DEVELOPMENT OF CHEMICAL IONIZATION MASS SPECTROMETRY FOR IN-SITU MEASUREMENT OF HYDROXYL (OH) AND HYDROPEROXYL (HO_2) RADICALS AND THEIR IMPACT ON ATMOSPHERIC CHEMISTRY

ZHOUXING ZOU

PhD

The Hong Kong Polytechnic University

2023

The Hong Kong Polytechnic University

Department of Civil and Environmental Engineering

Development of Chemical Ionization Mass Spectrometry for In-Situ Measurement of Hydroxyl (OH) and Hydroperoxyl (HO_2) Radicals and Their Impact on Atmospheric Chemistry

Zhouxing Zou

A thesis submitted in partial fulfillment of the
requirements for the degree of Doctor of Philosophy

December 2022

CERTIFICATE OF ORIGINALITY

I hereby declare that this thesis is my own work and that, to the best of my knowledge and belief, it reproduces no material previously published or written, nor material that has been accepted for the award of any other degree or diploma, except where due acknowledgment has been made in the text.

(Signed)

Zhouxing Zou (Name of student)

Abstract

The hydroxyl radical (OH) and hydroperoxyl radical (HO_2) play a central role in tropospheric chemistry. OH and HO_2, or HO_x, interconversion removes many reduced trace gases and forms secondary air pollutants. Measuring atmospheric concentrations of HO_x is a significant challenge due to its chemical properties. Additionally, the OH sources and sinks are poorly understood under low nitrogen oxides (NO_x) conditions. This study developed and optimized a chemical ionization mass spectrometer system (CIMS) with a calibration system to measure HO_x and investigate their impact on the atmosphere. Various components of the CIMS were compared to improve performance. The sensitivity of CIMS was improved by optimizing the flow rates of various gases and voltages. The sensitivity tests of the CIMS are explicitly described.

The first field campaign was conducted in urban Hong Kong in April 2019 to test the optimized CIMS for OH measurement. An obvious diurnal pattern of OH radicals was observed, with the highest concentration of 6×10^6 cm^{-3} at midday and the daytime detection limits at around 8×10^5 cm^{-3}. The overall uncertainty for this day is about ± 51%. The results demonstrated the capability of our CIMS for OH measurements.

The second field campaign was performed in autumn 2020 at a coastal site in Hong Kong. The measured average noontime OH concentration for the study period was $4.9 \pm 2.1 \times 10^6$ cm^{-3}. The 0D-Box model with comprehensive observational constraints reproduced daytime observed OH when the air parcels originated from the continental regions but overpredicted daytime observed OH for coastal air parcels by 142% on average. Missing reactivity for OH was proposed to be the cause of the model overprediction in low levels of NO_x and volatile organic compounds (VOCs). This finding implies the existence of unmeasured chemical species in the aged coastal air parcels. However, the lack of HO_2 measurement hindered further analysis.

Thus, in the third campaign in the winter of 2021-22 at the same coastal site, the CIMS was further developed for simultaneous measurement of ambient OH, HO_2, and

H_2SO_4 gases. A new data analysis method was developed to monitor the residual problem of the injection gases after switching measurement targets. Eleven days of results were obtained with the daily maximum concentration of HO_2, OH, and H_2SO_4 varying from 0.6 to 4.63 × 10^8 cm^{-3}, 2.6 to 15.42 × 10^6 cm^{-3}, and 4.11 to 10.79 × 10^6 cm^{-3}, respectively. This campaign shows the successful development of CIMS for HO_2 and H_2SO_4 measurement and the potential to simultaneously measure other species without isotopic $^{34}SO_2$ addition. This made our CIMS unique around the world.

Overall, this work developed the CIMS for HO_x and H_2SO_4 measurement, provided explicit details for the development and optimization processes of CIMS, performed the first comprehensive measurement of HO_x by CIMS in Asia, investigated the OH chemistry in the coastal environment of China, emphasized the knowledge gap of the aged air mass, and highlighted the importance of HO_x radical measurement to scrutinize our understanding of the atmosphere.

Publications

Published journal papers:

1. Wei Pu*, **Zhouxing Zou***, Weihao Wang, David Tanner, Zhe Wang, and Tao Wang: Development of a chemical ionization mass spectrometry system for measurement of atmospheric OH radical. *Atmospheric Measurement Techniques Discussions*, 2020, 1- 12, 68 (*Equal contribution)
2. Yi Chen, Yan Tan, Penggang Zheng, Zhe Wang, **Zhouxing Zou**, Kin-Fai Ho Shuncheng Lee, Tao Wang: Effect of NO_2 on nocturnal chemistry of isoprene: Gaseous oxygenated products and secondary organic aerosol formation. *Science of The Total Environment*, 156908, 2, 842, 2022.
3. **Zhouxing Zou**, Qianjie Chen, Men Xia, Qi Yuan, Yi Chen, Yanan Wang, Enyu Xiong, Zhe Wang, and Tao Wang: OH measurements in the coastal atmosphere of South China: possible missing OH sinks in aged air masses. *Atmospheric Chemistry and Physics*, 23, 7057-7074, 2023.

In preparation journal papers:

4. **Zhouxing Zou**, Tao Wang: Simultaneous measurement of HO_x and H_2SO_4 by CIMS in the coastal atmosphere of South China.

Acknowledgments

I express sincere gratitude to my chief supervisor, Prof. Tao Wang. He provides unique opportunities for me to challenge cutting-edge research. I am deeply impressed by his patient guidance, insightful suggestions, logical thinking, and academic writing skill. Furthermore, it is my honor to benefit from his personality and diligence especially his rigorous attitude to research, which I will treasure my whole life. My gratitude to him knows no bounds.

Many thanks to Dr. Pu Wei, who taught me first-hand experience on how to set up, maintain, and troubleshoot the CIMS instrument. His perseverance inspired and encouraged me to overcome the difficulties in CIMS development. I would like to thank Dr. Zhe Wang, a learned scholar who always provided insightful suggestions in discussions and always cares about my research and life. I am grateful to Mr. Steven Poon, who provides technical support to our research team. It is difficult to accomplish any field study without his help. Special thanks to Dr. Qianjie Chen who taught me the experience of model simulation and academic writing. The discussion with him is always interesting and inspiring. I would like to thank Mr. David Tanner and Dr. Alexandre Kukui for the discussion of CIMS development. It is heartening to hear from them when the CIMS development was hindered by difficulties.

Special thanks to Dr. Men Xia, Dr. Yi Chen, Enyu Xiong, Penggang Zheng, Qi Yuan, Dr. Haoxian Lu, Dawen Yao, and Yunxi Huo who worked together with me on projects, field campaigns, and manuscripts. I would like to thank Yanan Wang, Dr. Peng Wang, Chuan Yu, Yue Tan, Yifan Jiang, Dr. Xiaorui Chen, Dr. Zheng Zong, Dr. Chunshui Lin, and Dr. Meng Wang, Shichun Han, Weihang Sun for the discussion of research problems and life issue during lunch, swimming, and hiking. Thanks to other group members, Dr. Yiming Liu, Dr. Weihao Wang, Rongrong Gu, Jianing Dai, Dr. Yuting Wang, Dr. Wanyu Zhao, etc.

Thanks to Dr. Peter Louis from Hong Kong Environmental Protection Department for loaning the CIMS and supporting the field study in Hok Tsui. I am also thankful to Prof. S.C. Lee, Prof. Hai Guo, and Dr. Xiaopu Lv. They provide important suggestions during the Ph.D. confirmation of candidature and supporting data for analysis after the campaign. Thanks to Mr. Changbei Yu, Dr. Waichin Li, Prof. Adam Dillon, Dr. Avinnash P. Tiwari, and Prof. Mark Reed, who enlighten me on science before I start my research study. Thanks, Prof. Henrik Skov, Dr. Andreas Massling, and Prof. Ole John Nielsen for the help and support during the postgraduate study and the Arctic campaign.

I express many thanks to my father Mr. Jianwen Zou, my mother Ms. Jingwen Lai, and other family members. They genuinely care for me and love me. They are a powerful backup force in my life and encourage me to complete my Ph.D. study.

I sincerely thank the Hong Kong Research Grants Council for funding my research (Project No. T24-504/17-N). I also appreciate the resources provided by the Hong Kong Polytechnic University, e.g., the swimming pool, laboratory platforms, and library resources that support my study, research, and life.

Finally, thanks to all the wildlife I meet in Hok Tsui including the wild pig family who asks me for food, the geckoes who lay eggs next to the CIMS, and the spiders who always surprise me. They show me the tenacity of life.

Table of Contents

List of Figures

List of Tables

List of Abbreviations

Abb.	Full Name
$^{34}SO_2$	Isotopic sulfur dioxide
a.s.l.	above sea level
AVOCs	Anthropogenic volatile organic compounds
BVOCs	Biogenic volatile organic compounds
C_3F_6	Hexafluoropropene
CAS	Chinese Academy of Sciences
CDC	Collisional dissociation chamber
CI	Criegee intermediates
CIMS	Quadrupole chemical ionization mass spectrometer
CNRS	Laboratoire des Sciences du Climat et de l'Environnement
CO	Carbon Monoxide
NCAR	National Center for Atmospheric Research Boulder, Colorado
DOAS	Differential optical absorption spectroscopy
DWD	German Meteorological Service Hohenpeissenberg
EPD	Environmental Protection Department
FAGE	Fluorescence assay by gas expansion technique
F_{IE}	Ionization efficiency factor
F_{TE}	Transmission efficiency factor
F_{CE}	Conversion efficiency factor
FZJ	Forschungszentrum Jülich
GC-FID/MS	Gas chromatography-flame ionization detector/ mass spectrometry
Georgia	Georgia Institute of Technology
H_2SO_4	Sulfuric acid
HK	Hong Kong
HNO_3	Nitrate acid
HO_2	Peroxy radicals
HOMs	Highly oxidized organic molecules
HONO	Nitrous acid
HO_x	Hydroxyl and peroxy radicals

HO_x	Hydrogen oxide radicals (OH and HO_2)
HT	The Hok Tsui site
HT 2020	The second campaign in Hok Tsui, 2020
hv	Light, in chemistry shorthand
IDC	Ion detection chamber
IGC	Ion guide chamber
Indiana	Indiana University
Irvine	University of California, Irvine
JASMTEC	Japan Agency for Marine-Earth Science and Technology
K	Reaction constant
kmiss	Calculated missing OH reactivity
Leeds	University of Leeds
LIF	Laser-induced fluorescence
Lille	University of Lille
m/z	Mass-to-charge ratio
MPI	Max Planck Institute for Chemistry
MCM	Master chemical mechanism
MFC	Mass flow controller
min	Minute(s)
MVK	Methyl vinyl ketone
NO	Nitric oxide
NO_2	Nitrogen dioxide
NO_x	Oxides of nitrogen
NSI	Normalized Signal Intensity at m/z 97
NUIG	National University of Ireland, Galway
$O(^1D)$	Singlet state oxygen
OH	Hydroxyl radicals
OVOCs	Oxygenated volatile organic compounds
PKU	Peking University
$PM_{2.5}$	Fine particulate matter
PolyU	The Hong Kong Polytechnic University
PolyU2019	The first campaign at PolyU, April 2019
ppbv	Parts per billion by volume

ppmv	Parts per million by volume
pptv	Parts per trillion by volume
PRD	The Pearl River Delta
PSU	Pennsylvania State University
RH	Relative humidity
RO_2	Organic-peroxide
ROOOH	Hydrotrioxide
S_{62}	The signal at 62 m/z
S_{64}	The signal at 64 m/z
S_{97}	The signal at 97 m/z
S_{97NO}	The signal at 97 m/z with SO_2 and NO injection
S_{97SO2}	The signal at 97 m/z with SO_2 injection
$S_{97SO2Sca}$	The signal at 97 m/z with SO_2 and scavenger gas injection
$S_{97w/o}$	The signal at 97 m/z without any additional gases
SAPHIR	Simulation of atmospheric photochemistry in a large reaction
sccm	Standard-state cubic centimeter per minute
SCI	Stabilized criegee intermediates
S_{H2SO4}	The signal at 97 m/z corresponded with the H_2SO_4 concentration
S_{HO2}	The signal at 97 m/z corresponded with the HO_2 concentration
slpm	Standard-state liter per minute
SMPS	Scanning mobility particle sizer
$S_{NoiseCIMS}$	The signal at 97 m/z corresponded to noise from CIMS
$S_{NoiseHO2}$	The signal at 97 m/z corresponded to noise for HO_2 measurement
$S_{NoiseOH}$	The signal at 97 m/z corresponded to noise for OH measurement
SO2	Sulfur dioxide
SOA	Secondary organic aerosols
S_{OH}	The signal at 97 m/z corresponded with the OH concentration
Tof-CIMS	Time of flight chemical ionization mass spectrometer
VOCs	Volatile organic compounds

1. Introduction

This study focuses on the investigation of the OH, HO_2 measurement, and the OH radical impact on the atmosphere. This chapter starts with the structure of the thesis (section 1.1), followed by an introduction to the formation and removal processes of the OH, HO_2, and RO_2 in the atmosphere (section 1.2). The importance and impact of these radicals are discussed in section 1.3. Overall, the introduction section provided the reactions and theoretical basis of the thesis.

1.1 Structure of the thesis

The thesis is composed of seven chapters which are summarized as follows:

Chapter 1 provides the outline of the study, the current knowledge of the RO_x family, and their impotency.

Chapter 2 reviews three major techniques for HO_x measurement, summarizes the previous field campaigns, and emphasizes the discrepancy found between observation and simulation results.

Chapter 3 clarifies the research gaps in the literature review and how this study fulfills the research demand of the gaps.

Chapter 4 introduces the measurement principles, the CIMS constructions, and the calibration system. Then this chapter presents the unique procedure for CIMS optimization to achieve a better sensitivity of measurement by adjusting the injected gases, flow rates, and voltages of the CIMS. Lastly, the optimization results are shown as the optimized detection limit uncertainty and calibration factor.

Chapter 5 introduces the field conditions, presents the campaign setups, summarizes the specification of the CIMS in three campaigns, and presents the modeling setup for simulation.

Chapter 6 shows the observation results of field campaigns. The first campaign results show the capability of CIMS for OH measurement. The second field study reveals the overestimation of simulated OH in aged air mass and proposed the existence of unmeasured OH sinks. The third campaign tests the capability of CIMS for HO_x and H_2SO_4 measurement.

Chapter 7 gives a summary of the major findings of this study and suggestions for future work.

1.2 The RO_x Chemistry

The OH radical mechanism was first deduced in the early 1970s. With the help of ^{14}C isotopic trace methods, Weinstock and Niki (1972) deduced that the CO lifetime was far shorter than the scientists believed and proposed that the OH radical in the troposphere was responsible for the short lifetime of CO. The follow-up studies proved the existence and importance of OH in the troposphere. It is now well known that the hydroxyl radicals (OH) govern the oxidative capacity of the natural atmosphere and initiate the reaction chains in both polluted and clean atmospheres since it reacts with virtually all trace species. HO_2 and RO_2 are the products of the oxidation of CO and VOCs initialed by OH. This chapter starts the introduction of the RO_x family with the production of OH.

1.2.1 The Primary Production of OH

The primary production of OH radical in the troposphere is the photolysis of tropospheric ozone and HONO:

R 1.1 $O_3 + hv \rightarrow O_2 + O(^1D)$

R 1.2 $H_2O + O(^1D) \rightarrow 2OH$

R 1.3 $HONO \rightarrow OH + NO$

Even though HONO is the reservoir species of OH (see section 1.2.3), the source of HONO includes other reactions besides OH + NO, for example, the heterogeneous reactions (Fu et al., 2019). Thus, the HONO photolysis is introduced as the primary source of OH. Besides that, the ozonolysis of alkene (R 1.4 and R 1.5) also contributes to the ambient OH radicals.

R 1.4 $Alkene + O_3 \rightarrow SCI + CI + RCHO$

R 1.5 $CIs \rightarrow OH + R'COR''$

Where the (SCI) and CI represent the (stabilized) criegee intermediates (Mauldin III et al., 2012). The CIs produced from ozonolysis dominate the primary nighttime OH radical and gaseous sulfuric acid concentration (Guo et al., 2021).

The dominant production of OH for the different regions is different due to the air conditions. Globally, ozone photolysis dominates the production of OH. However, during the winter haze events (Ma et al., 2019) or in the polar region (Kukui et al., 2014), HONO photolysis contributed to the majority of OH production. On the other hand, OH production in coastal areas like the Hok Tsui site is dominated by HO_2 and RO_2 recycling instead of primary production (see details in section 6.2).

1.2.2 The Production of Peroxide and the RO_x cycle

The RO_x cycle starts with the primary production of OH radicals. The OH subsequently reacts with hydrocarbons R 1.6, and carbon monoxide R 1.7 forming organic-peroxyl (RO_2) and hydroperoxyl (HO_2)

R 1.6 $OH + RH + O_2 + M \rightarrow RO_2 + H_2O + M$

R 1.7 $OH + CO + O_2 + M \rightarrow HO_2 + CO_2 + M$

where M refers to air molecules (mostly N_2 and O_2) that collide and carry away energy. The peroxy radicals (HO_2 and RO_2) in high NO_x (NO_2 + NO) conditions may react with NO and recycle back to OH, with associated NO to NO_2 conversion.

R 1.8 $RO_2 + NO + O_2 \rightarrow R'HO + NO_2 + HO_2$

R 1.9 $HO_2 + NO \rightarrow OH + NO_2$

In the daytime, the NO_2 undergoes photolysis to form NO and leading to the formation of ozone (R 1.10 and R 1.11). This means the NO_x family promotes the recycling of HO_2 to OH in the daytime and such a cycle leads to secondary ozone production.

R 1.10 $NO_2 + hv \rightarrow NO + O$

R 1.11 $O + O_2 + M \rightarrow M + O_3$

In low NO_x condition, the HO_2 react with O_3 and recycle back to OH:

R 1.12 $O_3 + HO_2 \rightarrow OH + 2O_2$

Additionally, in high BVOCs conditions, a series of mechanisms was proposed for HO_2 and OH regeneration from RO_2 by H-shift without reacting with NO_x (Peeters et al., 2009). The details for the review of these studies are shown in section 2.2.2. Since the interactions between OH, HO_2, and RO_2 are fast compared to the other reactions and the lifetime of other species, they are collectively named as HO_x (HO_2 + OH) and RO_x (OH + HO_2 + RO_2) families.

1.2.3 The Reservoir Species in RO_x Chemistry

When the RO_x radicals are converted to relatively stable molecules and temporarily removed from the atmosphere, they are "stored" in the reservoir species. The reservoir species of the RO_x family include the HOOH, ROOH, HONO, and Peroxyacetyl

Nitrates (PANs) (R 1.21 to R 1.23). They have a longer lifetime (1-10 days) than the RO_x radicals and can recycle back via photolysis (R 1.3, R 1.16, R 1.17, and R 1.23) or the reaction with OH (R 1.18 to R 1.20). The hydroperoxides (ROOH and HOOH) are formed by HO_2 (R 1.13) and RO_2 (R 1.14) and react with HO_2 in the low NO_x region. The HONO (R 1.15) on the other hand, is formed when NO is present. The NO reacts with OH is the main source of atmosphere HONO which contributes 95% of atmospheric HONO production.

R 1.13 $HO_2 + HO_2 \rightarrow HOOH + O_2$

R 1.14 $RO_2 + HO_2 \rightarrow ROOH + O_2$

R 1.15 $OH + NO \rightarrow HONO$

R 1.16 $HOOH + hv \rightarrow 2OH$

R 1.17 $ROOH + hv \rightarrow OH + RO$

R 1.18 $HOOH + OH \rightarrow H_2O + HO_2$

R 1.19 $ROOH + OH \rightarrow R'CHO + OH + H_2O$

R 1.20 $HONO + OH \rightarrow NO_2 + H_2O$

The formation of PANs, the well-known photochemical smog constituent and important reservoir of RO_2 and NO_x, is also closely related to OH radicals. The reaction of the aldehydes with OH radical (R 1.21) forms the peroxyacetyl radicals ($RC(O)O_2$) which further reacts with NO_x and forms PANs (R 1.22 and R 1.23).

R 1.21 $RCHO + OH \rightarrow RC(O)O_2 + H_2O$

R 1.22 $RC(O)O_2 + NO \rightarrow NO_2 + CO_2 + RO_2$

R 1.23 $RC(O)O_2 + NO_2 + M \rightleftharpoons RC(O)O_2NO_2 + M$

The PANs are available for regional transport and produce RO_2 and NO_x by photolysis and thermal decomposition. Thus, the concentration and exact lifetime of PANs are directly related to the air pollution problem and have attracted considerable interest (Singh and Hanst, 1981).

1.2.4 The Sinks of RO_x Radicals

Compared to the reversible reactions in section 1.2.3, the formations of H_2SO_4 (R 1.24 to R 1.26) and HNO_3 (R 1.27) are the irreversible removal paths for the OH radical, and these processes are related to the acid rain issue.

R 1.24 $OH + SO_2 + M \rightarrow HSO_3 + M$

R 1.25 $HSO_3 + O_2 \rightarrow SO_3 + HO_2$

R 1.26 $SO_3 + 2H_2O \rightarrow H_2SO_4 + H_2O$

R 1.27 $OH + NO_2 + M \rightarrow HNO_3 + M$

The reactions of OH with SO_2 to form H_2SO_4 are the key reaction for the OH measurement by the CIMS. See section 4.1 for details.

Another potential loss for RO_x is the heterogeneous uptake of HO_2 by the aerosol particles. The loss rate is dominated by the aerosol surface area and the uptake coefficient. However, the understanding of HO_2 uptakes requires more investigation and the uptake coefficient differs by 3 to 5 magnitudes (Song et al., 2020) (see section 5.2 for the HO_2 uptake in the box model). The heterogeneous uptake, on the other hand, represents a very minor sink of OH (Ivanov et al., 1996; Park et al., 2008) and there is a lack of studies about the heterogeneous uptake of RO_2. Besides that, the wet and dry depositions of the reservoir species (like the wet deposition of H_2O_2) are also important removal paths of RO_x radicals from the atmosphere.

1.3 The Importance of RO_x

As shown in previous contents, OH is the major oxidant in the atmosphere and relates to the self-cleaning process in all air conditions. In regions strongly affected by anthropogenic activities, the RO_x cycle assisted by NO (R 1.6 to R 1.9) decomposes the anthropogenic VOCs to CO_2. In the forest region, the OH initiates the degradation of biogenic VOCs (BVOCs) like isoprene (Wennberg et al., 2018) and monoterpene (Rolletter et al., 2019). During the last decade, the importance of the RO_x family in the forest region was further emphasized by the new recycling mechanisms discovered by the measurement in forests (Lu et al., 2013b) and the follow-up chamber study (Peeters et al., 2014). Moreover, the major anthropogenic greenhouse gas, methane, is mainly removed by OH which means that the RO_x family is also closely related to climate change (Zhao et al., 2020a).

The RO_x family is also closely related to secondary organic aerosols (SOA) production. The reactions of OH with SO_2 (R 1.24 to R 1.26) and NO_2 (R 1.27) as well as the self- and cross-reactions of RO_2 and HO_2 transform the primary pollutants into low-vapor pressure gas molecules such as nitric acid (HNO_3), sulfuric acid (H_2SO_4), and highly oxidized organic molecules (HOMs) (Lu et al., 2012). These products are partitioned into aerosol particles and undergo multiphase reactions that form SOA. They contribute to the aerosol mass in the atmosphere and further affect chemistry, visibility, climate, and human health (Ziemann and Atkinson, 2012). Besides that, the previously mentioned PANs formation via OH reaction with aldehyde and the secondary NO_2 (R 1.9) and ozone (R 1.10 and R 1.11) formation also deteriorate the air conditions.

Thus, the RO_x family plays a key role not only in the degradation of VOCs but also in major environmental issues such as photochemical pollution, acid rain, haze, and climate change (Calvert et al., 1985; Kulmala et al., 2004; Wang et al., 2017; Lu et al., 2019). Therefore, the comparison of observed and model-simulated RO_x concentrations are vital for the estimation of the trace-gas lifetime and the comparison result is an indicator of our understanding of atmospheric chemistry. In the next sections, the previous efforts in RO_x measurement and modeling will be introduced.

2. Literature Review

As stated in the last section, the RO_x family dominates the atmospheric oxidation process and is closely related to environmental issues. Therefore, the observation of RO_x is important for our understanding of atmospheric chemistry. To observe the RO_x family, the measurement technique for OH radical is critical since the measurement of RO_2 and HO_2 is achieved by converting them to OH (R 1.8 and R 1.9). Due to the complexity of RO_2 species, there are limited results of RO_2 measurement. Therefore, section 2.1 mainly focuses on OH measurement techniques and their advantages and disadvantages. Then section 2.2 summarizes and reviews the comparison between observed HO_x concentration and the zero-dimensional box model simulated HO_x concentration to scrutinize our understanding of atmospheric photooxidation chemistry in different conditions.

2.1 The Measurement Methods

Since the importance of OH was revealed in the 1970s (Levy, 1971), concerted efforts have been made to develop techniques to measure OH in the atmosphere (Hard et al., 1979). However, the low concentration, high reactivity, and short lifetime (<1 s) of OH make it very difficult to be detected and quantified. The low concentration requires high sensitivities and small interferences in the instruments; the high reactivity demands a small loss in the sampling system, and the short lifetime requires measurement at a high temporal-spatial resolution. It is a big challenge to meet all of these requirements in a measurement system (Lu et al., 2019).

During the past decades, three major techniques have been developed for in-situ OH measurements: differential optical absorption spectroscopy (DOAS) (Perner et al., 1976), laser-induced fluorescence assay by gas expansion technique (LIF) (Hard et al., 1979), and chemical ionization mass spectrometry (CIMS) (Eisele and Tanner, 1991).

LIF and DOAS directly measure OH based on spectroscopic methods. CIMS on the other hand, measured OH indirectly by converting it to HSO_4^- for mass spectrometer detection. As shown in Figure 2.1.1, sixteen research institutes around the world are capable of HO_x measurement based on these techniques. The colors label the nation of the research groups. The measurement method for HO_x measurement is labeled in a different shape: triangle, circle, and diamond represent the groups using LIF, CIMS, and more than one instrument, respectively. The CIMS developed in this study is labeled by a star. The names, detection limits uncertainties, and references of each instrument are summarized in Table 2.1.

Unlike the measurement of OH, the HO_2 and individual species of RO_2 ($^*RO_2$) measurements for both CIMS and LIF are achieved by a similar indirect measurement method. The ambient HO_2 and $^*RO_2$ are converted to OH by the addition of NO injected into the sample flow as shown in R 1.8 and R 1.9. Then the HO_2 and $^*RO_2$ are detected in the form of OH in the LIF and further converted to HSO_4^- for detection in CIMS. The

DOAS is unable to measure HO_2 and $*RO_2$. The following sections will introduce the basic OH measurement theory for different methods, the modification, and findings based on these techniques. The optimization and findings of the HO_xCIMS in PolyU will be discussed in the latter section.

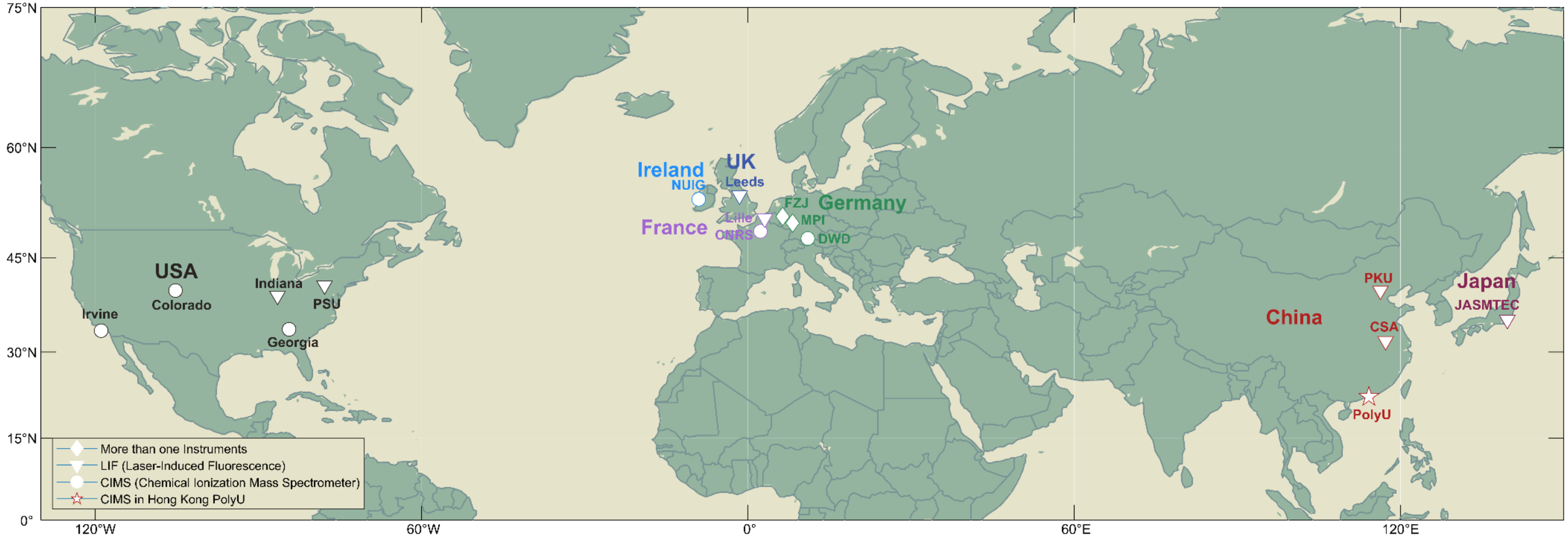

Figure 2.1.1 Research groups and their location around the world.

Table 2.1 Summary of research instruments for HO_x measurement with the detection limits (DL) and uncertainties.

Group Abb.	Name of institution	Nation	Instrument (Name)	Interpolation time	S/N	DL of OH: 10^5 (cm^{-3})	OH Uncertainty	DL of HO_2: 10^6 or *Others (cm^{-3})	HO_2 Uncertainty	LOD Reference
FZJ	Forschungszentrum Jülich	Germany	DOAS	205 s	1	8	6.5% (1σ)	N/A	6.5% (1σ)	(Pang et al., 2022)
			LIF-FAGE	47 s	1	3.5	13% (1σ)	15	16% (1σ)	(Pang et al., 2022)
PSU	Pennsylvania State University	USA	LIF-FAGE (GTHOS or ATHOS)	1 min	1	2.7	32% (2σ)	4.9	32% (2σ)	(Faloona et al., 2004; Brune et al., 2020)
PKU	Peking University	China	LIF-FAGE (PKU-LIF)	30 s	2	6	10% (1σ)	10	13% (1σ)	(Ma et al., 2022)
Leeds	University of Leeds	UK	LIF-FAGE (AirFAGE)	7 mins	2	5.5	26% (2σ)	3.1 *CH_3O2: 6.5	26% (2σ)	(Slater et al., 2020)
Lille	University of Lille	France	LIF-FAGE (UL-FAGE)	1 min	N/A	3.7	N/A	Not provided	N/A	(Blocquet et al., 2013)
JASMTEC	Japan Agency for Marine-Earth Science and Technology	Japan	LIF-FAGE	73 s	2	5.3	20% (1σ)	5.4	24% (1σ)	(Kanaya et al., 2012)
Indiana	Indiana University	USA	LIF-FAGE (IU-FAGE)	OH: 30 mins HO_2: 20 s	1	8	18% (1σ)	70	18% (1σ)	(Lew et al., 2020)
MPI	Max Planck Institute for Chemistry	Germany	LIF-FAGE (HORUS)	1 min	2	9.8	28.5% (1σ)	19.7	36% (1σ)	(Nussbaumer et al., 2021; Marno et al., 2020)
CAS	Chinese Academy of Sciences	China	LIF-FAGE (AIOFM-LIF)	1 min	1	1.7	14% (1σ)	8	17% (1σ)	(Zhang et al., 2022b)

Table 2.1 (Continued)

Group Abb.	Name of institution	Nation	Instrument (Name)	Interpolation time	S/N	DL of OH: 10^5 (cm^{-3})	OH Uncertainty	DL of HO_2: 10^6 or *Others (cm^{-3})	HO_2 Uncertainty	LOD Reference
Georgia	Georgia Institute of Technology	USA	*CIMS	10 mins	N/A	1.3	30% (3σ)	Not provided	35% (3σ)	(Liao et al., 2011)
			Br-Tof-CIMS	1 min	3	N/A	N/A	17.2	18% (1σ)	(Sanchez et al., 2016)
NCAR	National Center for Atmospheric Research Boulder, Colorado	USA	CIMS (PeRCIMS)	1 min	2	2	35% (N/A)	2	35% (N/A)	(Wolfe et al., 2014)
CNRS	Laboratoire des Sciences du Climat et de l'Environnement	France	*CIMS	2 mins	3	5	40% (2σ)	2	47% (2σ)	(Kukui et al., 2014)
DWD	German Meteorological Service Hohenpeissenberg	German	*CIMS	8 s	2	4.5	19% (1σ)	*H_2SO_4: 3×10^4	19% (1σ)	(Berresheim et al., 2000; Kanaya et al., 2012)
MPI	Max Planck Institute for Chemistry	Germany	CIMS	1 min	N/A	N/A	N/A	*HO_2 and RO_2: 12.3	20%	(Hanke et al., 2002)
NUIG	National University of Ireland, Galway	Ireland	*CIMS	5 mins	2	2.4	40% (2σ)	*H_2SO_4 & MSA: 4.3×10^4	40% (2σ)	(Berresheim et al., 2014)
Irvine	University of California, Irvine	USA	*CIMS (AP-CIMS)	5 mins	2	1	40% (2σ)	N/A	40% (2σ)	(Jeong et al., 2022)
PolyU	Hong Kong Polytechnique University	HK, China	CIMS	3 mins	2	1.7	48% (3σ)	20	38% (3σ)	This thesis

N/A: not available *CIMS: the CIMS using isotopic $^{34}SO_2$ for OH measurement.

2.1.1 Differential Optical Absorption Spectroscopy (DOAS)

The DOAS method measures the absorption of the OH radicals under the 308 nm wavelength (Perner et al., 1976). and calculates the measured concentration by the Beer-Lambert law,

E 2.1 $$[OH] = ln\left(\frac{I_0}{I}\right) \times \frac{1}{\sigma_{OH} l}$$

where, I_0 is the background light intensity before transmission through the atmosphere and I represents the light intensity after the transmission. The σ_{OH} is the absorption cross-section of OH with respect to the wavelength used in the instrument. l represents the path length.

The advantages of DOAS are due to the Beer-Lambert law. Firstly, DOAS is self-calibrating because of the law and does not require a calibration device. Secondly, the uncertainty of DOAS is limited only by the accuracy of absorption cross-section and the path length, which provide an extremely low uncertainty (6-7%, Pang et al., 2022a) when compared to the other two measurement methods (See Table 2.1). These major advantages make DOAS the primary standard in OH measurement. However, due to the extremely low ambient OH concentration (~10^6 cm^{-3}), DOAS requires a long path length for measurement (up to 10 km) to create a measurable difference between I_0 and I (Hard et al., 1979; Stone et al., 2012). Thus, the size and the alignment of DOAS become difficulties in the experiment and field study. Moreover, the DOAS requires considerable averaging of air masses, and interference from other atmospheric constituents also affects the OH measurement.

Even with these difficulties, some field measurements (Perner et al., 1976; Hübler et al., 1984; and Platt et al., 1988) were done with the DOAS and provided the earliest observed OH concentrations in the low troposphere including the marine boundary layer (Brauers et al., 2001). The only DOAS that remain in service for OH measurement is owned by the Forschungszentrum Jülich, Germany, which is used for the studies of Simulation of Atmospheric PHotochemistry In a large Reaction (SAPHIR) Chamber. With the help of this DOAS, the SAPHIR can monitor the OH concentration and reveal the atmospheric oxidation processes of important VOCs species initiated by OH like methacrolein (Fuchs et al., 2014), β-pinene (Kaminski et al., 2017), methyl vinyl ketone (MVK, Fuchs et al., 2018), isoprene (Novelli et al., 2020a; and Zhao et al., 2021), myrcene (Tan et al., 2021) and limonene (Pang et al., 2022). Besides the investigation of oxidation processes, the DOAS application in the chamber also provides a unique opportunity for intercomparison between different HO_x measurement techniques (Schlosser et al., 2009; Fuchs et al., 2010), and for investigation of the LIF-FAGE interference under different conditions (Fuchs et al., 2012a, and 2016a, see details in section 2.1.2).

2.1.2 Laser-Induced Fluorescence Assay by Gas Expansion technique (LIF-FAGE)

Different from the DOAS which measures OH based on absorption, LIF-FAGE measures the OH radicals by the laser-induced fluorescence techniques. The method was pioneered in the 1970s and used the laser at 282 nm for OH excitation and to measure the resonance fluorescence emitted by the excited OH radicals (Hard et al., 1979, 1984). However, the problems of scattering and interference hinder the application of LIF. For example, the photolysis of ozone and the subsequent reaction with H_2O (R 1.1 and R 1.2) to form OH radicals contribute to interference signals and deteriorate the ambient OH measurement, especially in the troposphere (Smith and Crosley, 1990). Thus the LIF technique was applied for stratospheric OH measurement before the 1990s (Wennberg et al., 1990). Then a series of improvements to LIF were done. 1. The laser wavelength of LIF was tuned to selectively excite the OH radicals on a single rovibronic transition at 308 nm for higher sensitivity (Hofzumahaus and Holland, 1993). 2. The scavenger gas hexafluoropropene (C_3F_6) was introduced to remove the ambient OH and the interference produced was monitored by the LIF (Dubey et al., 1996). 3. A variety of laser system types was developed by different research institutes to achieve better detection limits (Stimpfle and Anderson, 1988; Chan et al., 1990; Dubey et al., 1996; Tan et al., 1998). With the improvements, the detection limits for LIF reach from 2 to 10 × 10^5 cm^{-3} for HO_x measurement (Table 2.1).

In the last twenty years, the LIF is recognized as the most widely used technique for OH measurement in laboratory and field studies globally (Stone et al., 2012; Lu et al., 2019). As shown in Figure 2.1.1 and Table 2.1, nine groups measured HO_x by LIF and had various contributions to our understanding of the atmosphere. Some examples of the findings for different groups are shown below.

The Forschungszentrum Jülich (FZJ) groups found the well-known underestimated OH in the forest region by comparing observation to model simulation (Hofzumahaus et al., 2009) and discovered the possible complementary mechanisms in the chamber studies. Such underestimation was found in different forests by LIFs owned by Indiana University (Indiana), University of Leeds (Leeds), Pennsylvania State University (PSU), Max Planck Institute for Chemistry (MPI), and Peking University (PKU). The PSU developed two forms of LIF configuration for ground and aircraft measurement named GTHOS and ATHOS, respectively (Ground or Air based Tropospheric Hydrogen Oxides Sensor, Faloona et al., 2004). The GTHOS found the possible interference of LIF in low NO_x forest conditions (Mao et al., 2012), and the ATHOS found missing OH reactivity in the global marine boundary layer during the Atom campaign (Thames et al., 2020). The follow-up study of the interference by the University of Lille (Lille) found that such interference in low NO_x atmosphere measurement might be the Hydrotrioxide species (ROOOH, Fittschen et al., 2019). The underestimation and the interference of LIF in low NO_x conditions guide the research interests of OH until now (see section 2.2.2. for a detailed description).

On the other hand, the Japan Agency for Marine-Earth Science and Technology (JASMTEC) found the overestimation of OH in the coastal air (Kanaya et al., 2012), and investigated possible missing reactivity, after the modification of the LIF for measuring OH reactivity, in different regions of Japan (Ramasamy et al., 2016; Li et al., 2020a, 2021a, see section 2.2.1 for underestimation studies review).

The measurement of HO_x by LIF also contributes to the pollution analysis. The PKU and the Chinese Academy of Sciences (CAS) applied the LIF for pollution study in different cities in China and revealed the importance of OH production from HONO in the winter haze period (Tan et al., 2018) and stated the unknown behaviors of RO_2 for high-NOx regimes (Zhang et al., 2022b). The LIF in MPI participated in the HCHO budget study around Europe and defined the Ozone formation regimes in different areas.

Compared to the DOAS, the LIF has an advantage in size, selectivity, and sensitivity (Heard and Pilling, 2003). However, the requirement of a calibration system increases the measurement uncertainty.

2.1.3 Chemical Ionization Mass Spectrometer (CIMS)

The CIMS technique measures OH indirectly based on an ion-assisted mass spectrometry method. It employs a chemical reaction scheme that OH is firstly converted into H_2SO_4 (R 1.24 to R 1.26) by isotopic $^{34}SO_2$, and $H_2{}^{34}SO_4$ is subsequently measured by a specific chem-ionization method (Eisele and Tanner, 1991). The CIMS technique for measuring OH was first developed at the Georgia Institute of Technology (Georgia) by Eisele and Tanner (1991). The system was further improved at the National Center for Atmospheric Research (NCAR) by reducing wall reactions (Eisele and Tanner, 1993), reducing the background signal (Tanner and Eisele, 1995), and developing a better calibration system (Tanner et al., 1997). Mauldin et al., (1998) modified the CIMS for measurement at an aircraft platform during the First Aerosol

Characterization Experiment (ACE1). Edwards et al., (2003a) further upgraded the calibration system and developed the measurement of HO_2 and RO_2 by controlling the concentration of NO and SO_2 added to the instrument.

Based on the design of Tanner et al. (1997) and the modifications mentioned above, other CIMS instruments were developed at the Meteorological Observatory Hohenpeissenberg (DWD), Germany, by Berresheim et al. (2000) and at the National University of Ireland Galway (NUIG) by Berresheim et al. (2013). Kukui et al. (2008) developed a new version of the CIMS instrument with a newly designed inlet for residual time reduction at the Centre National de la Recherche Scientifique (CNRS), France.

Most of the CIMS uses isotopic $^{34}SO_2$ for OH conversion. The conversion product, $H_2{}^{34}SO_4$, has a different mass-to-charge ratio. In this way, the ambient H_2SO_4 interference can be eliminated. final ratio of [NO] to [SO_2], CIMS has lower noise and higher sensitivity compared to either DOAS or LIF techniques for OH measurement because of the higher collection efficiency of ions than photons (Hard et al., 1979)(See Table 2.1 for specific detection limit for different instruments). As a result, CIMS processes the lowest detection limit for ambient OH measurement among the three techniques (Heard and Pilling, 2003).

Despite the advantage of isotopic $^{34}SO_2$, this chemical is expensive due to the limited demand and lacking industrial scale production. Some research institutes like Georgia and NCAR use the ^{34}S powder combustion technique to produce the isotopic $^{34}SO_2$. The ^{34}S powder is regulated due to its reactive chemical properties and is expensive. The safety issue in the combustion process and the storage requirement of the gases are also obstacles to isotopic $^{34}SO_2$ application. Thus, even though the isotopic $^{34}SO_2$ improved the CIMS's performance, the difficulty in getting $^{34}SO_2$ hampered the application of CIMS. Additionally, the indirect measurement method of CIMS is not suitable for a high NO_x environment due to NO-caused interference.

The HO_x measurement by CIMS has been used to investigate the observation-model discrepancy in the forest regions (Wolfe et al., 2014; Jeong et al., 2022). However, compared to the LIF which was used for measurements in urban as well as clear environments, the CIMS was mainly deployed to the polar (Kukui et al., 2014), coastal (Berresheim et al., 2002), and remote atmospheres (Tan et al., 2001b), which were characterized by clean conditions.

2.2 Comparison of Observed and Simulated Concentrations of HO_x

After the development of HO_x measurement techniques, the HO_x observations were performed by different research institutes around the world in different environments (Figure 2.2.1). The measurement results were often compared with model simulations to evaluate whether a model has included major sources and sinks of HO_x. Table 2.2 summarizes the latest measurement and comparison results for the campaigns shown in different locations in Figure 2.2.1. The simulated versus observed HO_x ratios ($R_{S/O}$) show the discrepancy between observation and simulation.

As concluded by previous reviews (Lu et al., 2019; Rohrer et al., 2014; Stone et al., 2012), the observed OH concentrations can generally be reproduced by box models under high NO conditions (NO > 1 ppb) such as at the urban sites or within polluted air mass (Table 2.2). However, the discrepancies between the model and observation were often found under low NO conditions (NO < 1 ppb); the model generally overpredicts OH observations in a low VOCs environment (Table 2.2a, section 2.2.1) and underpredicts OH observations in a high biogenic VOCs (BVOCs) environment (Table 2.2b, section 2.2.2).

The HO_2, on the other hand, didn't show clear trends that the agreement between observation and simulation has been highly variable in different environments as shown by the HO_2 $R_{S/O}$ in Table 2.2 and mentioned by the previous study (Lew et al., 2020). This variation might due to the interference from aromatic and alkene based RO_2 during HO_2 measurement. (Lew et al., 2020)

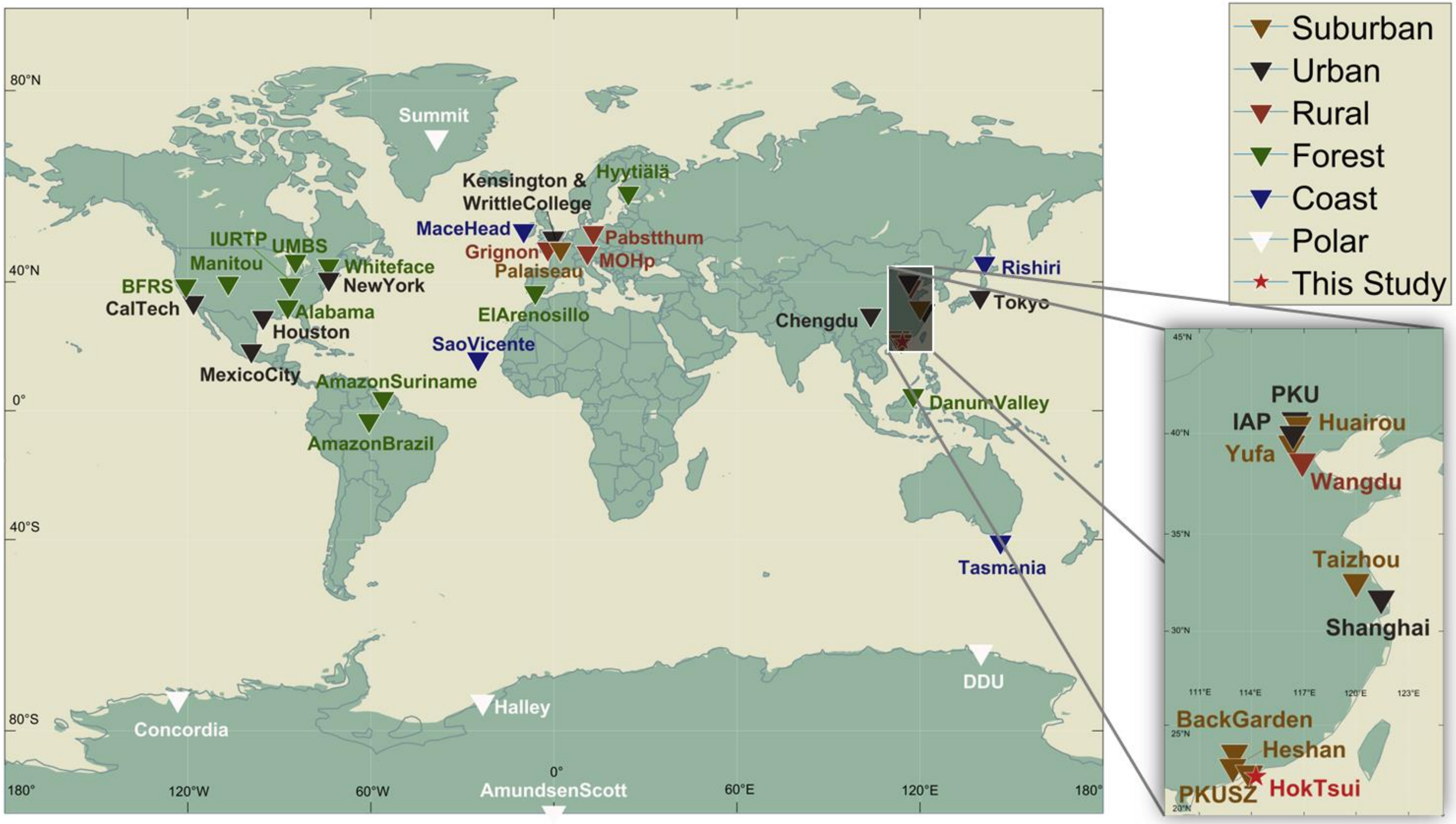

Figure 2.2.1 The HO_x measurements around the world.

Table 2.2 Summary of the latest studies with respect to the measurement site shown in Figure 2.2.1.

Comparison results (OH only)	Reference	Time	Location in Figure 1	Site type	Instrument for HO_x	Measurement notes	OH conc. 10^6 cm^{-3}	HO_2 conc. 10^8 cm^{-3}	Ratio notes	OH $R_{S/O}$	HO_2 $R_{S/O}$	Other references targeting the same site
Overprediction	(Berresheim et al., 2002)	June–July 1999	MaceHead	Coast	CIMS	Mean (All) Peaks (Mean Clean) Peaks (Pollution)	0.12 2.5 18 & 12	N/A	Mean (17 June, Coastal) Mean (30 July, Continental)	2 ~1	N/A	(Carslaw et al., 1999; Berresheim et al., 2013, 2014);
Overprediction	(Sommariva et al., 2004; Creasey et al., 2003);	Jan–Feb 1999	Tasmania	Coast	LIF	Mean (Peaks) Peaks (Range)	3.5 2 to 5.5	2 1 to 2.5	Mean (7–8 Feb) Mean (15–16 Feb)	~1.11 ~1.32	N/A ~2	N/A
Overprediction	(Kanaya et al., 2007a)	September 2003	Rishiri	Island Coast	LIF	Peaks (Mean)	2.7	1.45	OH rectified by constrained HO_2	1.35	1.89	N/A
Overprediction	(Mauldin III et al., 2010)	Nov–Jan 2003-04	AmundsenScott	Antarctica	CIMS	Mean (Range)	1.5 to 2.5	N/A	Mean	~2	N/A	(Mauldin III et al., 2001b)
Overprediction	(Kukui et al., 2014)	Dec–Jan 2011-2012	Concordia	Antarctica	CIMS	Mean (All) Peaks (Mean) Mean (range)	3.1 5.2 0.3 to 7.5	0.99* 1.7* 0.1 to 2*	Mean (w/PSS HONO) Mean (w/measured HONO)	0.72 2.19	1.02* 1.84*	N/A
Overprediction	(Dusanter et al., 2009a, b);	March 2006	MexicoCity	Urban	LIF	Peaks (Range) Peaks (Mean)	2 to 15 4.6	0.56 to 4.5 1.9	Mean (13:00 w/o glyoxal) Mean (Morning, polluted) Mean (11:00–14:30) Mean (After 14:30)	2.4 ~0.5 to ~1 1.7 ~1	1.5 0.2 to ~1 ~1 ~1	N/A
Overprediction	(Bloss et al., 2007)	Jan–Feb 2005	Halley	Polar	LIF	Mean (All) Peak (Mean)	0.39 0.79	2.04 4.03	Peak (S1: Conventional) Peak (S2: S1 + halogen oxides) Peak (S3: S2 + possible VOCs)	0.67 1.64 1.27	N/A	N/A
Overprediction	(Holland et al., 2003)	Jul–Aug 1998	Pabstthum	Rural	LIF	Peaks (Range)	6 to 8	5 to 7.4	Mean (Low NO_x)	2	1.4	N/A
Overprediction	(Whalley et al., 2018)	Jul–Aug 2012	Kensington	Urban	LIF	Mean (Noon; S-W air) Mean (Noon; E, polluted air)	~2.2 ~3	~0.2 ~0.5	Mean (Air mass: South-westerly) Mean (Air mass: Easterly, polluted)	1.25 2	~4 10	N/A
Overprediction	(Griffith et al., 2016)	May–June 2010	CalNexLA	Urban	LIF	Peaks (Range) Peaks (Weekdays) Peaks (Weekend)	1.5 to 9 ~4 ~5	0.8* to 10* ~3* ~8*	Mean (Weekend) Mean (Weekday)	1.43 1	0.77* 0.33*	(Volz-Thomas et al., 2003b, a)

Table 2.2b Continued

Comparison results (OH only)	Reference	Time	Location in Figure 1	Site types	Instrument for HO$_x$	Measurement notes	OH conc. 10^6 cm^{-3}	HO$_2$ conc. 10^8 cm^{-3}	Ratio notes	OH R$_{S/O}$	HO$_2$ R$_{S/O}$	Other references targeting the same site
Underprediction	(Hofzumahaus et al., 2009; Lu et al., 2012);	July 2006	BackGarden	Rural	LIF	Peaks (Mean)	15	15	Mean (Range, NO < 1 ppb) Mean (Lu et al., 2012a)	0.2 to 0.33 0.5	N/A	N/A
Underprediction	(Whalley et al., 2011)	Apr–May 2008	DanumValley	Rainforest	LIF	Peaks (Mean)	2.5	3	w/C$_5$H$_8$ recycling mechanism (Peeters et al., 2009)	~0.63	~0.5	(Pugh et al., 2010)
Underprediction	(Liao et al., 2011)	May–June 2007 Jun–Jul 2008	Summit	Polar	CIMS	Mean (2007 spring) Mean (2008 summer)	3.0 4.1	2.7* 4.2*	2007 spring w/o BrO & w BrO 2008 summer w/o BrO & w BrO	0.72 0.78 0.54 0.56	0.87 0.96	(Sjostedt et al., 2007)
Underprediction	(Wolfe et al., 2014)	Aug 2010	Manitou	Forest	CIMS	Peaks (Range)	3 to 10	24.6 to 44.3	Peak	~0.625	0.33	(Kim et al., 2013)
Underprediction	(Tan et al., 2019)	Oct–Nov 2014	Heshan	Suburban	LIF	Peaks (Mean)	4.5	3	Budget analysis only	N/A	1	N/A
Underprediction	(Griffith et al., 2013)	Jul–Aug 2008 Jul–Aug 2009	UMBS	Forest	LIF	Peak (Mean, 2008) Peak (Mean, 2009)	~3.3 ~1.6	~7 ~4.8	Mean (2008) Mean (2008 w/ISOP mechanisms) Mean (2009) Mean (2009 w/ISOP mechanisms)	~0.4 0.9	~0.57 ~1.3 ~0.6 ~1.5	N/A
Underprediction	(Lu et al., 2013a)	Sept 2006	Yufa	Urban	LIF	Peaks (Range) Peaks (Mean)	4 to 17 ~7	2 to 24 ~1.5	Mean (NO < 0.1 ppb) Mean (NO > 1 ppb)	0.38 ~1	~1 ~1	N/A
Underprediction	(Mao et al., 2012)	Jun–Jul 2009	BFRS	Forest	LIF	Peaks (Mean w/ interference) Peaks (Mean w/o interference)	~4.5 ~1.8	N/A	Mean (w/ interference) Mean (w/o interference)	0.32 0.71	N/A	N/A
Underprediction	(Lu et al., 2019)	Summer 2014	Wangdu	Rural	LIF	Peaks (Range noontime)	5 to 15	3 to 14	Mean (NO > 0.3 ppb) Mean (NO < 0.3 ppb, afternoon)	~1 0.5	10 (NO > 4 ppb) N/A	N/A
Underprediction	(Lew et al., 2020)	Jul 2015	IURTP	Forest	LIF	Peaks (Mean)	4	10	Mean (Daytime) Mean (Evening and morning)	0.83 0.50	1.10 to 1.32	N/A
Underprediction	(Lelieveld et al., 2008)	Oct 2005	AmazonSuriname	Forest (Flight)	LIF	Mean (Forest boundary) Mean (Forest free troposphere) Mean (Atlantic boundary) Mean (Atlantic free troposphere)	5.6 8.2 9.0 10.1	10.5 4.9 6.7 5.5	Mean (w/MIM: MPI ISOP mechanism) Mean (w/MIM2+: extra 40% to 80% OH recycle)	0.1 to 0.2 ~1	N/A	N/A

Table 2.2c Continued

Comparison results (OH only)	**Reference**	**Time**	**Location in Figure 1**	**Site types**	**Instrument for HO$_x$**	**Measurement notes**	**OH conc. 10^6 cm^{-3}**	**HO$_2$ conc. 10^8 cm^{-3}**	**Ratio notes**	**OH R$_{S/O}$**	**HO$_2$ R$_{S/O}$**	**Other references targeting the same site**
Good match	(Ren, 2003b, a)	Jun–Aug 2001	NewYork	Urban	LIF	Peaks (Range) Peaks (Mean)	2 to 20 7	0.5 to 6 1	Mean	0.91	0.81	N/A
Good match	(Ren et al., 2006)	Jul–Aug 2002	Whiteface	Forest	LIF	Peaks (Mean)	2.6	4.9	Mean	1.22	0.83	N/A
Good match	(Kanaya et al., 2007b)	Jan–Feb & Jul–Aug 2004	Tokyo	Urban	LIF	Peaks (Mean, winter) Peaks (Mean, summer)	1.5 6.3	0.27 1.4	Peaks (Mean, winter) Peaks (Mean, summer)	0.99 0.81	0.71 1.22	N/A
Good match	(Feiner et al., 2016; Kaiser et al., 2016);	Jun–Jul 2013	Alabama	Forest	LIF	Peaks (Mean)	1	6.64	Peaks (Mean)	~1	~1	N/A
Good match	(Jeong et al., 2022)	Feb–Mar 2014	AmazonBrazil	Forest	CIMS	Peaks (Mean 10:00-15:00) Peaks (Range)	1 ~1 to ~2.8	N/A	Mean	1	N/A	N/A
Good match	(Hens et al., 2014)	Summer 2010	Hyytiälä	Forest	LIF	Mean (Above-Canopy) Mean (Ground)	3.5 ~1.8 to ~1.2	N/A	Mean	1	0.3	(Petäjä et al., 2009; Novelli et al., 2014);
Good match	(Emmerson et al., 2007)	Jul–Aug 2003	WrittleCollege	Urban	LIF	Peaks (Range)	1.2 to 7.5	0.16 to 3.3	Mean	1.24	1.07	N/A
Good match	(Ren et al., 2013)	Apr–May 2009	Houston	Urban	LIF	Peak (Mean)	~8.8	~6.2	Mean	0.9	1.22	(Mao et al., 2010; Chen et al., 2010);
Good match	(Ma et al., 2019)	Nov–Dec 2017	PKU	Urban	LIF	Peaks (Mean clean) Peaks (Mean polluted)	2 1.5	0.4 0.3	Mean (clean) Mean (polluted)	~1 ~0.66	~0.66 0.08	N/A
Good match with missing source	(Whalley et al., 2021)	Summer 2017	IAP	Urban	LIF	Peak (All)	28	10	Mean (NO < 1 ppb)	~1	1.83	(Slater et al., 2020)
Good match with underpredicted HO$_2$	(Zhang et al., 2022b)	Nov–Dec 2019	Shanghai	Urban	LIF	Peaks (Mean)	2.7	0.8	N/A	N/A	N/A	N/A
No comparison	(Kukui et al., 2008)	June–July 2007	Grignon	Suburban	CIMS	Peak (July 6)	~23	~2	N/A	N/A	N/A	N/A
No comparison	(Wang et al., 2021b)	Oct–Nov 2018	PKUSZ	Suburban	LIF	Peaks (Mean)	5.3	4.2	N/A	N/A	N/A	(Wang et al., 2019a)

No comparison	(Rohrer and Berresheim, 2006)	1999–2003	MOHp	Rural	CIMS	Mean (All)	1.97	N/A	N/A		N/A	N/A	(Handisides, 2003);
No comparison	(Zhang et al., 2022a)	Aug–Sept 2019	Chengdu	Urban	LIF	Peaks (Range, PKU-LIF) Peaks (Range, AIOFM-LIF)	1.6 to 15 2.1 to 15.9	N/A	N/A		N/A	N/A	N/A

Notes for Table 2.2:

Mean:	Campaign averaged concentration or ratio
Peak:	Campaign maximum concentration or ratio
Peaks (Mean):	The maximum concentration or ratio for the averaged diurnal or cases result.
Mean (Range):	The daily average concentration or ratio range for the campaign or cases.
Peaks (Range):	The maximum concentration or ratio range for the campaign or cases.
w/ and w/o:	Consider or not consider the specific mechanism, species, or interference.
~:	The result is based on the figure or description without the exact number mentioned in the article.
N/A:	Not available in the article
*:	The HO_2 result including some RO_2 species.

2.2.1 Overestimation of OH by Model

The model overestimation of OH was found in various environments including remote marine boundary layers, coastal, urban, and Artic regions (Table 2.2a). Previous studies have attributed the model overestimation to the overestimation of OH sources, missing OH sinks, and the uncertainty of simulation and observation. For example, model overestimation of OH was found when the dominant sources like HCHO and NO (Zhang et al., 2006), HONO (Kukui et al., 2014), and HO_2 (Kanaya et al., 2007a) were overestimated. The overestimation of OH was resolved when these sources were better constrained in the model. On the other hand, unmeasured VOCs were proposed as missing OH sinks, especially in aged air (McKeen et al., 1997; Carslaw et al., 1999; Berresheim et al., 2002; Creasey et al., 2003; Mauldin III et al., 2010; Griffith et al., 2016). Previous studies have shown evidence of missing OH sinks in the forest (Hansen et al., 2014) and marine regions (Thames et al., 2020), likely from the unmeasured organic compounds from biogenic (Kaiser et al., 2016) or oceanic emissions (Thames et al., 2020) and their oxidation products. Regarding the OH model overestimations caused by simulation and measurement uncertainties, some studies showed the overestimations were within measurement uncertainties (McKeen et al., 1997; Carslaw et al., 1999), while others suggested possible sampling loss of OH (Mauldin III et al., 2010) or possible calibration bias due to the low relative humidity (Mauldin III et al., 2001a).

2.2.2 Underestimation of OH by Model

The model underestimation of OH was mostly found in the forest area with high BVOC emissions (mostly isoprene) and low NO conditions (Table 2.2b) by LIF. The underestimation was attributed to the missing OH sources (Hofzumahaus et al., 2009; Tan et al., 2001a; Lelieveld et al., 2008; Whalley et al., 2011). To explain the possible missing source, a series of new OH regeneration reactions under low NO conditions were proposed from OH oxidation of isoprene experiments in the chamber. The mechanism, known as the Leuven isoprene mechanism (LIM1, Peeters et al., 2014), includes unimolecular reactions (Peeters et al., 2009; da Silva et al., 2010; Fuchs et al., 2013; Novelli et al., 2020) and isomerization of isoprene and/or its products (Peeters and Müller, 2010; Fuchs et al., 2014). With the adoption of this mechanism, the simulated OH concentration increased by 20 to 30% in the forest region (Lew et al., 2020). Another breakthrough is the development of a new chemical scavenging technique in the LIF instruments to better determine the interference to the instrument's background. Some studies show that the interference in LIF instruments can explain 40 to 60% of the previously observed high OH concentrations (Mao et al., 2012; Hens et al., 2014; Novelli et al., 2014; Feiner et al., 2016; Woodward-Massey et al., 2020). With the adoption of interference scavenging and LIM1 improved mechanism, measurements by LIF in an Alabama forest (Feiner et al., 2016). Recently, OH measured by CIMS in the Amazon forests (Jeong et al., 2022) agreed with the LIM1 improved model predicted OH. Whereas, other studies still indicated an underestimation of OH in the model (Tan et al., 2019; Lew et al., 2020).

3. Remaining Challenges

3.1 Limited Field Observation of HO_x

Based on the literature reviews about the measurement techniques and the discrepancy problem, three major challenges remained for future study. At first, more observation is needed to better understand the HO_x chemistry and its impact on air quality. Even though efforts have been made in the last thirty years, as shown in Figure 2.2.1, the measurement of HO_x is scattered and limited around the world. HO_x observation is vital for atmospheric chemistry involved in the production of secondary pollutants in polluted areas and surrounding areas.

The industrialization of the Pearl River Delta (PRD) and Hong Kong (HK) region during the past three decades was accompanied by high anthropogenic emissions of air pollutants (Lu et al., 2013b), causing elevated levels of surface ozone (Wang et al., 2019b) and particulate matters (Yao et al., 2014). Even though sparse measurements of OH in the PRD region were done previously by LIF (Hofzumahaus et al., 2009; Lu et al., 2012; Wang et al., 2019a, 2021a) to study the atmospheric oxidative capacity and impacts on air quality, the measurement is still very limited in the PRD region, and no measurement was performed in Hong Kong. Therefore, the observation of HO_x in the PRD-HK region is desirable.

3.2 The Discrepancy Between Simulation and Observation

Second, more comparison of HO_x simulation and observation by different measurement methods besides LIF is required to better understand the atmospheric oxidation chemistry in low NO_x conditions.

Underestimation of OH in low NO_x high BVOCs conditions was attributed to the interference of LIF. Thus, it is highly desirable to deploy an alternative technique to re-examine the underprediction issue besides the LIF. A recent study in the Amazon forest (Jeong et al., 2022) supports that the use of the CIMS for OH budgets study in the forest region can cross-validate the observation results and provides another aspect for the underestimation problem.

On the other hand, the overestimation found in low NO_x areas like coastal, marine, and polar regions is also important for the understanding of the atmospheric oxidation process, and the fate of trace gases (Zhao et al., 2020b; Tan et al., 2022), and pollution production, as low NO_x aged air mass is where most of the atmospheric oxidation takes place (Brune et al., 2020). Nevertheless, the overestimation received less attention compared to the underestimation issue in recent studies. Additionally, the variable agreement between observed and modeled HO_2 concentration remains to be resolved and also requires more investigation.

3.3 Difficulties in CIMS Development

Finally, it is still a great challenge to perform the HO_x measurement due to its reactive chemical properties. Since the LIF was widely used and was found subject to interferences during development, the alternative CIMS technique is desirable for comparison. However, as a customer–build instrument, CIMS is difficult for new users which explains the fact that CIMS has not been widely used compared to the LIF.

Despite the previous development and application of CIMS for HO_x measurements, applications of this technique remain challenging and are hindered by a lack of detailed experimental procedures to make a CIMS functional. Moreover, isotopic $^{34}SO_2$ used for conversion in the other CIMS is expensive and difficult to obtain due to safety concerns.

3.4 The Aim of This Study

Due to the challenges that remained, this study aims to investigate the atmospheric oxidative capacity and its impacts on air quality in the PRD-HK region by developing a new CIMS system to obtain the ambient levels, and the diurnal variation of OH, and HO_2. The observation results will further compare with the modeling results to investigate the OH discrepancy problem under low NO_x conditions. The development process and measurement principles of the CIMS development will be detail recorded to provide a useful reference to other CIMS users and promote the application of CIMS for HO_x measurement.

4. Development of PolyU CIMS

The chemical ionization mass spectrometer used in this study was originally developed by the Georgia Institute of Technology (Tanner et al., 1997). Compared to the CIMS in previous studies, the PolyU CIMS is not using isotopic SO_2 for OH and HO_2 conversion due to the safety consideration and the restriction of its use by the university. However, without isotopic SO_2, the PolyU CIMS is still capable of not only OH and HO_2 but also H_2SO_4 measurement. Section 4.1 describes the measurement principles for three gases. Then sections 4.2 and 4.3 introduce the components and working theory of the CIMS system and the calibration system, respectively. The comparison of different components and the sensitivity test results of CIMS are shown in section 4.4. Section 4.5 shows the calibration process. Section 4.6 shows the detection limits and the uncertainties measured in the lab. Finally, the residual problem of injection gases is shown in section 4.7.

4.1 Measurement Principles

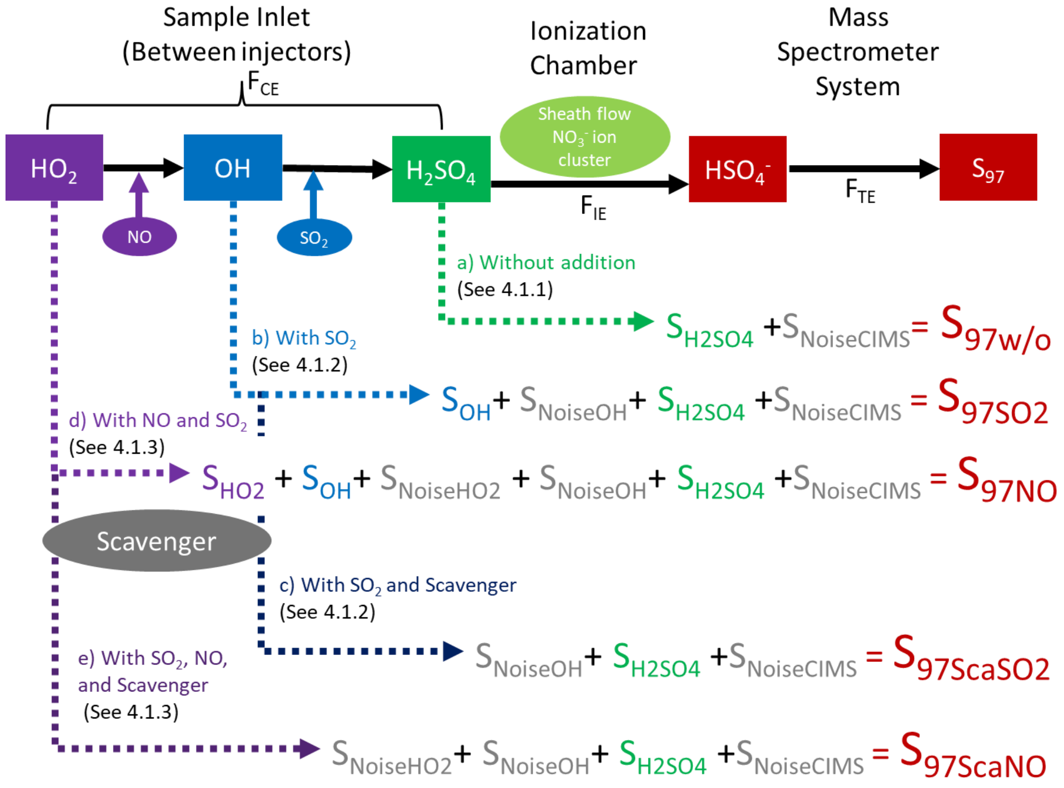

Figure 4.1.1 The flow chart for the relationship between the measurement species and signal intensity at 97 (S_{97}) with different gas injections.

Figure 4.1.1 show the flow chart for measurement principles. The label on the top of the flow chats is the location where the process happens inside the CIMS (refer to Figure 4.2.1). F_{CE}, F_{IE}, and F_{TE} are the efficiency factors affecting the sensitivity and will be discussed later in section 4.4.3. Circled NO, SO_2 and scavengers are the gases added to the front injectors. S_{97} refers to the signal intensity detected by CIMS at m/z 97 and the affixed label after S_{97} ($S_{97w/o}$, S_{97SO2}, S_{97NO}, $S_{97ScarSO2}$, $S_{97ScaNO}$) refers to the S_{97} measured directly by CIMS when different gases are added to the sample flow. The measured species affixed label (S_{H2SO4}, S_{OH}, S_{HO2}, $S_{NoiseOH}$, $S_{NoiseHO2}$, and $S_{NoiseCIMS}$) refer to the signals that corresponded to the species concentration or interferences. These signals are not provided by CIMS measurement directly. See details in the following sections.

4.1.1 H_2SO_4 Measurement Principle

The measurement principle H_2SO_4 is the foundation principle for CIMS measurement since the HO_2 and OH are converted to H_2SO_4. Therefore, the measurement principle of H_2SO_4 is the common part of OH and HO_2 measurement.

The ambient H_2SO_4 in the sample flow is converted into HSO_4^- by chemical ionization in reaction with the NO_3^- primary reactant ions:

R 4.1 $H_2SO_4 + NO_3^- \cdot (HNO_3)_m \cdot (H_2O)_n \rightarrow HSO_4^- \cdot (HNO_3)_m(H_2O)_n + HNO_3$

$\mathrm{NO_3^-} \cdot \mathrm{(HNO_3)_m} \cdot \mathrm{(H_2O)_n}$ are cluster ions with m and n mostly of 0 - 2 and 0 - 3 (Berresheim et al., 2000). These cluster ions are generated by the reaction of HNO_3 vapor with electrons (Fehsenfeld et al., 1975):

R 4.2 $HNO_3 + e^- \rightarrow NO_2^- + OH$

R 4.3 $HNO_3 + NO_2^- \rightarrow NO_3^- + HONO$

R 4.4 $NO_3^- + (HNO_3)_m + (H_2O)_n + M \rightarrow NO_3^- \cdot (HNO_3)_m \cdot (H_2O)_n + M$

Where $\mathrm{e^-}$ is emitted from an ion source. The ion clusters are subsequently dissociated in the collisional dissociation chamber (CDC):

R 4.5 $NO_3^- \cdot (HNO_3)_m \cdot (H_2O)_n + M \rightarrow NO_3^- + (HNO_3)_m + (H_2O)_n + M$

R 4.6 $HSO_4^- \cdot (HNO_3)_m \cdot (H_2O)_n + M \rightarrow HSO_4^- + (HNO_3)_m + (H_2O)_n + M$

As shown in Figure 4.1.1 a) the H_2SO_4 is finally detected by a mass spectrometer system as $\mathrm{HSO_4^-}$ at 97 m/z (S_{97}). Since no additional gases were added to the sample flow through front injectors, the signal is further marked as $S_{97w/o}$. Due to the excess reagent ion NO_3^-, the H_2SO_4 is completely ionized. However, the noise signal of the instrument is hard to eliminate. Thus, the $S_{97w/o}$ correlated to the H_2SO_4 contributed signal S_{H2SO4} and noise signal $S_{NoiseCIMS}$ from the instrument. The $S_{NoiseCIMS}$ is determined during calibration. Then the signal contributed by H_2SO_4 can be calculated as follows.

E 4.1 $$S_{H2SO4} = S_{97w/o} - S_{NoiseCIMS}$$

4.1.2 OH Measurement Principle

Ambient OH radical is measured by converting it to H_2SO_4 by adding SO_2 into the sample flow. The addition of SO_2 initiates the chemical conversion sequence in the presence of oxygen and water vapor as mentioned previously.

R 1.24 $$OH + SO_2 + M \rightarrow HSO_3 + M$$

R 1.25 $$HSO_3 + O_2 \rightarrow SO_3 + HO_2$$

R 1.26 $$SO_3 + 2H_2O \rightarrow H_2SO_4 + H_2O$$

Then the OH is converted to H_2SO_4 goes through the same process and is detected as S_{97}. Since the SO_2 is added through the injector for conversion, the signal is further marked as S_{97SO2} (Figure 4.1.1b). The S_{97SO2} is not only contributed by the ambient signal corresponding to OH (S_{OH}) but also ambient H_2SO_4 concentration (S_{H2SO4}), the previously mentioned interference from CIMS ($S_{NoiseCIMS}$), and other interference signals marked as $S_{NoiseOH}$. The $S_{NoiseOH}$ includes the signals corresponding to artificial OH formed by primary ion creation, recycled OH from HO_2 triggered by NO, ambient criegee intermediates, the interference signals due to the addition of scavenger gases and other possible interference from ambient air.

To mitigate the $S_{NoiseOH}$ for better performance, the scavenger gases were added to the CIMS from three positions. Firstly, they are added to the sheath flow to mitigate the effect of artificial OH which is the unwanted OH radicals formed from primary ion creation (R 4.2).

R 4.2 $$HNO_3 + e^- \rightarrow NO_2^- + OH$$

Another flow of scavenger gas is added into the sample flow via rear injectors to reduce the reaction time of conversion to prevent the HO_2 recycled reaction triggered by ambient NO in the conversion region and the ionization chamber.

R 1.8 $RO_2 + NO + O_2 \rightarrow R'HO + NO_2 + HO_2$

R 1.9 $HO_2 + NO \rightarrow OH + NO_2$

See section 4.4 for the optimization of reaction time by the flow rate adjustment. However, the criegee intermediates (see the conversion from criegee intermediates to H_2SO_4 in Mauldin III et al., 2012), ambient H_2SO_4, and other possible interference are inevitably contribute to the S_{97}. Besides, the noises mentioned above also cannot be completely removed. Therefore, the scavenger gases are also added to the sample flow together with SO_2 to eliminate the ambient OH radical and measure a background signal ($S_{97SO2Sca}$, Figure 4.1.1c,). In this case, the S_{97} corresponds to H_2SO_4 (S_{H2SO4}) and the interference ($S_{NoiseOH}$). Thus, the ambient OH corresponded signal (S_{OH}) can be determined by subtracting the signals ($S_{97SO2Sca}$) correlated with criegee intermediates, H_2SO_4, and other interference from the S_{97SO2} as shown in the following equation.

E 4.2 $S_{OH} = S_{97SO2} - S_{97SO2Sca}$

The injection positions of scavenger gases are shown in Figure 4.2.1. See details about scavenger gas selection and their elimination efficiency in Section 4.4.3.5.

4.1.3 HO_2 Measurement Principle

Compared to the OH measurement principle, the HO_2 requires an additional conversion for measurement. As shown by R 1.9, ambient HO_2 can be converted to OH and further detected by CIMS. The addition of NO into the sample flow together with SO_2 from the front injectors can indirectly measure HO_2 by converting ambient HO_2 to OH (R 1.9) and then to H_2SO_4 (R 1.24 to R 1.26) for detection. It is worth noting that in the OH detection, the R 1.9 causes an interference; however, it becomes the key reaction during HO_2 measurement. The signals obtained with the addition of SO_2, and NO are labeled as S_{97NO} (Figure 4.1.1d). Similar to the OH measurement, the HO_2 measurement also suffers from an interference signal and is noted as $S_{NoiseHO2}$. Therefore, the scavenger gas applied for OH radical can also determine the background signal during HO_2 measurement ($S_{97NOSca}$) which corresponds to ambient H_2SO_4 ($S_{97H2SO4}$), and both the interference of HO_2 ($S_{NoiseHO2}$) and OH ($S_{NoiseOH}$) as shown in Figure 4.1.1e. It is note that, the $S_{Noise\ HO2}$ and $S_{NoiseOH}$ including the interference that caused by the addition of scavenger gases. Then the S_{HO2} can be subtracted from the following equation.

E 4.3 $$S_{HO2} = S_{97NO} - S_{97NOSca} - S_{OH}$$

In the troposphere, the HO_2 concentration is 2 orders of magnitude greater than OH. Thus, the S_{HO2} can be approximated to $S_{97NO} - S_{97NOSca}$.

R 1.8 $$RO_2 + NO + O_2 \rightarrow R'HO + NO_2 + HO_2$$

The RO_2 species will also contribute to the HO_2 signal by R 1.8. As indicated in the previous study, the interference of RO_2 in HO_2 measurement is negligible when the RO_2 species produced from the H-atom subtraction reaction like the OH reacts with methane and ethane. However, the RO_2 species produced from OH-addition to the alkene like isoprene, and methacrolein or aromatic precursors will have a higher reaction rate with NO and affect the HO_2 measurement (Fuchs et al., 2011). Therefore, the HO_2 measurement in remote low BVOC conditions like the second and third field studies in this thesis is not affected by the RO_2 interference.

4.2 CIMS System

Figure 4.2.1 shows the schematic and the photo of the PolyU CIMS system. The CIMS measures the ambient OH concentration when connecting to the stainless-steel inlet, and, during calibration, the calibrator is connected to the CIMS instead. The chemical conversion region is the area between the front and rear injectors in the sample inlet system. In this region, H_2SO_4 is formed by the chemical conversion from OH (R 1.24 to R 1.26) or HO_2 (R 1.9 and R 1.24 to R 1.26). Then the H_2SO_4 is ionized into HSO_4^- ion cluster in the chemical ionization region. The ion cluster further transfers to the mass spectrometer system through a pinhole by the force of the electric field. The mass spectrometer system consists of three parts including a collisional dissociation chamber (CDC) for ion cluster dissociation, an ion guide chamber (IGC) to refocus the ions, and an ion detection chamber (IDC) for ion detection and electric signal generation.

R 1.24 $OH + SO_2 + M \rightarrow HSO_3 + M$

R 1.25 $HSO_3 + O_2 \rightarrow SO_3 + HO_2$

R 1.26 $SO_3 + 2H_2O \rightarrow H_2SO_4 + H_2O$

R 1.9 $HO_2 + NO \rightarrow OH + NO_2$

It is noted that, in Figure 4.2.1, the blue color highlights the name of flows, the red color highlights the injectors, the purple color highlights the ion sources, and the green color highlights the modifications for simultaneous measurement for HO_2 (NO/N_2 Front Flow) and H_2SO_4 (Front Valve).

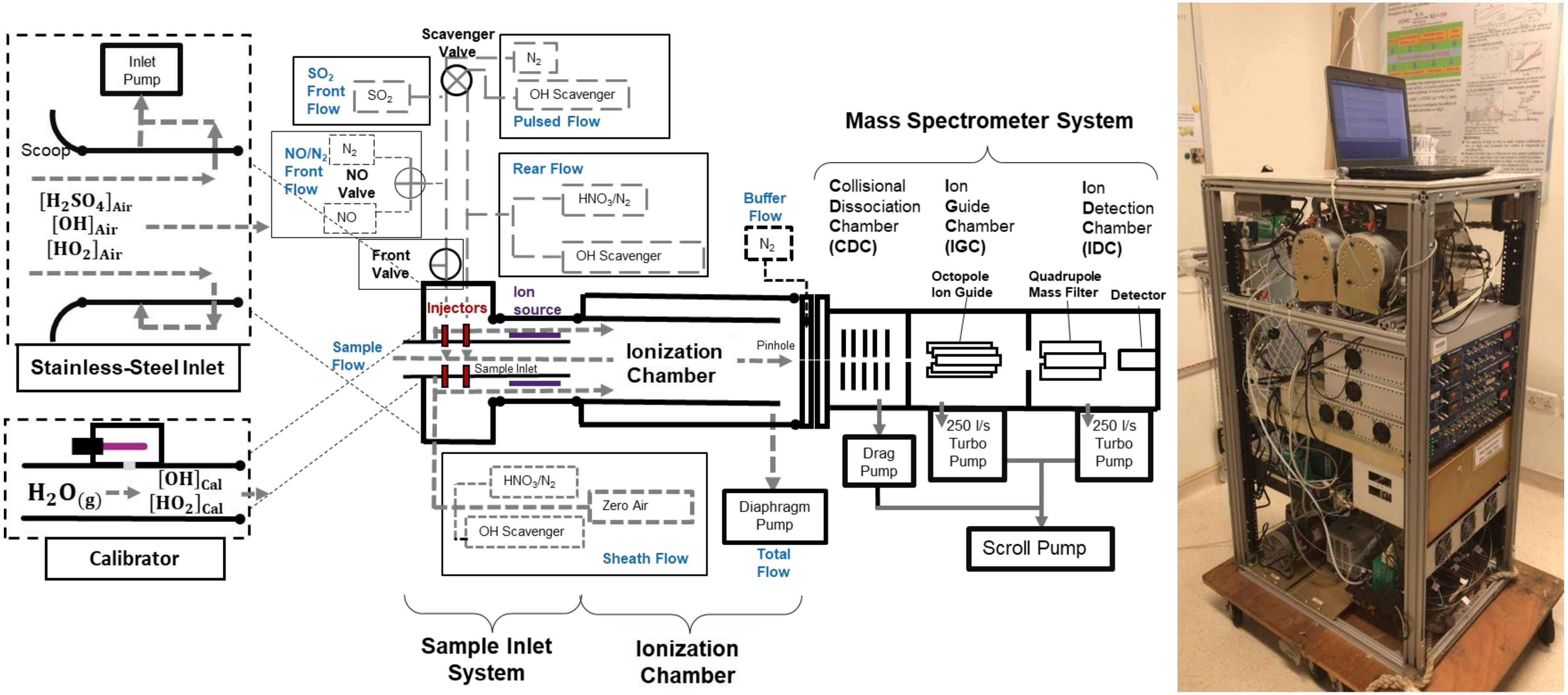

Figure 4.2.1 Schematics of the CIMS system which consists of a stainless-steel inlet, a sample inlet, an ionization chamber, a mass spectrometer system, and a calibration system. The photo of the PolyU CIMS shown on the right. The aluminum frame supports the CIMS to measure the ambient air both horizontally and vertically.

4.2.1 Sample Inlets System and the Conversion Region

As shown in Figure 4.2.1, during ambient sampling, the air sample at ambient temperature and pressure is first drawn into a 5 cm diameter, 32 cm long stainless-steel tube. A turbulence-reducing scoop is attached to the front of the tube to avoid the eddy influence at high wind speeds and create a laminar flow to minimize the contact between airflow and the inlet surface (Tanner et al., 1997). The flow velocity at the center of the tube is 5 m/s, which is measured manually using a pitot. The residual time in the stainless steel is less than 0.1s and the sampling loss is nearly constant (Tanner et al., 1997). The central part of the air is then drawn through a 1.6 cm diameter stainless steel inlet into the chemical conversion region with the flow rate being determined by a mass flow controller (MKS, MFC company). The excess flow in the tube is vented back into the atmosphere via the inlet pump.

The sample inlet in Figure 4.2.1 is equipped with two pairs of stainless-steel needle injectors that are placed in opposite positions. The first (front injectors) pair is installed at a 69 mm distance from the stainless sample inlet. The second pair (rear injectors) are installed at 25.8 mm from the front injectors. The front injectors introduce different gases to trigger the chemical conversions of the CIMS and determine the measurement targets. The rear injectors on the other hand terminate all conversions by introducing scavenger gases to the sample flow and eliminating the remained HO_2 and recycled OH. The space between the front and rear injectors is the chemical conversion region. The conversion between HO_2 and OH to H_2SO_4 as described in sections 4.1.2 and 4.1.3 mainly takes place in this region.

During the H_2SO_4 measurement, no additional gases are added to the sample flow through the front injectors. The front valve is switched off and guides all gases to the exhaust flow instead of to the sample flow. In this case, the signal ($S_{97w/o}$) obtained by CIMS is correlated to ambient H_2SO_4 (S_{H2SO4}) and the instrumental noise ($S_{NoiseCIMS}$) as mentioned in Section 4.1.1. The noise for the instrument is determined during calibration. Then the signal of ambient H_2SO_4 can be determined by simple subtraction shown in E 4.1 mentioned above.

E 4.1 $S_{H2SO4} = S_{97w/o} - S_{NoiseCIMS}$

To measure OH radicals, the 99.999 vol.% N_2 and 0.9 vol.% SO_2 are added to the sample flow through the front injectors to convert OH into H_2SO_4 (R 1.24 to R 1.26).

R 1.24 $OH + SO_2 + M \rightarrow HSO_3 + M$

R 1.25 $HSO_3 + O_2 \rightarrow SO_3 + HO_2$

R 1.26 $SO_3 + 2H_2O \rightarrow H_2SO_4 + H_2O$

The function of the scavenger valve in Figure 4.2.1 is to switch the injection position of the scavenger gases to measure the total signals (S_{97SO2}) or the background signals ($S_{97ScaSO2}$). As discussed above, to eliminate the interference during OH measurement, another flow is added through a pulsed flow controlled by a zero-dead space four-way electrically operated valve, which automatically switches the injection positions of scavenger gas and pure N_2 to change measurement modes. When the scavenger gas is added through the front injectors to the sample flow, N_2 is switched through the rear injectors, the CIMS is then running in background mode. Under this condition, atmospheric OH simultaneously reacts with SO_2 and the scavenger gas, with the reaction of OH with scavenger gas being much faster than SO_2. This configuration produces background signal $S_{97SO2Sca}$ from the interferences of OH measurement (e.g., atmospheric H_2SO_4) with negligible contribution from atmospheric OH. When the scavenger gas and N_2 are switched into the sample flow through the rear and front injectors, respectively, CIMS is running in signal mode. Atmospheric OH is all converted by SO_2, and the total signal S_{97SO2} is produced. Similarly, the signal corresponding to OH (S_{OH}) can be determined by E 4.2 mentioned above.

E 4.2 $S_{OH} = S_{97SO2} - S_{97SO2Sca}$

In the measurement of HO_2, the 1 vol.% NO is added to the sample flow together with SO_2 for the conversion of HO_2 to OH and then to H_2SO_4 (R 1.9 and R 1.24 to R 1.26). The NO/N_2 front flow in Figure 4.2.1 is controlled by a zero-dead space four-way electrically operated valve (the NO Valve in Figure 4.2.1) and switches the injection flow between NO and N_2 automatically.

R 1.9 $HO_2 + NO \rightarrow OH + NO_2$

Similar to the OH measurement, the scavenger valve is switched automatically to create the total signal S_{97NO} and background signal $S_{97NOSca}$ during HO_2 measurement when NO is added together with SO_2 in the sample flow. Then the HO_2 signal (S_{HO2}) can be calculated by E 4.3 mentioned above.

E 4.3 $S_{HO2} = S_{97NO} - S_{97NOSca} - S_{OH}$

The concentration of OH, HO_2, and H_2SO_4 can be calculated by the following equations, respectively.

E 4.4 $[H_2SO_4] = \frac{1}{C_{OH}} \times \frac{S_{H2SO4}}{S_{64}}$

E 4.5 $[OH] = \frac{1}{C_{OH}} \times \frac{S_{OH}}{S_{64}}$

E 4.6 $[HO_2] = \frac{1}{C_{HO2}} \times \frac{S_{HO2}}{S_{64}}$

Where the C_{OH} is the calibration factor for OH and H_2SO_4 and the C_{HO2} is the calibration factor for HO_2. The determination of calibration factors is shown in section 4.5. S_{H2SO4}, S_{OH} and S_{HO2} are the signals corresponding to measured species and calculated from subtractions mentioned above E 4.1 to E 4.3. S_{64} is the signal corresponding to the reagent ions (NO_3^-). As discussed in Berresheim et al. (2000), the absolute concentration of the H_2SO_4 and reagent ion (NO_3^-) is not required as the concentration is determined based on their relative signal strength and the calibration factor. Therefore, the signal strength is represented by the signal ratio between S_{97} (HSO_4^- ion) and S_{64} (NO_3^- ion).

4.2.2 Chemical Ionization Region

The sample flow through the chemical conversion region is then drawn into the chemical ionization region and mixed with the sheath flow (Figure 4.2.1). The sheath flow is continuously drawn into the same region through an annular space between a 3.5 cm o.d. outer tube and a 1.2 cm o.d. sample tube by a diaphragm pump (KNF-813). These tubes are concentric with the downstream end of the chemical conversion region. The sheath gas is produced by a zero-air generator (Thermo Electron Corporation, Model 111) attached with active charcoal and silica gel to remove trace gases such as SO_2 and NO_x. Before entering the ionization region, HNO_3 vapor and the scavenger gas are added continuously to the sheath flow. The HNO_3 vapor is obtained by N_2 carrier gas passing through the headspace of a reservoir of concentrated liquid HNO_3. When HNO_3^- doped sheath gas passes through the ion source (Figure 4.2.1), $\mathrm{NO_3^-\cdot(HNO_3)_m\cdot(H_2O)_n}$ reactant ions are produced by the reaction of HNO_3 and electrons. Additionally, the N_2-carried HNO_3 is also added through the rear injector to maintain the ion cluster distribution and further improve the stability of the reagent ion signal (Sjostedt et al., 2007).

The $\mathrm{NO_3^-\cdot(HNO_3)_m\cdot(H_2O)_n}$ reactant ions then react with H_2SO_4 molecules from the sample air to form $\mathrm{HSO_4^-\cdot(HNO_3)_m(H_2O)_n}$ cluster ions in the chemical ionization region according to R 4.1.

R 4.1 $H_2SO_4 + NO_3^- \cdot (HNO_3)_m \cdot (H_2O)_n \rightarrow HSO_4^- \cdot (HNO_3)_m(H_2O)_n + HNO_3$

Voltages are applied to the sample and sheath flow tubes to produce an electrical field to force the reactant ions to the center of the chemical ionization region and enhance the interaction of reactant ions with H_2SO_4. The optimization of voltages for better sensitivity is shown in Section 4.4.3.

The total flow (Figure 4.2.1) is then exhausted at the end of the chemical ionization region through diaphragm pumps (Thomas, SK-668) and controlled by an MFC. To prevent the HNO_3 vapor from corroding the pump and the MFC and polluting the ambient air, the exhaust flow is first filtered through active charcoal cartridges and then vented back into the atmosphere at a distance of > 10 m from the sampling point. A small portion of the total flow is drawn into the mass spectrometer system through a 101.6 μm diameter pinhole. A counterflow of N_2 buffer gas is added to the atmospheric pressure side of the pinhole (Figure 4.2.1) to prevent unwanted clusters and molecules from entering the pinhole (Berresheim et al., 2000). Voltages are added at the positions of the N_2 buffer and pinhole to force the ions into the mass spectrometer system.

4.2.3 Mass Spectrometer System

The mass spectrometer system is separated into three differentially pumped chambers with two adjacent chambers being connected through a 4 mm pinhole (Figure 4.2.1). The first chamber behind the pinhole is a collisional dissociation chamber (CDC). The pressure of the CDC is typically maintained at around 0.5 hPa through a drag pump (Adixen, MDP 5011) and a scroll pump (Agilent Technologies, IPD-3). The CDC has a high ion kinetic energy (i.e. high electric field to number density ratio), and most of the entered cluster ions (e.g. $\mathrm{HSO_4^-} \cdot (\mathrm{HNO_3})_\mathrm{m}(\mathrm{HO_2})_\mathrm{n}$ and $\mathrm{NO_3^-} \cdot (\mathrm{HNO_3})_\mathrm{m} \cdot (\mathrm{HO_2})_\mathrm{n}$) are dissociated in the CDC through R 4.5 and R 4.6 mentioned previously.

R 4.5 $NO_3^- \cdot (HNO_3)_m \cdot (H_2O)_n + M \rightarrow NO_3^- + (HNO_3)_m + (H_2O)_n + M$

R 4.6 $HSO_4^- \cdot (HNO_3)_m \cdot (H_2O)_n + M \rightarrow HSO_4^- + (HNO_3)_m + (H_2O)_n + M$

The second chamber is an octopole ion guide high vacuum chamber (IGC). In this chamber, the pressure is maintained at about 1.3×10^{-3} hPa through a turbo molecular pump (Agilent Technologies, TwisTorr 304 Fs) and the same scroll pump mentioned above. Here, the ions from the CDC are refocused by an octopole ion guide and transported to the third chamber.

The third chamber (IDC) contains a quadrupole mass filter and detector with attached signal amplifier electronics. The mass-selected ions of the quadrupole are amplified and detected by a channeltron ion multiplier and then counted based on standard techniques (Sjostedt et al., 2007). This chamber maintains a pressure of about 2.6×10^{-5} hPa through another turbo molecular pump and the same scroll pump.

4.3 Calibration System

4.3.1 Calibration Unit and Principle

The calibration of the CIMS is achieved by controlled concentrations of OH and HO_2 radicals, which are produced through photolysis of water vapor by 184.9 nm light (Tanner and Eisele, 1995):

R 4.7 $H_2O + hv\ (184.9\ nm) \rightarrow OH + H$

R 4.8 $H + O_2 + M \rightarrow HO_2 + M$

The calibration factor C is then determined based on the produced OH and HO_2 concentrations and detected signals of HSO_4^- and NO_3^- according to the measurement principle.

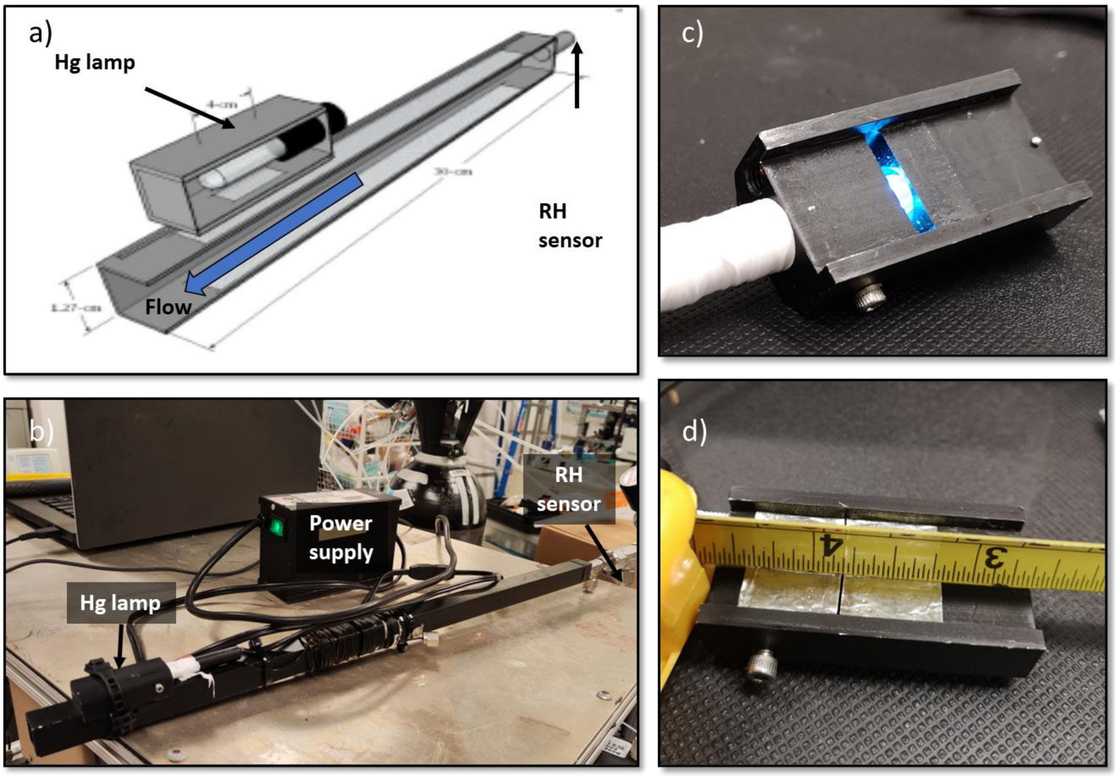

Figure 4.3.1 The Calibration System. a) Schematic diagram of the calibration system. b) The photo of the calibration system. c) The original gap for the lamp. d) The narrowed gap for lower transmission. It is noted that when the calibrator connects to

CIMS, the gap of the Hg lamp is less than 1 cm from the sample inlet. The reactions triggered by the radicals before the conversion reactions are negligible.

Figure 4.3.1a and b show the diagram and the photo of the main components of the calibration system, respectively. The system consists of a cuboid stainless steel tube, a hygrometer, and an optical element. The length of the cuboid stainless steel tube is 52 cm with a 1.6 cm side length. The high-precision capacitance humidity measurement hygrometer (Vaisala, HMP100) is connected at the front of the tube to measure the temperature T and dew point temperature T_d of the mixed air. The optical elements are mounted at the end of the tubes (air outlet side) to minimize the wall loss during calibration. This element consists of a Pen Ray mercury lamp (Analytik Jena, UVP Pen Ray) and a bandpass filter. The bandpass filter blocks most of the emitted photons except those at 184.9 nm. Finally, the transmitted light enters the tube and photolyzes water vapor to produce OH and HO_2 radicals according to R 4.7 and R 4.8. The mixing ratio of water vapor in the airflow is controlled through the mix of the dry synthetic air and humidity air from a water bubbler.

When the calibration tube was applied for calibration with the original gaps for light transmission (Figure 4.3.1c), the OH radicals produced by the calibration system is more than 100 times larger than the ambient concentration. Therefore, to achieve a lower calibration concentration for higher accuracy, the gap for light transmission was reduced by aluminum-foil paper as shown in Figure 4.3.1d. The following section shows the result after such modification.

4.3.2 Quantification of the Calibration System

4.3.2.1 HO_x Quantification

The concentrations of OH and HO_2 radicals produced from the water vapor photolysis reaction during calibration can be described as follow:

E 4.7 $$[HO_2\,] = [OH] = I \times t \times \sigma_{H_2O} \times \phi_{H_2O} \times [H_2O]$$

where *I* and *t* are the photon intensity (unit: photons s^{-1} cm^{-2}) and the reaction time of H_2O photolysis, respectively. In the calibration system, the *I* and *t* are determined at the same time and considered as one factor. The determination of *It* is described in the next section (4.3.2.2). [HO_2], [OH], and [H_2O] are the concentrations of HO_2 OH radicals and water vapor, respectively, $\sigma_{\mathrm{H_2O}}$ is the photolysis cross-section of water vapor at 184.9 nm (7.14×10^{-20} cm^2, Cantrell, et al. 1997) and $\phi_{\mathrm{H_2O}}$ represents the photolysis quantum yield, which is assumed to be 1.0 at 184.9 nm. [H_2O] is calculated according to the temperature (T), saturated water vapor pressure ($P^{\circ}_{H_2O}$) and relative humidity (RH) of the mixed air flow (Kürten et al., 2012).

4.3.2.2 *It* Value Quantification

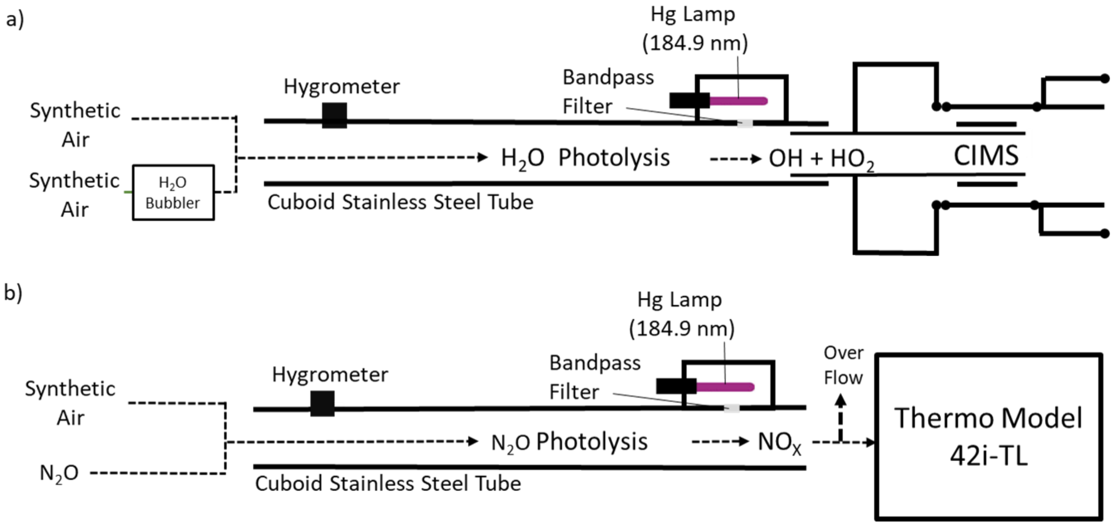

Figure 4.3.2 Schematic diagram of calibration processes. a) The CIMS calibration experiment. b) The N_2O actinometry experiment for determination of product *It* value.

The product *It* is determined based on the chemical actinometry method (Figure 4.3.2b). This method measures NO_x generated from N_2O photolysis with the same calibration system under the same condition as that for the CIMS calibration. Since

N_2O photolysis and H_2O photolysis require the same photon intensity (184.9 nm), the product *It* of H_2O photolysis can be determined by measured NO_x and N_2O mixing ratios produced by N_2O photolysis (Edwards et al., 2003).

Briefly, high-purity N_2O (99.9%) mixed with dry synthetic gas flows into the calibration system. The photolysis of N_2O generates NO_x through the following reactions (Edwards et al., 2003):

R 4.9 $N_2O + hv\ (184.9\ nm) \rightarrow N_2 + O(\,^1D)$

R 4.10 $O(\,^1D) + O_2 \rightarrow O(\,^3P) + O_2$

R 4.11 $O(\,^1D) + N_2 \rightarrow O(\,^3P) + N_2$

R 4.12 $O(\,^3P) + O_2 + M \rightarrow O_3 + M$

R 4.13 $O(\,^1D) + N_2O \rightarrow 2NO$

R 4.14 $O(\,^1D) + N_2O \rightarrow N_2 + O_2$

The O_3 produced from R 4.12 could oxidize NO to NO_2. Therefore, the photolysis of N_2O eventually converts it to NO_x which is concurrently measured by a commercial NO_x detector (Thermo, Model 42i-TL) The combined product *It* is a function of the mixing ratios of N_2O, N_2, O_2, and produced NO_x:

E 4.8
$$It = \frac{(K_{37}\times[O_2]+K_{38}\times[N_2]+(K_{40}+K_{41})\times[N_2O])\times[NO_X]}{2\times K_{40}\times\sigma_{N_2O}\times\phi_{N_2O}\times[N_2O]^2}$$

Where K_{37}, K_{38}, K_{40}, and K_{41} are the rate constants of R 4.10, R 4.11, R 4.13, and R 4.14, respectively. $\sigma_{\mathrm{N_2O}}$ is the absorption cross-section of N_2O, and $\phi_{\mathrm{N_2O}}$ represents the photolysis quantum yield. The values for them can be found in the previous study (Kürten et al., 2012).

Ideally, the N_2O actinometry experiment should be conducted with the same flow rate as in the H_2O photolysis experiment such that the reaction time can be the same. However, at the flow rate suitable for CIMS calibration (10 slpm), the concentration of NO_x produced from N_2O photolysis is near the detection limit of the NO_x detector. Hence, the N_2O actinometry experiment was carried out at a lower flow rate (3 and 6 slpm) to increase the reaction time for photolysis and then the NO_x production. The *It* values for the lower flow rate (It_{HLOW}) and higher flow rate (It_{HIGH}) have the following relationship:

E 4.9 $$It_{HIGH} = \frac{FR_{LOW} \times It_{LOW}}{FR_{HIGH}}$$

where FR_{LOW} and FR_{HIGH} represent different flow rates. Based on this equation, It_{HIHG} can be obtained by scaling It_{LOW} with the ratio of FR_{LOW} and FR_{HIGH}. The E 4.9 is validated in the next section.

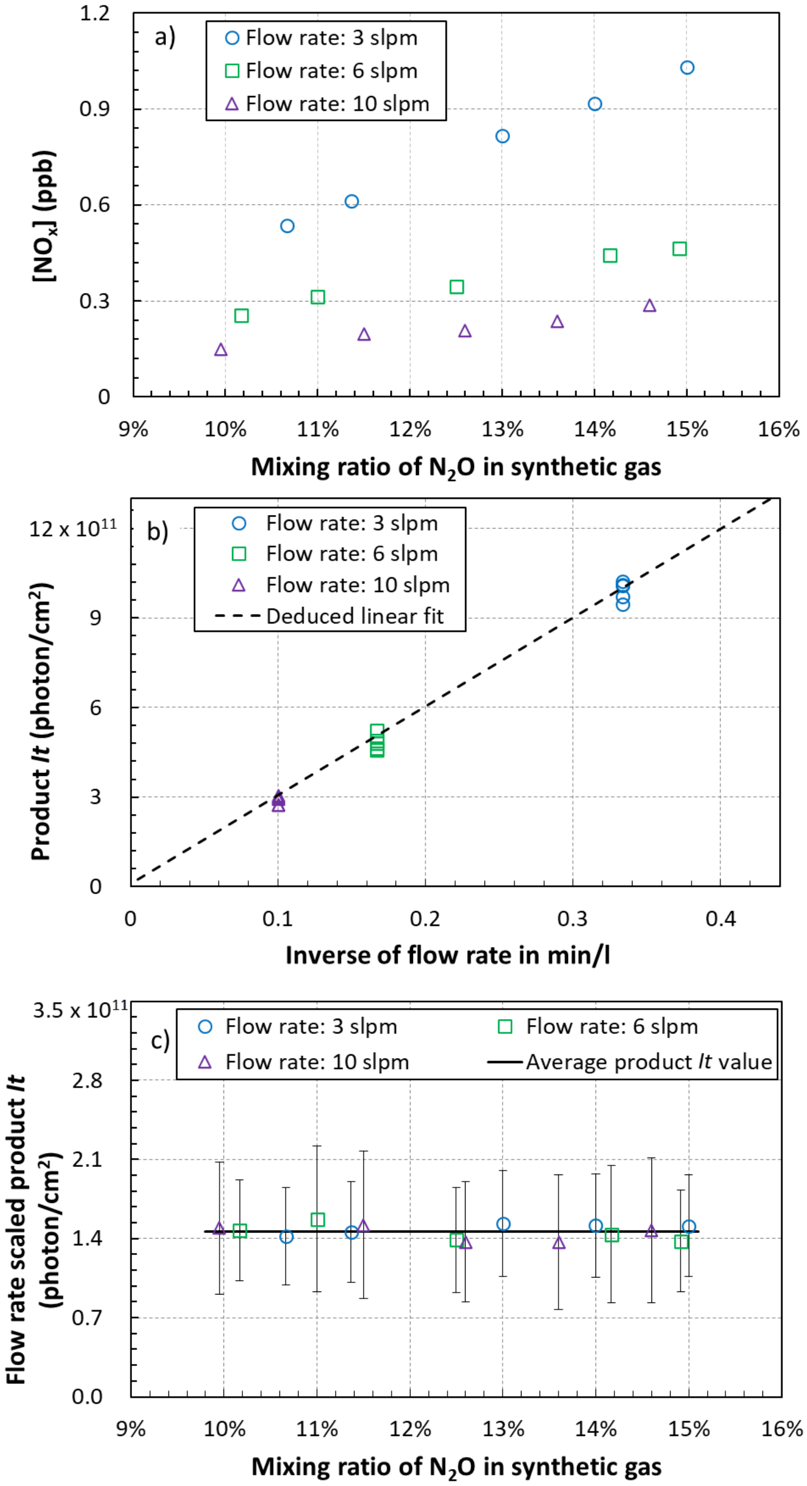

Figure 4.3.3 The results of the N_2O actinometry experiment. a) The produced NO_x concentration as a function of the N_2O mixing ratio. Different colors represent different flow rates. b) The product *It* as a function of the inverse of flow rate (see detail in text). c) The flow rate scaled product It as a function of the N_2O mixing ratio, which was obtained by scaling product It with the ratio of flow rates (3, 6, and 10 slpm) to 10 slpm.

Figure 4.3.3 shows the results of the N_2O actinometry experiment. The black line is the average value of the flow rate scaled product It and the error bars show the standard deviation. Figure 4.3.3a shows the NO_x produced as the function of N_2O mixing ratios from 10% to 15% at different flow rates (FR_{N_2O} = 3, 6, and 10 slpm). Generally, an increase in the N_2O mixing ratio or a decrease in reaction time (lower flow rate) led to more production of NO_x. In Figure 4.3.3b, the product *It* corresponding to different flow rates was calculated according to E 4.9 based on the result in Figure 4.3.3a. The product *It* linearly increased with the inverse of the flow rate, which validates the linear dependency between product *It* and the inverse of the flow rate shown in Figure 4.3.3b. This linear dependency is consistent with the result of Kurten et al. (2012). In addition, the product *It* was independent of the N_2O mixing ratios in the range of 10% to 15% (Figure 4.3.3c). Based on the E 4.9, the flow rate scaled *It* (It_{HIGH}) is calculated from It_{LOW} in Figure 4.3.3b multiplying the ratio of FR_{LOW} (3, 6, and 10 slpm, respectively) to FR_{HIGH} (10 slpm). The *It* varied from 1.37 to 1.53 × 10^{11} at different flow rates and N_2O mixing ratios. The mean value of 1.46 × 10^{11} photon cm^{-1} was adapted for It_{HIGH}. Then based on the calculated It values and E 4.7, the calibration can be performed. See section 4.5 for the example of calibration results during the field study.

4.3.3 Application of the Calibration System

After determining the value of *It*, the [OH] and [HO_2] concentrations produced by the calibration system can be calculated. By applying the calibration system to the CIMS (Figure 4.3.2a), the calibration can proceed and the calibration factors for OH and HO_2 can be determined by coupling E 4.5 and E 4.6 with E 4.7, respectively.

E 4.4 $$[H_2SO_4] = \frac{1}{C_{OH}} \times \frac{S_{H2SO4}}{S_{64}}$$

E 4.5 $$[OH] = \frac{1}{C_{OH}} \times \frac{S_{OH}}{S_{64}}$$

E 4.6 $$[HO_2] = \frac{1}{C_{HO2}} \times \frac{S_{HO2}}{S_{64}}$$

Besides that, with the addition of known [SO_2] to the calibration flow, this calibration system can calibrate the $H_2SO_{4(g)}$ sensitivity of not only the QCIMS but also the Tof-CIMS (Chen et al., 2022a). More importantly, the calibration system provides a stable [OH] and [HO_2] for the CIMS sensitivity tests. Section 4.4 and section 4.5 show the details of the optimization of CIMS and the calibration results for field studies after optimization are shown, respectively.

4.4 CIMS Optimizations

As shown in Figure 4.2.1, the CIMS system is complicated, and its performance is affected by different parameters and components. In this section, we present the tests result for different types of ion sources and scavenger gases (propane and C_3F_6), comparison of primary ions detection, and optimization of the instrument sensitivity and noise. This section emphasizes the discussion of different selections and the ideas of optimization, instead of the exact specification of CIMS, because the specification of CIMS was changed during three campaigns due to the change of measurement targets and settings. The difference in the CIMS technical specification for different campaigns and the reason for changes are shown in section 5.2.

4.4.1 Ion Source

Radioactive ion source (^{210}Po or ^{241}Am) and corona discharge source (corona ionizer) have been used as the ion source in previous studies (Berresheim et al., 2000; Sjostedt et al., 2007; Kukui et al., 2008). In this study, ^{210}Po and corona sources were compared.

^{210}Po emits alpha particles that interact with the carrier gas to quickly form thermalized electrons and positive ions (Fehsenfeld et al., 1975). The formed electrons react with O_2 and then HNO_3 to produce $NO_3^- \cdot (HNO_3)_m \cdot (H_2O)_n$ reactant ions. ^{210}Po was used due to its low OH interference and ease of installation. Corona ionizer generates NO_3^- by discharge formed between a tungsten needle and a 1 mm diameter plate 3 mm from the needle tip (Kukui et al., 2008). The corona source has the advantage of producing much higher concentrations of $NO_3^- \cdot (HNO_3)_m \cdot (H_2O)_n$ primary ions compared with radioactive ^{210}Po or ^{241}Am foils, which leads to higher concentrations of HSO_4^- and higher signal intensities (and higher sensitivities). However, the corona discharge source is known to produce a significant number of neutral species including OH radicals (artificial OH), which means the noise is relatively high (Kukui et al., 2008).

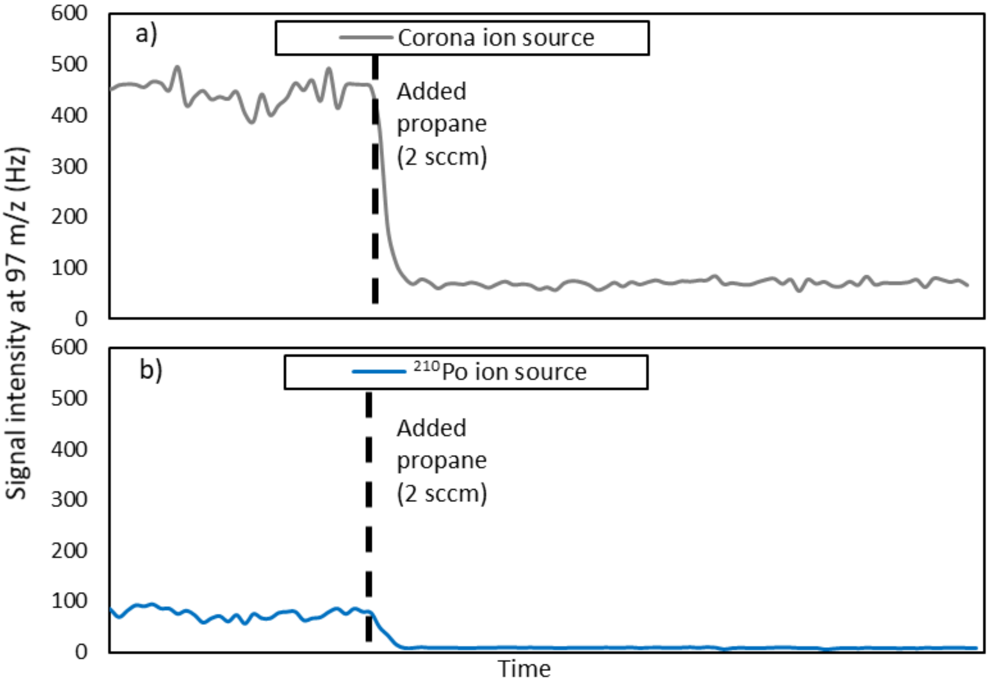

Figure 4.4.1 Signal intensity at 97 m/z when using a) corona and b) ^{210}Po as the ion source. The SO_2 flow rate was 5 sccm.

We compared a ^{210}Po ions source and a corona source (Figure 4.4.1). The result showed that the detection limit of the CIMS with the ^{210}Po ion source was lower than that with the corona source due to larger noise in the corona source. We previously applied the corona source in the same CIMS to measure peroxy radicals (RO_2 and HO_2 without OH), and the noise level was acceptable compared to the ambient concentration of peroxy radicals. For OH measurement, although a scavenger gas was added in the sheath flow to remove most artificial OH radicals, the remaining interferences were still high compared to ambient OH concentrations.

In this study, ^{210}Po foils were chosen as the ion source in our CIMS system. It should be noted, however, that a radioactive source like ^{210}Po is often subject to strict health safety regulations, and the users need to apply for a permit to use and transfer the radioactive source. In addition, ^{210}Po undergoes alpha decay to stable ^{206}Pb with a half-life of about 140 days. Therefore, in order to keep stable signal intensities for primary ions, the ^{210}Po foils need to be replaced regularly.

4.4.2 Primary Ions Detection

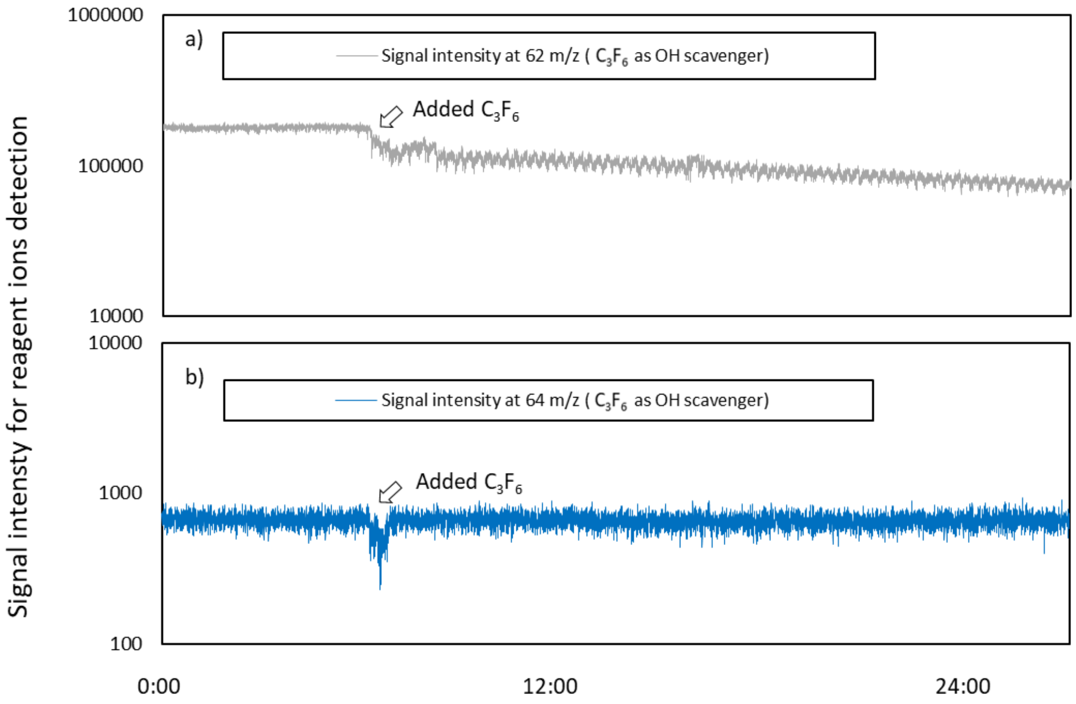

Figure 4.4.2 Signal intensity at a) 62 m/z and b) 64 m/z for reagent ion detection by an aged detector when using C_3F_6 as a scavenger.

Determination of the concentrations needs to use the signal intensities of NO_3^- ions (S_{62} or S_{64}) according to E 4.4 to E 4.6. Some previous researchers traced the NO_3^- ions on the signal intensities at 62 m/z (S_{62}, Tanner et al., 1997; Sjostedt et al., 2007; Kukui et al., 2012). We found that the concentrations of NO_3^- in the inlet system was extremely high (Figure 4.4.2a before the addition of C_3F_6). Even though a small portion of the NO_3^- ions were finally detected by the mass detector, the signals were enough for measurement (Figure 4.4.2b before the addition of C_3F_6). After operating the CIMS by detecting the signal of NO_3^- ions at 62 m/z about a year, all signals from the channeltron detector dropped significantly compared to one year ago which may be due to the accelerated aging of the detector by the high concentrations of NO_3^- ions. Additionally, the aged detector is also more vulnerable to the suppression effect of the addition of C_3F_6 and the change from S_{64} to S_{62} can mitigate this decrease. Figure 4.4.2a shows the signal continuously decreases after the C_3F_6 suppression when using S_{62}. Such suppression recovers after time when applying the S_{64} as the reagent ion as shown in Figure 4.4.2b. Note that the scales on the y-axis of Figure 4.4.2 a) and b) are different.

Therefore, the isotopic signal ($N^{18}O_3^-$) at 64 m/z (S_{64}) was chosen to detect NO_3^- primary ions for extended operation. The signal intensity at 64 m/z is lower than at 62 m/z by about a factor of 167.

4.4.3 Sensitivity Optimization

The sensitivity (S) of the CIMS instrument to the H_2SO_4, OH, and HO_2 radicals depend on their conversion efficiency to H_2SO_4 in the chemical conversion region (F_{CE}), the ionization efficiency of H_2SO_4 to HSO_4^- in chemical ionization region (F_{IE}), and the transmitted efficiency of HSO_4^- from sample inlet to mass spectrometer system (F_{TE}):

$$S \sim F_{CE} \cdot F_{IE} \cdot F_{TE}$$

F_{CE} is dependent on the reaction time and the reactant concentrations. Due to different reactions path for OH and HO_2 to convert to H_2SO_4, this factor changes along with different measurement targets. During H_2SO_4 measurement, $F_{CE\text{-}H2SO4} = 1$ due to no conversion is needed. However, during the measurement of OH ($F_{CE\text{-}OH}$) and HO_2 ($F_{CE\text{-}HO2}$), the conversion efficiency factors are affected by the $[SO_2]$ and the $[NO]/[SO_2]$ ratio, respectively. F_{IE} is affected by the flow dynamics, which determines the mixing of flows, and the electric field inside the ionization region, which forces the $NO_3^- \cdot (HNO_3)_m \cdot (HO_2)_n$ primary ions to the center of the region for H_2SO_4 ionization. The F_{TE} is related to the N_2 buffer and the induced electrical field in the pinhole area which determines the number of ions that can access the mass spectrometer system.

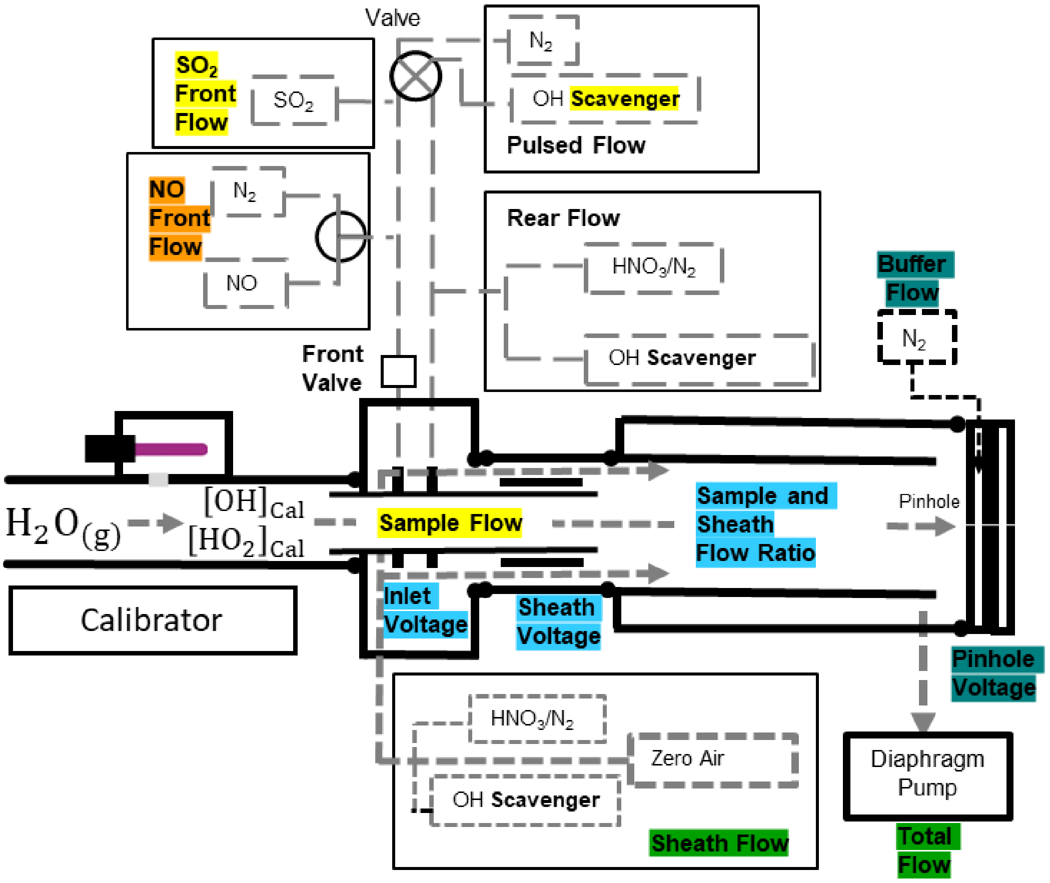

Figure 4.4.3 The sample inlet system and conversion region diagram of the CIMS with adjustable voltages and flows for a sensitivity test.

Figure 4.4.3 shows the inlet system of the CIMS. In order to produce OH and HO_2 signals, the calibrator is applied, and the flows of the calibrator are maintained at the same flow rates, RH, and temperature to produce stable radical concentrations for the test. The adjustable flow rates and voltages are labeled based on the factors they correlated to. During the sensitivity test, the calibrator is applied to the CIMS to maintain OH and HO_2 concentration at a certain level. Yellow labels the sample flow, SO_2, and scavenger flow relating to the $F_{CE\text{-}OH}$. The orange labels NO flow that needs to be considered additionally for conversion efficiency $F_{CE\text{-}HO2}$ during HO_2 measurement. Blue labels sample and sheath flow ratios and their voltages relating to the F_{IE}. The total and sheath flow indirectly determine the sample flow rate and further the sample and sheath ratio and are labeled in green. Finally, buffer flow and pinhole voltages affect the F_{CE} and are labeled in dark green.

The sensitivity of OH is optimized first for OH and H_2SO_4 measurement by determining the optimal F_{CE-OH}, F_{IE}, and F_{TE}. The F_{CE-OH} is first optimized for the maximum conversion of the ambient OH to H_2SO_4 by adjusting the SO_2 flow and the sample flow rate. Then, to achieve the best F_{IE} for H_2SO_4 ionization, the flow dynamic and electric field are optimized by adjusting the sample/sheath flow ratio and the voltages applied to the sample and sheath flow. Finally, the N_2 buffer flow rate and the voltages of the pinhole are adjusted to control the F_{TE} to determine the amounts of ions entering the detector. During the optimization, the calibration tube is applied to produce OH radicals and control their concentration.

The conversion efficiency factor F_{CE-HO2} for HO_2 measurement is determined at last by adjusting the [NO]/[SO_2] ratio with settled SO_2 flow after the CIMS is optimized for OH and H_2SO_4 measurement.

In order to compare the adjustment result, the signal is normalized in Figure 4.4.4 based on the signal intensity at the settings of 10 sccm SO_2, 16.8 slpm total flow, 12.6 slpm sheath flow, 3.7 slpm sample flow, 440 sccm N_2 buffer flow, -80 V sheath voltage, -32 V inlet voltage, and 41% relative humidity of the sample air. Red dashed lines highlight the optimized values selected for PolyU CIMS. It is noted that the red dashed line in the following figures in this section were the optimized settings applied for our CIMS.

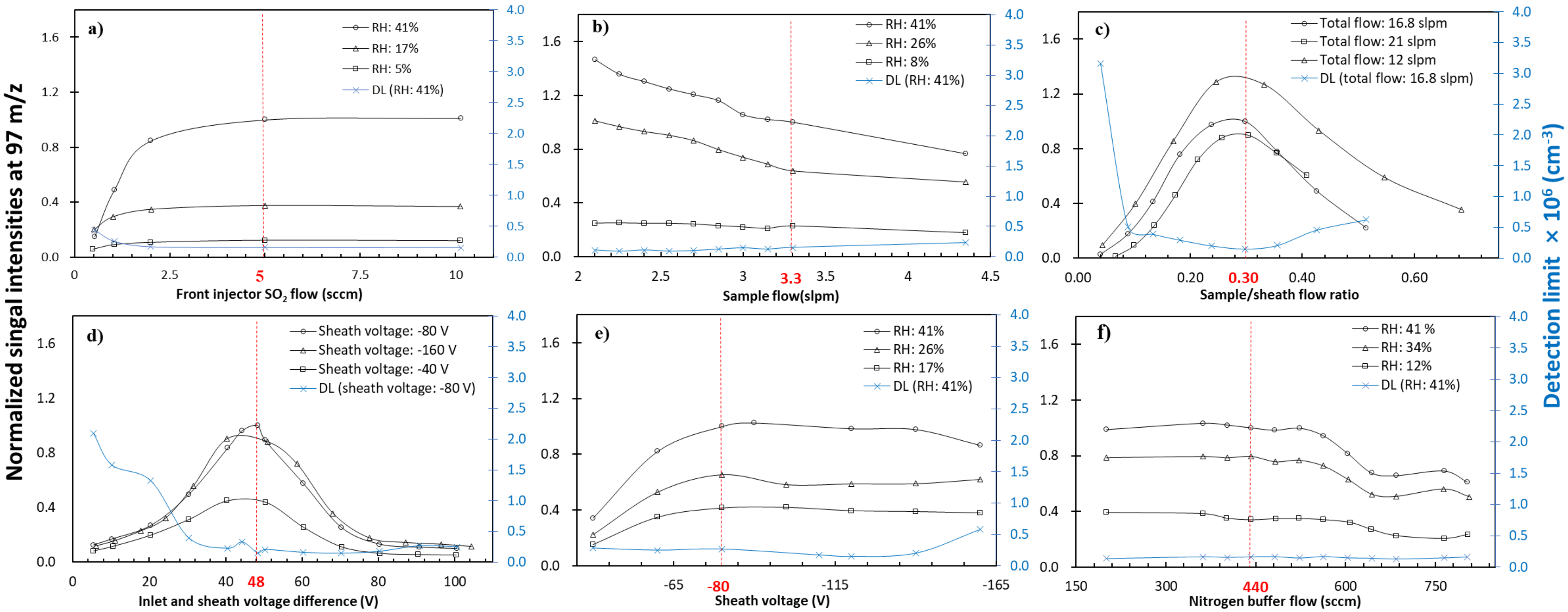

Figure 4.4.4 The normalized signal intensity at 97 m/z and detection limit as a function of a) SO_2 flow rate b) sample flow with fixed sample/sheath flow ratio, c) sample/sheath flow ratio, d) inlet and sheath voltages difference, e) sheath voltage with the fixed voltage difference between inlet and sheath voltages, f) N_2 buffer flow with the other parameters constant.

4.4.3.1 Conversion Efficiency

Figure 4.4.4a shows the normalized signal intensity (NSI) at 97 m/z for HSO_4^- as a function of the flow rate of SO_2 (0.9 vol.%). The NSI first increased with increased SO_2 and reached a stable level at a flow rate > ~2.5 sccm, which did not vary with the relative humidity. This result indicates that the SO_2 concentration at the flow rate of 2.5 sccm was adequate to convert sampled OH to H_2SO_4. Since the concentration of OH radical produced by the calibration system during optimization was 1 to 2 magnitudes higher than that in ambient conditions, the 2.5 sccm flow of SO_2 is adequate for ambient measurement. In field studies, the SO_2 flow rate of the CIMS was set at larger than 5 sccm with a factor of 2 margins, following the previous study (Sjostedt et al., 2007).

The effects of the sample flow rate on NSI are shown in Figure 4.4.4b. During the adjustment of the sample flow rate, if the sheath flow rate remains the same, not only the conversion time but also the flow dynamics in the ionization chamber will be affected. Thus, in order to show the effect of conversion time on NSI only, the sheath flow was adjusted along with the sample flow to maintain the sample/sheath flow rate ratios and control the F_{IE} in Figure 4.4.4b. Briefly, the NSI increased with the decrease in sample flow rate, which can be explained by a longer OH conversion time (R 1.24 to R 1.26) and a higher F_{CE} at a lower flow rate. However, the increased reaction time will also increase the OH interference produced from HO_2 recycling in the presence of NO in sample air. Previous studies usually kept the reaction time less than 60 ms to mitigate such interference (e.g. Tanner et al., 1997). After considering the reaction time and interference, the sample flow rate was set at 3.7 slpm, which gives a reaction time of ~47 ms. After the above selection of the SO_2 concentration and sample flow rate, the optimal F_{CE} is determined.

4.4.3.2 Ionization Efficiency

Figure 4.4.4c shows the NSI as a function of the ratio of sample flow to sheath flow in the ionization region. The NSI first increased and then decreased with the increased ratio, with a peak value at a sample/sheath flow ratio of 0.3. This optimized ratio was independent of the total flow rates from 12 to 21 slpm. This ratio produced a turbulent flow in the chemical ionization region. Such flow dynamics facilitate a fast mixing of the reactants and enhance the F_{IE} of H_2SO_4 as well as the NSI at 97 m/z (Tanner and Eisele, 1995; Tanner et al., 1997).

Figure 4.4.4d-e shows the change of NSI by different voltages applied to the sample and sheath flow. The NSI first increased and then decreased as the increase of the difference in voltage between the sample and the sheath flow (Figure 4.4.4d). At the voltage difference of 48 V, the peak NSI was achieved, and this voltage difference is selected. Figure 4.4.4e shows the NSI increased with the negative sheath voltage and then kept stable with the sheath voltage < -70 V. This shows that when it is negatively charged, it is the voltage difference but not the exact voltage that affects the NSI. In later studies, the inlet and sheath voltages of the CIMS were set at -32 V and -80 V, respectively.

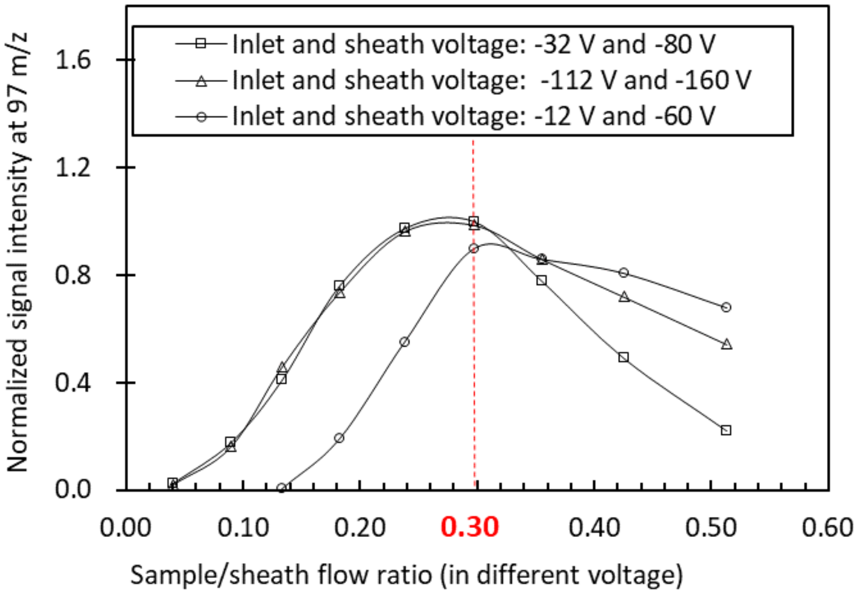

Figure 4.4.5 The normalized signal intensity at 97 m/z as a function of sample/sheath flow ratio at different voltages

The cross interactions of sample/sheath flow and voltages on NSI were also evaluated (Figure 4.4.5). The result shows that the highest NSI was achieved when the sample/sheath flow ratio was close to 0.3, independent of the voltages. The optimized F_{IE} of the CIMS is achieved by the above selections of the flow ratio and electric field.

4.4.3.3 Transmission Efficiency

The N_2 buffer flow rate controls the proportion of sample air in dry N_2, thereby affecting the amount of ion cluster in the sample air entering the mass detector. Figure 4.4.4f shows that the NSI increased with the decreased buffer flow rate, as expected. However, a lower flow rate of N_2 buffer gas also allows more undesired neutral molecules and particles in sample air to enter the mass spectrometer (Berresheim et al., 2000). With these considerations, the flow rate of N_2 buffer gas was set as 440 sccm (Figure 4.4.4f). To force the ions to the center of the pinhole, the voltage applied before and on the pinhole was optimized similarly and set at -70 V and -40 V, respectively (figure not shown).

4.4.3.4 Conversion Efficiency of HO2

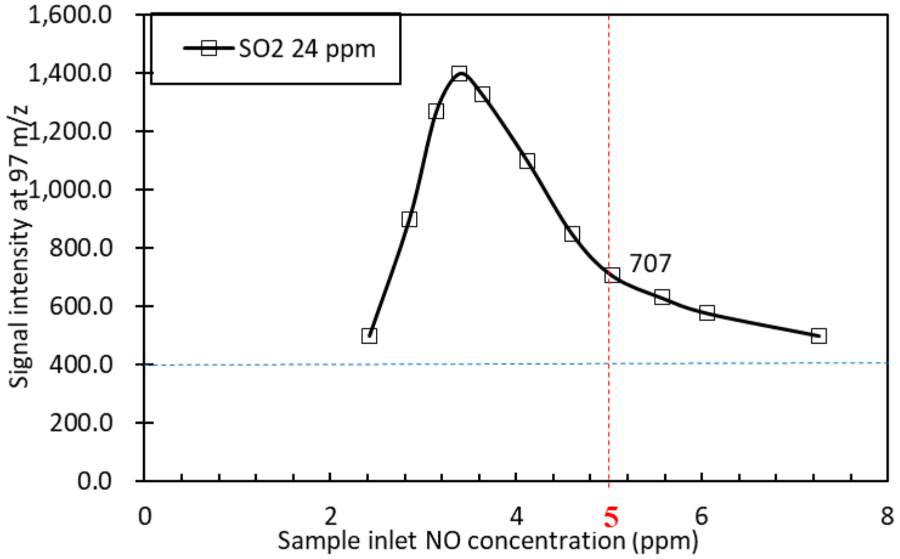

Figure 4.4.6 Signal intensity at 97 m/z versus nitric oxide concentration at a fixed sulfur dioxide concentration of 24 ppm.

The addition of NO gas through the front injector can convert peroxy radicals to OH and further be detected by CIMS as S_{97} (R 1.9).

R 1.9 $HO_2 + NO \rightarrow OH + NO_2$

However, as a competitive reaction, the excess levels of NO can cause the formation of HONO and prevents the OH from being detected by the CIMS (R 1.15).

R 1.15 $OH + NO \rightarrow HONO$

Therefore, the key parameter for HO_2 measurement is the [NO] to [SO_2] ratio and the reaction time of the conversion. As shown in Figure 4.4.6, with the fixed SO_2 concentration in sample flow, the Hz 97 signal detected by CIMS increases with the increase of the [NO] in sample flow to a distinct maximum. As the [NO] further increases (larger than 3.4 ppm in this case), the R 1.15 becomes important and the OH radical trends to react with NO to form HONO instead of being converted by SO_2. Thus, the Hz 97 signal decreases with the increase of [NO] after peaking at 3.4 ppm.

The final ratio of [NO] to [SO_2] selected for the campaign is approximately 1:5 to achieve a detection efficiency of 0.6. In this ratio, the sensitivity would not change dramatically alone with the change of NO concentration and provide a relatively stable sensitivity. Conversely, in larger reaction times, the Hz 97 corresponding to HO_2 increases due to more complete conversion, as described by (Edwards et al., 2003). However, in our CIMS the chemical conversion from HO_2 to H_2SO_4 (R 1.9 and R 1.24 to R 1.26) occurred in the same conversion region (Figure 4.4.3) where OH is converted to H_2SO_4. This means that the increase in HO_2 conversion time will also increase the conversion time of OH and cause unwanted interference in OH measurement as discussed above. Thus, the reaction time remains at a low level for both HO_2 and OH conversion.

4.4.3.5 Noise Minimization and Scavenger Gas

After optimization of CIMS's sensitivity, noise minimization is needed to reduce the signal that is not related to the ambient OH. As discussed above, the noises for OH measurements include interference in ambient air and artificial OH produced by the ion source. The artificial OH is mitigated by adding the scavenger gas in the sheath flow (front injectors) and the ambient interference is quantified by the scavenger gas switching between the front and rear injector for the subtraction shown in Figure 4.2.1. In previous studies, propane, C_3F_6, and NO_2 have been used as scavenger gases by different groups (Berresheim et al., 2000; Sjostedt et al., 2007; Kukui et al., 2008). In this section, we determine the optimal scavenger flow rates for the CIMS operation and then compare different scavenger gases during application.

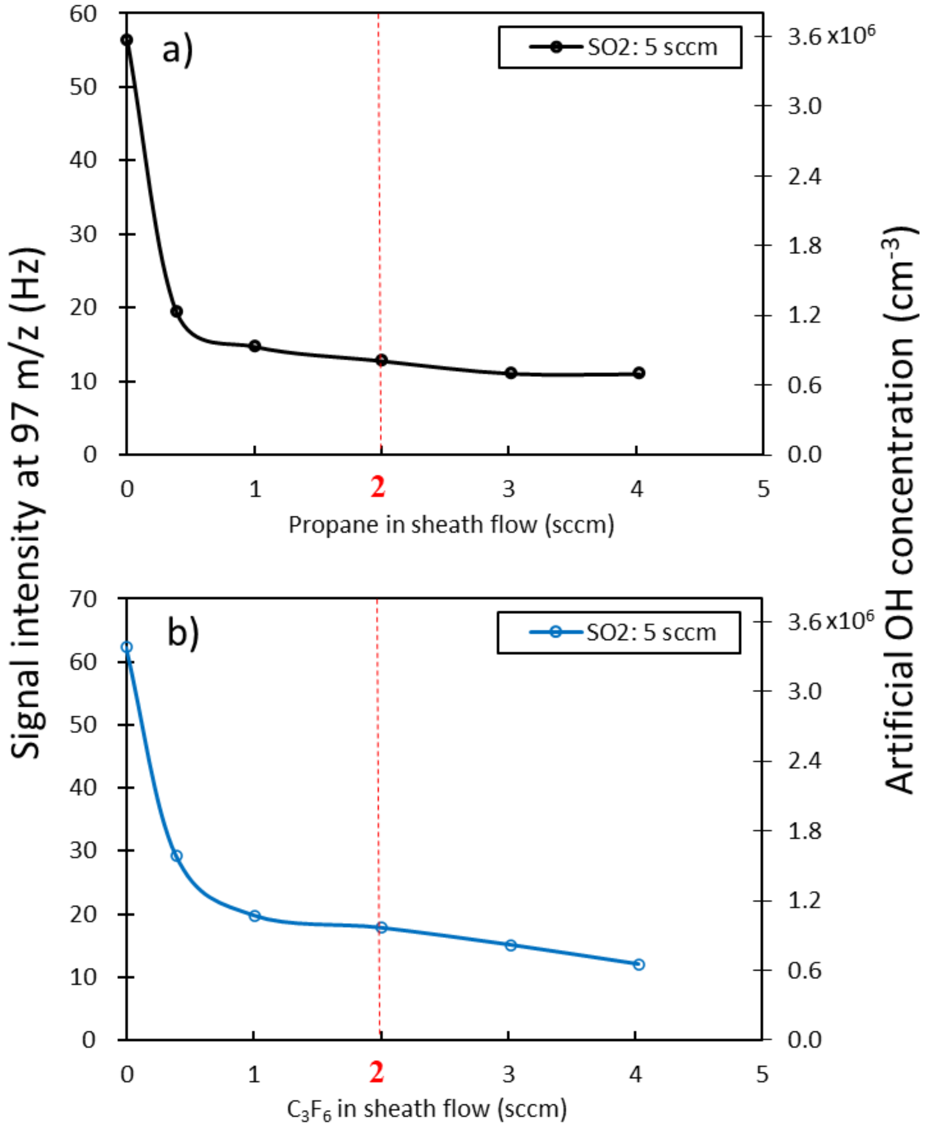

Figure 4.4.7 Artificial OH signal as a function of a) propane and b) C_3F_6 flow rate added in sheath flow, respectively.

To test the artificial OH, N_2 gas was used as sample air so that there were no OH radicals in the sample air. As shown in Figure 4.4.7, the artificial OH concentration from the ^{210}Po ion source was around 3.5×10^6 cm^{-3} when the scavenger gas was not added through the sheath flow. Such noise was comparable to the ambient OH concentration, when scavenger gases were added to the sheath flow, the artificial signals were reduced with the increasing scavenger flow and kept stable at ~1×10^6 molecules cm^{-3} when the flow rate was higher than 1 sccm. The flow of scavenger gas in the latter field campaign was set at larger than 2 sccm in the sheath flow.

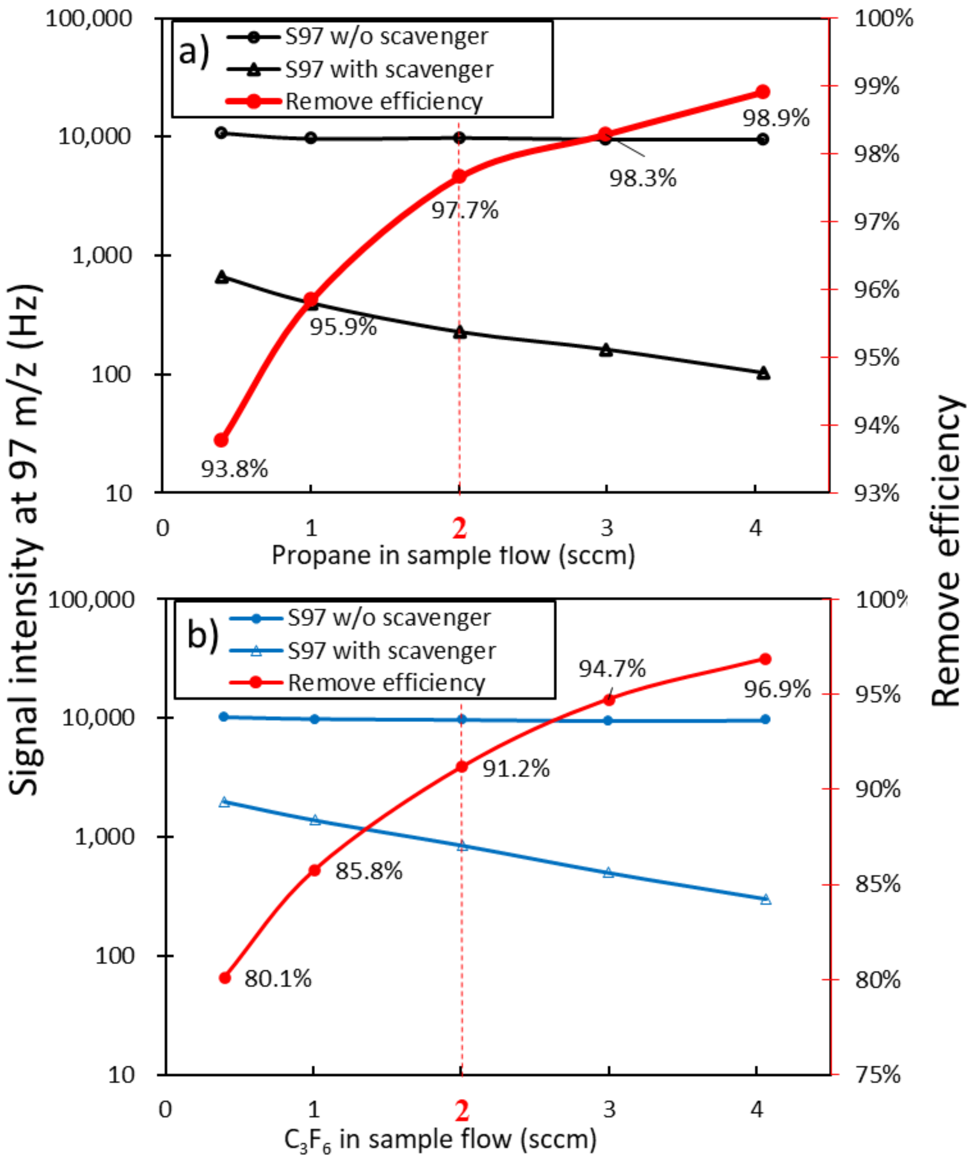

Figure 4.4.8 Signal intensity at 97 m/z and the OH removal efficiency as a function of the change of a) propane and b) C_3F_6 flow rate added to the sample flow.

Figure 4.4.8 shows that the removal efficiency (RE) of OH increased with the increased scavenger flow rate initially and leveled off at the flow rate > 2 sccm for propane with the unchanged SO_2 flow rate. However, the RE of C_3F_6 kept increasing with the increase of scavenger flow. We adopted the flow rate of 2 sccm for comparison, which led to more than 90% removal efficiency for OH in two scavenger gases. As OH concentrations produced by the calibration system are higher than those in typical ambient air, the RE of the scavenger is appropriate for ambient measurement. The interference introduced by the scavenger gases where estimated when the scavenger gases were added through the front injector ($S_{97ScaSO2}$, and $S_{97ScaNO}$). Such interference was eliminated by the subtractions as shown in Figure 4.1.1 when calculating the OH and HO_2 concentrations.

Figure 4.4.7 and Figure 4.4.8 show that pure propane (99.95 vol.%, Harvest Wise Gases (H.K.) Limited) has a higher efficiency than pure C_3F_6 (99.95 vol.%). Thus, theoretically, propane is a better scavenger for OH radical elimination with a lower price compared to C_3F_6 (2~3 times higher). However, the by-product of OH elimination by propane causes interference in HO_2 measurements. Thus, for the OH and HO_2 measurement, the use of C_3F_6 as scavenger gases is preferred.

Compared to propane, the signal removal efficiency of C_3F_6 is around 90% when 2 sccm is added as an elimination for both OH and HO_2 measurements. It is noted that the C_3F_6 suppressed the signal intensities detected by the mass detector. This suppression was recovered with a new detector. However, when the detector was aged, such suppression caused a continuous decrease in the reagent signal as shown in Figure 4.4.2. This problem can be mitigated by changing reagent ions as previously mentioned. Even though the C_3F_6 elimination efficiency is lower, has a signal suppression problem, and the price is more expensive when compared to propane, it is the best option for HO_x measurement and is widely applied in not only CIMS but also LIF.

NO_2 can also be a candidate for scavenger gas (Kukui et al., 2008), but is not discussed in this study since the high purity of NO_2 as a scavenger is not available due to the safety restriction in Hong Kong. In this thesis, we used both propane and C_3F_6 as scavenger gas for different campaigns. See the detailed discussion in section 5.2 about the setting changes of CIMS in three field campaigns.

4.5 Calibration Result

The calibrations were done for CIMS at different times of day with varying temperatures, humidity, and solar intensity, and the calculated calibration factors seem only related to the change of settings of the CIMS.

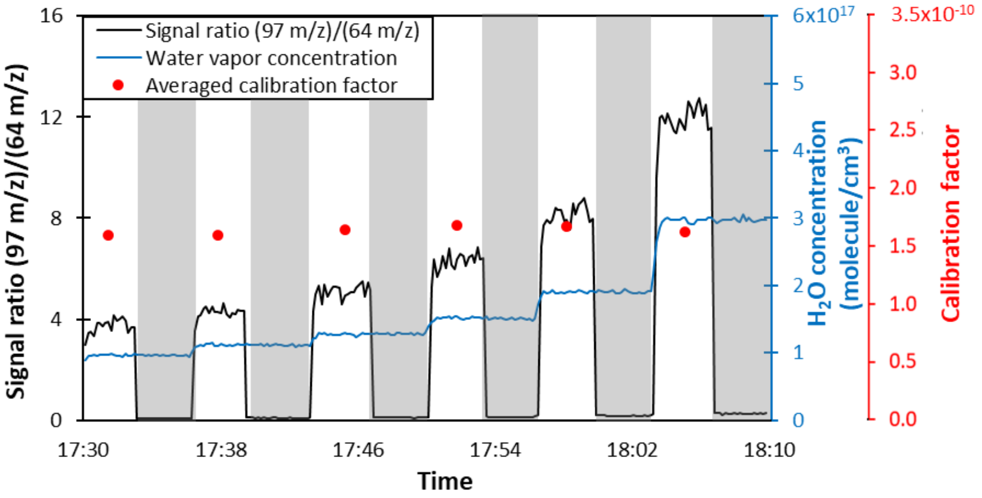

Figure 4.5.1 The time series showing calibration results.

Figure 4.5.1 shows an example of a typical procedure for determining the calibration factor in the field study. Gray-labeled areas represent the background mode during calibration. The black line represents the ratio of signal intensity at 97 m/z and 64 m/z. The blue line represents water vapor concentration. Red dots represent the 3 - minute averaged calibration factors at different steps. The instrument signals were continuously measured by adjusting H_2O concentrations without changing other parameters. The different OH concentrations were calculated according to E 4.7.

E 4.7 $$[HO_2] = [OH] = I \times t \times \sigma_{H_2O} \times \phi_{H_2O} \times [H_2O]$$

For each step, the signal intensities (in Hz) of HSO_4^- and NO_3^- were collected for 6 minutes with 3 minutes each for background mode and signal mode. The calibration factors were determined from the calculated OH concentrations and signal intensities based on E 4.5.

E 4.5 $$[OH] = \frac{1}{C_{OH}} \times \frac{S_{OH}}{S_{64}}$$

The red dots in Figure 4.5.1 represent the average calibration factors for every 6 minutes. The result shows that the calibration factors in different steps were very close, ranging from 1.60 to 1.69 × 10^{-10} Hz cm^3., and were independent of water vapor concentrations. The averaged calibration factor for our CIMS is 1.64 × 10^{-10} Hz cm^3 in this calibration. During this campaign, the calibration factor remained unchanged.

In the last campaign, the calibration factor for OH (C_{OH}), H_2SO_4 (C_{H2SO4}), and HO_2 (C_{HO2}) were determined by the same calibration system. The C_{H2SO4} should be approximate to the C_{OH} due to the measurement principle. The C_{HO2} is determined by E 4.6.

E 4.6 $$[HO_2] = \frac{1}{C_{HO2}} \times \frac{S_{HO2}}{S_{64}}$$

E 4.7 $$[HO_2\,] = [OH] = I \times t \times \sigma_{H_2O} \times \phi_{H_2O} \times [H_2O]$$

Where [HO_2] is calculated from E 4.7 and the S_{HO2} is calculated from the transformed E 4.3 ($S_{HO2} = \frac{S_{97NO} - S_{97NOSca}}{2}$). The C_{HO2} in this campaign were calculated in different [H_2O]. Similar to the C_{OH} result, the C_{HO2} is independent of water vapor concentrations and the averaged C_{HO2} is 0.60 × 10^{-8} Hz cm^3 (figure not shown)

The calibration factors were closely associated with the specifications; hence, the CIMS was calibrated both before and after any modifications. Additionally, the CIMS underwent calibration in varying atmospheric conditions, such as temperature, relative humidity, and light conditions, during each campaign. It is worth noting that the calibration factors remained relatively stable under consistent settings, irrespective of the ambient conditions.

4.6 Detection Limit and Uncertainty

The detection limit can be calculated as follows,

E 4.10 $$DL = \frac{1}{C} \times \frac{n*\sigma}{S_{64}}$$

where DL is the detection limit in 10^6 cm^{-3}, C is the calibration factor, and *n* is the ratio of signal to noise (S/N). σ represents the standard deviation of the signal intensity of HSO_4^- at 97 m/z, and S_{64} represents the signal intensity of NO_3^- at 64 m/z at the integration time t. The σ in detection limit calculations for OH, H_2SO_4, and HO_2 is the standard deviation of $S_{97ScaSO2}$, $S_{NoiseCIMS}$, and $S_{97ScaNO}$, respectively. $S_{97ScaSO2}$, $S_{NoiseCIMS}$, and $S_{97ScaNO}$ are the signals with scavenger gas in the front injectors for different measurements (Figure 4.1.1).

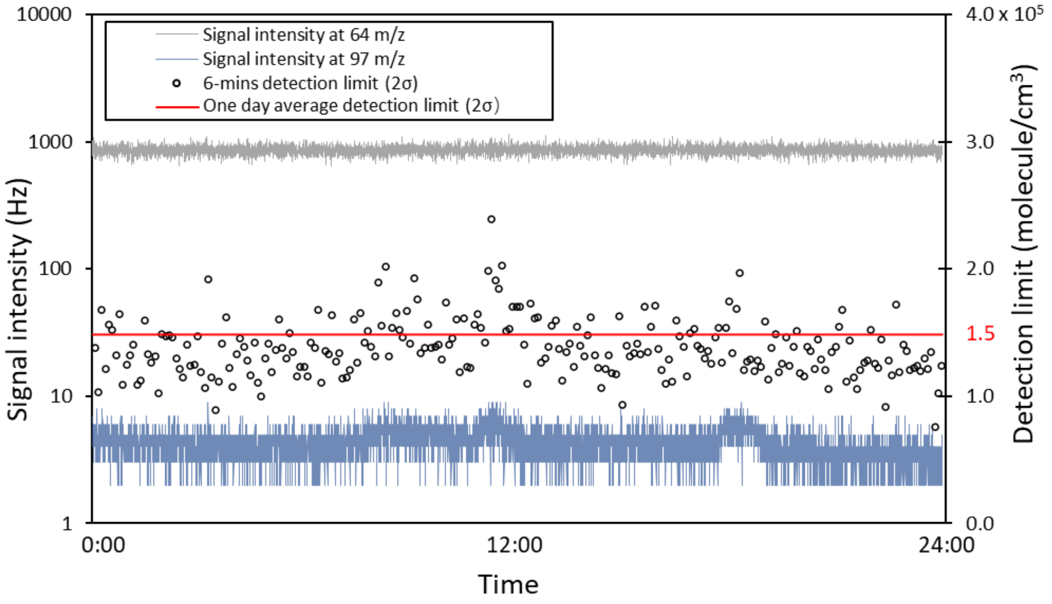

Figure 4.6.1 The detection limit (2σ) of the CIMS. The one-day averaged detection limit is 1.5x10^5 molecule/cm^3 for OH measurement.

Figure 4.6.1 shows the concentrations of OH radicals and the corresponding detection limit (S/N = 2, average time = 6 minutes) in the laboratory as an example. The detection limit was quite stable over the whole day and ranged from 0.08 to 0.20 × 10^6 cm^{-3}, with an average value of approximately 0.15 × 10^6 cm^{-3}. The detection limit of HO_2 was acquired by the same method with the S/N ratio measured with the addition of NO. The average detection limit (S/N = 2, average time = 6 minutes) value of HO_2 is around 2×10^6 cm^{-3}. Unlike the other CIMS in previous research institutes which has a stable DL with the addition of isotopic $^{34}SO_2$ for conversion, the DL of our CIMS for the field campaign varies under ambient conditions and is several times greater than the lab DL.

The uncertainty for the calibration factor (C) of OH measurements is dependent on the uncertainties of all the parameters involved in the calculation of the concentrations of OH radicals and the precision of the measurements of signal at 64 m/z and 97 m/z. The uncertainty was ~36% for It, $\sigma_{\mathrm{H_2O}}$~5% for $\sigma_{\mathrm{H_2O}}$, <1% for $\phi_{\mathrm{H_2O}}$ (Cantrell et al. 1997), and ~10% for the water concentration (Kukui et al., 2008). The precision of the measurement signal at 64 m/z and 97 m/z of the CIMS instrument (2σ) was 11% (for 6 min integration time). The overall uncertainty for the calibration factor was about 38% (2σ) for OH. The uncertainty for H_2SO_4 and HO_2 is calculated similarly, and the uncertainties for the three campaigns are shown in section 5.2.

Besides the uncertainty, the residual gases in the inlets after the switching of measurement targets also need to be considered during the radical measurements. However, the residual problem of SO_2 and NO changed with measurement duration, the inlet cleaning process, and the ambient air conditions. Thus, the residual problems have to be addressed under measurement conditions. See the detailed description of the residual problem and the solution in the next section.

4.7 Residual Problem and Solution

The residual problem did not affect the measurement result when the CIMS measured OH only. However, in the development of H_2SO_4 and HO_2 measurements of our CIMS, the residual of injection gases (NO and SO_2) caused positive bias on OH and H_2SO_4 measurements, respectively.

The ambient H_2SO_4 was measured by switching off the injection of SO_2 gases in the front injector. After switching off of SO_2 injection in front injectors, the SO_2 residual in the injector tubes will be carried to the sample flow by other injection gases, react with ambient OH (R 1.24 to R 1.26), and contribute to the $S_{97w/o}$ signal (Figure 4.1.1). Similarly, when CIMS switched from HO_2 to OH measurement, the NO gases in the front injectors will be switched off. The residual NO in the front injector tubes will be carried to the sample flow and convert HO_2 to OH (R 1.9) and causing an unwanted increase in the S_{97SO2} signal (Figure 4.1.1).

The SO_2 residual problem for H_2SO_4 measurement can be solved due to the measurement of H_2SO_4 does not require any injection in the front injector. By the application of a three-way valve to the CIMS front injectors (The front valve in Figure 4.2.1), the entire front injector flow was switched to the exhaust. In this case, the residual SO_2 in the front injectors tubes does not contact the sample flow, which perfectly avoids the residual SO_2 gases in the front injector during H_2SO_4 measurement.

The NO residual problem, on the other hand, is inevitable because the measurement of OH requires SO_2 injection in the front injectors and such injection will carry the residual NO in the injector tubes to the sample flow after switching off the NO injection. It is hard to estimate the residual problem during ambient measurement by conventional time series analysis. The ambient OH concentration has distinct variations during measurement due to their chemical properties which means it is difficult to determine whether the change of signal is due to the residual problem or the change of ambient conditions. The previous study determined the residual time of NO by the calibration process (Kukui et al., 2012). By monitoring the changes in OH calibration factors before and after NO injection, the residual time of NO can be determined.

Nevertheless, the calibration process is not enough for NO residual time determination. The concentration of OH in calibration is 10 to 100 times larger than in ambient measurement which means the residual NO caused the increase of S_{97} might be lower enough to not affect the OH signal during calibration but still attribute to the

S_{97} during ambient OH measurement. Additionally, the residual problem seems mitigated after the cleaning of the inlets and deteriorated during the continued measurements without cleaning which means the positive bias signal caused by residual NO will also increase during continued measurements.

To better determine the impact of the residual problem and monitor the signal changes due to residual gases during the measurement, we developed a data analysis method that divided the observation results into serval cycles (Cyc #) based on the injection time of NO.

Table 4.1 The cycle and dataset set up for NO residual problem monitoring (Hok Tsui 2021 to 2022 campaign).

Cyc start Time	Cycle #	Set 1 0 min	Set 2 2 min	Set 3 4 min	Set 4 6 min	Set 5 8 min	Set 6 10 min	Set 7 12 min	Set 8 14 min	Set 9 16 min	Set 10 18 min	Set 11 to 20 20 min to the end
0:00	Cyc 1	HO_2	HO_2	HO_2	H_2SO_4	H_2SO_4	OH	OH	OH	H_2SO_4	H_2SO_4	repeat Set 6 to 10 twice
0:40	Cyc 2	HO_2	HO_2	HO_2	H_2SO_4	H_2SO_4	OH	OH	OH	H_2SO_4	H_2SO_4	
……	……	……	……	……	……	……	……	……	……	……	……	
23:20	Cyc 36	HO_2	HO_2	HO_2	H_2SO_4	H_2SO_4	OH	OH	OH	H_2SO_4	H_2SO_4	

Table 4.1 shows the diurnal data rearranged by 36 cycles. Each cycle starts with the injection of NO and the duration of each cycle is 40 mins. In the first 6 mins of each cycle, SO_2 and NO were injected into the sample flow and measured the ambient HO_2 radical (S_{97NO} and $S_{97ScaNO}$). Then in the next 4 mins of each cycle, the front injector flow draws to exhaust by the three-ways valve for H_2SO_4 measurement ($S_{97w/o}$). After that, in the next 6 mins (Set 6 to 8 in Cyc1) of each cycle, the front injectors switch back and the SO_2 is injected again for OH measurement (S_{97SO2} and $S_{97ScaSO2}$) without NO addition. The measurement of OH and H_2SO_4 will continue to switch two more times (Table 4.1) to finish one cycle measurement. After the diurnal measurement was finished, 36 cycles were collected.

The data sets (Set #) in Table 4.1 are the union of 2 mins results with respect to their start time in each cycle. For example, set 1 is the collection of 2 mins HO_2 measurement from each cycle (Cyc1 to Cyc36), and Set 8 is the collection of 2 mins

OH measurement from each cycle (Cyc1 to Cyc36) which starts 4 mins after the stop of NO injection. As the increase of the Set #, the measurement starts later after the NO injection is switched off. By comparing the diurnal pattern and averaged concentration in different sets of OH, the residual NO will be monitored.

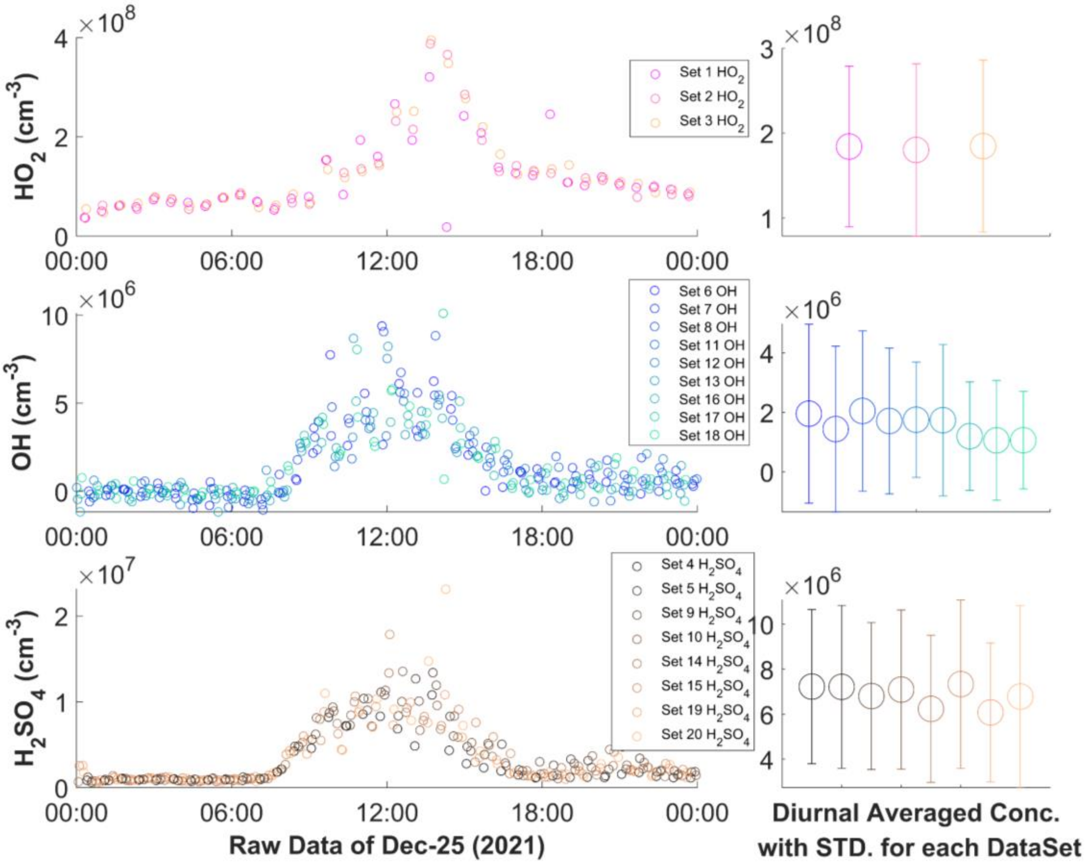

Figure 4.7.1 Measurement result of OH and H_2SO_4 at Hok Tsui, 25 December 2021.

Figure 4.7.1 shows the 2 mins averaged diurnal result for the CIMS measurement in the field study after cleaning the CIMS's injectors and inlet (See section 6.3 for detailed results of the field study). The data sets were labeled in different colors. The diurnal averaged concentration with standard deviation for each dataset is shown on the right. Three sets of HO_2 shows similar diurnal patterns and the daytime averaged concentration (1.84 ± 0.95, 1.80 ± 1.02, and $1.84\pm1.01\times10^8$ cm^{-3} for set 1, 2, and 3, respectively). The results in the different datasets didn't show any significant difference (p>0.05). Similarly, H_2SO_4 and OH results show no significant difference (p>0.05) between the data sets with maximum ($7.33 \pm 3.74 \times 10^6$ cm^{-3}, Set 6, for H_2SO_4 and $2.04 \pm 2.68 \times 10^6$ cm^{-3}, Set 3, for OH) and minimum averaged concentration ($1.06 \pm 1.63 \times 10^6$ cm^{-3}, Set 18, for OH and $6.07 \pm 3.09 \times 10^6$ cm^{-3}, Set 19, for H_2SO_4), respectively.

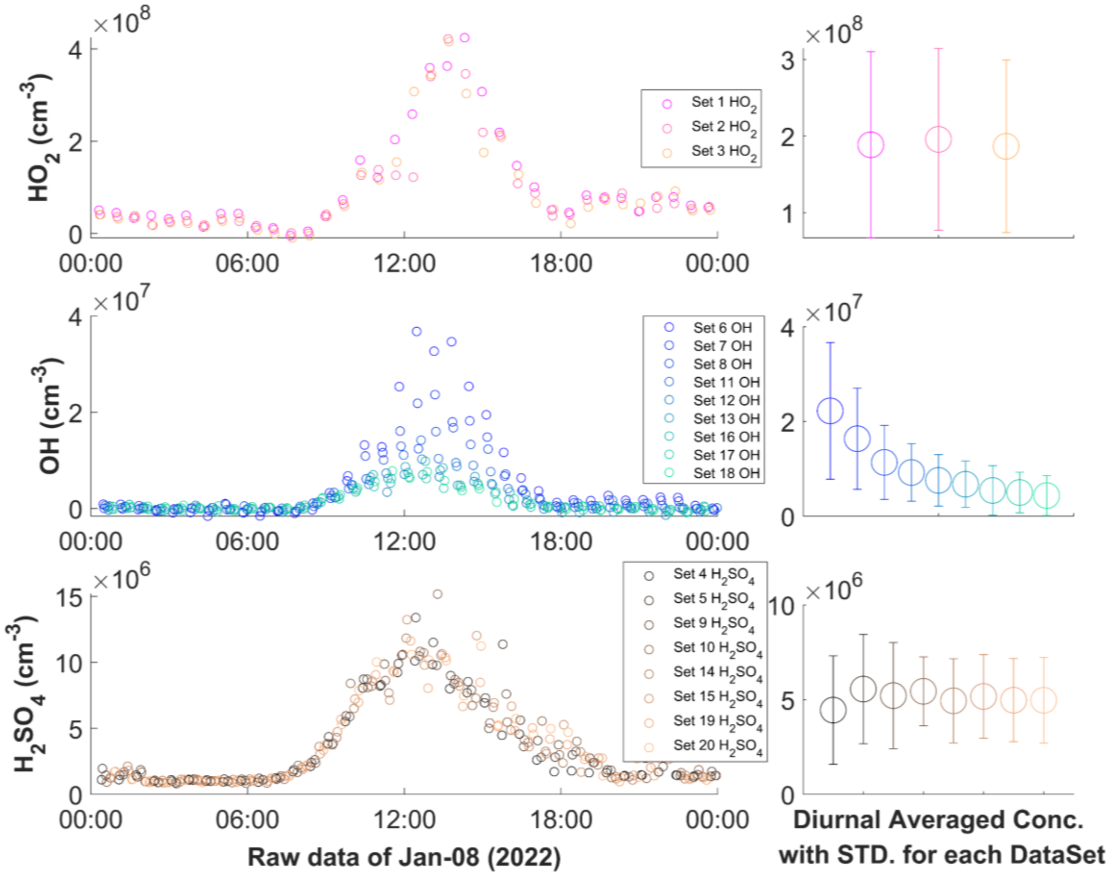

Figure 4.7.2 Measurement result of OH and H_2SO_4 at Hok Tsui on 08 January 2022.

Figure 4.7.2 shows the measurement results after about one week of measurement without cleaning the inlet and injectors. The averaged HO_2 and H_2SO_4 concentration for different data sets on the same day didn't show a significant difference (p>0.05) which demonstrates that the CIMS was properly functioning for HO_2 and H_2SO_4 measurement.

However, the OH measurement results show an obvious decrease as the increase of the number of data sets in raw data and the data set averaged concentration (Figure

4.7.2). The first data set of OH measurement (Set 6) has an average concentration of $2.22 \pm 1.44 \times 10^{7}$ cm^{-3} and the average concentration in the last OH data set (Set 18) is $4.34 \pm 4.21 \times 10^{6}$ cm^{-3} which is significantly different. This implies that the residual NO caused an increase in OH corresponded signal on 08 January (Figure 4.7.2) is more obvious and the residual time of NO is longer compared to the first day after cleaning (Figure 4.7.1). Nevertheless, the last two sets of OH didn't show a significant difference statistically ($p > 0.05$) which implied that the residual NO can be eliminated within the cycle duration. When the last two datasets of OH show significant differences, the inlets, and injectors of the CIMS need to be cleaned to eliminate the residual NO for valid OH measurement.

5. Methodology for Field Study

5.1 Field Setup

5.1.1 The Hong Kong Polytechnic University

Figure 5.1.1 The map of ambient experiment location from Google Earth (© Google Earth).

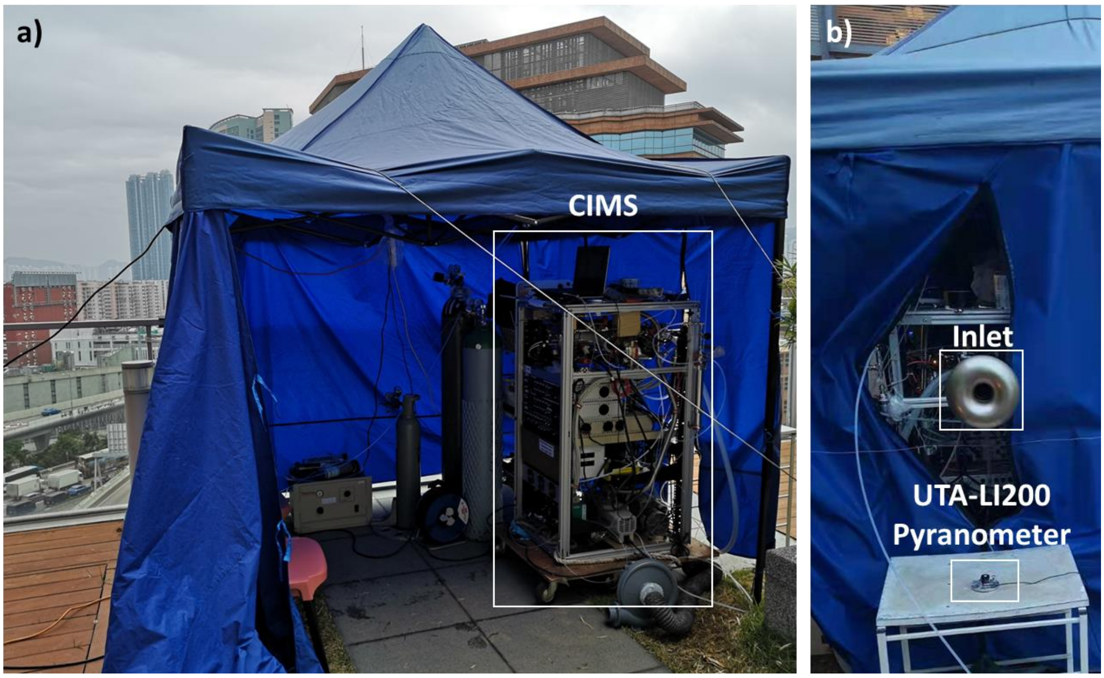

Figure 5.1.2 The setup of CIMS in the sky garden in PolyU. a) the rain tent in the sky garden and b) the front side of the tent for CIMS sampling.

Figure 5.1.1 shows the first campaign for testing the OH CIMS. The location is labeled with a red dot in Figure 5.1.1 which is around 50 m high above the ground on the 11th floor of a teaching building on the campus of The Hong Kong Polytechnic University (PolyU) and was surrounded by several busy roads. A tent was set up as a temporary shelter for the CIMS (Figure 5.1.2). The sample inlet was positioned horizontally facing the south. Since the tents could only provide protection from fine rain and without temperature control, other species like NO_x were not included and only OH concentration and solar radiation were measured to check the function of CIMS after the sensitivity tests.

5.1.2 The Hok Tsui Supersite

Figure 5.1.3 Location of Hok Tsui Supersite Air Monitoring Station on China's southern coast, in Hong Kong.

Two more field campaigns were conducted at the Cape D'Aguilar (or Hok Tsui (HT)) Air Quality Supersite operated by the Hong Kong Environmental Protection Department from October 6 to November 24, 2020 (HT 2020), and November 06, 2021, to January 15, 2022 (HT 2021-22). The HT Supersite (22°12'32" N, 114°15'12" E) is a coastal site located at the south-eastern tip of Hong Kong Island. The site is surrounded by the ocean, vegetation, and sparse country roads (Figure 5.1.3) and is ~15 km away from the nearest urban center. There is no strong anthropogenic emission source within the surrounding area, except for the ocean-going vessels traveling in nearby waters (Peng et al., 2022). Nonetheless, the site occasionally receives polluted air masses from mainland China, including the highly urbanized Pearl River Delta (PRD) region (Li et al., 2018; Peng et al., 2022).

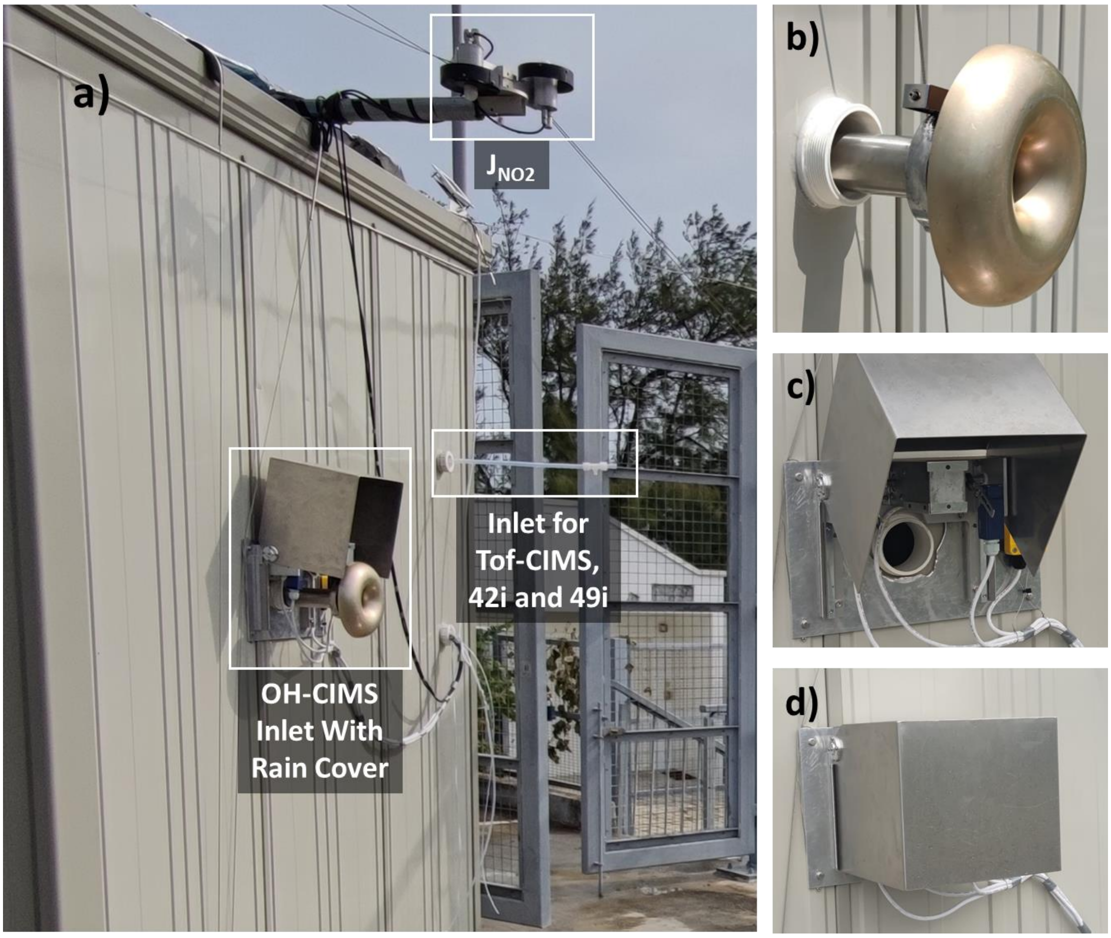

Figure 5.1.4 a) The measurement setup in yard B of Hok Tsui Supersite. b) the sample inlet of CIMS without the rain cover. The rain cover without sample inlet under c) sunny and d) rainy conditions, respectively.

For the HT 2020 campaign, we measured OH radicals, O_3, NOx, CO, HONO, VOC, OVOCs, relative humidity, temperature, NO_2 photolysis frequency (J_{NO2}), and aerosol size distribution. Table 5.1 summarized their measurement technique, resolution, and detection limits. As shown in Figure 5.1.4, The OH-CIMS was housed in an air-conditioned shelter in yard B together with Tof-CIMS, Ozone, and NO_x analyzers. The stainless-steel inlet with scoop stretched out from the hole of the shelter's wall and horizontally facing the south for sampling (Figure 5.1.4b). The self-designed automatic rain cover was applied to protect the sample inlet from rain (Figure 5.1.4c and d). The J_{NO2} was measured on top of the shelter. The other gases and aerosol size distribution were measured inside the main station building in yard A around 10 m away from yard B (Figure 5.1.3). Table 5.1 summarizes the instruments and measured species during the HT 2020 campaign. The backward trajectory was calculated at 1-hour intervals for sampling days at an elevation of 60 m above ground level using MeteoInfoMap software on meteothink.org, (Wang, 2014, 2019).

For the HT 2021-22 campaign, the sampling conditions and sets up were the same as that in HT 2020. Only the OH, HO_2, and H_2SO_4 results obtained in 2021 will be shown in the results section to demonstrate the capability of HO_x-CIMS.

Table 5.1 Instruments and measured species in the HT 2020 field campaign.

Species	Instruments	Time Resolution	Detection Limit	Accuracy (1σ)
NO, NO_2	Chemiluminescence/photolytic converter (Thermo, Model 42i)	1 min	60 ppt	NO: ± 5.2% NO_2: ± 15.2%
OH	Nitrate-quadrupole chemical ionization mass spectrometer (CIMS)	10 s	Lab: 1.7×10^5 cm^{-3} Daytime: 1.2×10^6 cm^{-3}	± 44%
Ozone	Ozone analyzer, model 49i, Thermo Scientific	1 min	0.5 ppb	± 6.0%
JNO_2	Filter Radiometer, Metcon	1 min	4×10^{-5} s^{-1}	± 10%
HONO	Iodide-Tof-CIMS, Aerodyne Inc	1s	0.2 ppt	± 15 %
SO_2	Pulsed Fluorescence SO_2 Analyzer (Thermo, Model 43i)	1 min	1 ppb	± 6.1%
CO	Gas Filter Correlation CO Analyzer (Thermo, Model 48i)	1 min	40 ppb	± 7.4%
NH_3	Chemiluminescence NH_3 Analyzer (Thermo, Model 17i)	2 mins	1 ppb	± 8%
Particle number size distribution	Scanning mobility particle sizer, TSI	5 mins	1 particle cm^{-3}	± 10%
VOCs	GC-MS/FID (GC955 Series 611/811, Syntech Spectras)	1 hour	~10 ppt	± 20%
	PTR-MS (PTR-QMS 500, IONICON Analytik, Austria)	5 mins	20 ppt	± 20%
OVOCs	PTR-Tof-MS, IONICON Analytic;	1 s	~10 ppt	± 15%

5.2 CIMS Configuration in Different Field Studies

The CIMS for the first and second field campaigns measured OH only. These two campaigns were done in April 2019 at PolyU and in Autumn 2020 at Hok Tsui, respectively. As shown in Table 5.2, the scavenger gases changed from propane to C_3F_6. Since the only first cylinder of propane had a satisfying purity for OH elimination, C_3F_6 was applied in the second campaign. Besides that, the reagent ion also changed from NO_3^- to $N^{18}O_3^-$ to mitigate the reagent signal decrease due to detector aging. With the rain cover applied in the second campaign, the nighttime signal was available for the calculation of the detection limit. Therefore, the elimination rates, calibration factors, and detection limits changed between the first and second campaigns.

The CIMS in the last campaign in Winter 2021 to 2022 at Hok Tsui could measure OH, HO_2, and H_2SO_4 with the addition of NO and the front valve. Their detection limits, calibration factors, and uncertainties are shown in Table 5.2. Compared to the previous campaigns, settings changed as follows:

1. 2 sccm of NO was added to the sample flow for HO_2 conversion in the third campaign.
2. The SO_2 flow was increased from 5 to 10 sccm to achieve the optimized $[SO_2]/[NO]$ for HO_2 conversion as mentioned in section 4.4.3.4.
3. The elimination rate was relatively low compared to the previous campaigns due to the increase of SO_2 and the extra measurement of HO_2. This can be improved by increasing the scavenger gas concentration. However, in this study, the sensitivity was good enough for measurement even with a lower elimination rate, the flows of scavenger gases remain the same in three campaigns for better comparison.

Table 5.2 Specifications of CIMS for HO_x and H_2SO_4 measurements in three campaigns. The red color shows changes in CIMS's settings.

PolyU 2019

Efficiency Related	Parameters	Gas	Values	Units	Specification for Measurement	Values	Units
E_{Conv}	**Front Injection**	SO_2 (0.9%)	5	sccm	Sample Flow [SO_2]	12	ppm
	Pulse Valve	N_2	2	sccm	Cycle Duration (OH)	6	mins
		C_3H_8 (99.9%)	2	sccm	Scavenging Efficiency (OH)	98%	
	Rear Injection	C_3H_8 (99.9%)	2	sccm	Sample Flow [C_3H_8]	1072	ppm
		HNO_3	10	sccm	Reaction Time	47	ms
	Sample Flow		3.7	slpm	Sample Flow Speed	55	cm/s
E_{Ion}	**Sheath Flow**	Zero Air	12.6	slpm	Reynolds Number in Ionization Chamber	>4000 Turbulent flows	
		HNO_3	10	sccm			
		C_3H_8 (99.9%)	2	sccm	Sheath Flow [C_3H_8]	159	ppm
	Total Flow		16.8	slpm	Sheath Flow Speed	25	cm/s
	Sheath Voltages		-80	V	Voltages Difference for ionization	48	V
	Sample Voltages		-32	V			
E_{Trans}	**Buffer Gas**	N_2	440	sccm	Voltages Difference for transmission	80	V
	Buffer Voltages		-70	V			
	Pinhole Voltages		-40	V			
Cal	**Calibration Flow**		10	slpm	Calibration Factor (Reagent ion: NO_3^-)	$1.64*10^{-10}$	cm^3
	Flow Speed		65	cm/s			
	Product It Value		$1.46*10^{11}$	photon/cm^2			
Uncertainties	**Sigma**			2	**Detection Limit ($\times 10^5$ cm^{-3}) (3σ)**	In lab	1.5
	Calibration			38%		Day	9
	Overall			51%		Night	N/A

Hok Tsui 2020

Efficiency Related	Parameters	Gas	Values	Units	Specification for Measurement	Values	Units
E_{Conv}	**Front Injection**	SO_2 (0.9%)	5	sccm	Sample Flow [SO_2]	12	ppm
	Pulse Valve	N_2	2	sccm	Cycle Duration (OH)	6	mins
		C_3F_6 (99.9%)	2	sccm	Scavenging Efficiency (OH)	92%	
	Rear Injection	C_3F_6 (99.9%)	2	sccm	Sample Flow [C_3F_6]	1072	ppm
		HNO_3	10	sccm	Reaction Time	47	ms
	Sample Flow		3.7	slpm	Sample Flow Speed	55	cm/s
E_{Ion}	**Sheath Flow**	Zero Air	12.6	slpm	Reynolds Number in Ionization Chamber	>4000 Turbulent flows	
		HNO_3	10	sccm			
		C_3F_6 (99.9%)	2	sccm	Sheath Flow [C_3F_6]	159	ppm
	Total Flow		16.8	slpm	Sheath Flow Speed	25	cm/s
	Sheath Voltages		-80	V	Voltages Difference for ionization	48	V
	Sample Voltages		-32	V			
E_{Trans}	**Buffer Gas**	N_2	440	sccm	Voltages Difference for transmission	80	V
	Buffer Voltages		-70	V			
	Pinhole Voltages		-40	V			
Cal	**Calibration Flow**		10	slpm	Calibration Factor (Reagent ion: $N^{18}O_3^-$)	$1.21*10^{-8}$	cm^3
	Flow Speed		65	cm/s			
	Product It Value		$8.8*10^{10}$	photon/cm^2			
Uncertainties	**Sigma**			2	**Detection Limit ($\times 10^5$ cm^{-3}) (3σ)**	In lab	1.7
	Calibration			38%		Day	12
	Overall			44%		Night	8.5

Hok Tsui 2021-2022

Efficiency Related	Parameters	Gas	Values	Units	Specification for Measurement	Values	Units
E_{conv}	**Front Injection**	SO_2 (0.9%)	10	sccm	Sample Flow [SO_2]	24	ppm
		NO (0.9%)	2		Sample Flow [NO]	5	ppm
	Pulse Valve	N_2	2	sccm	Cycle Duration (OH)	6	mins
					Cycle Duration (HO_2)	60	mins
		C_3F_6 (99.9%)	2	sccm	Scavenging Efficiency (OH)	90%	
					Scavenging Efficiency (HO_2)	60%	
	Rear Injection	C_3F_6 (99.9%)	2	sccm	Sample Flow [C_3F_6]	1072	ppm
		HNO_3	10	sccm	Reaction Time	47	ms
	Sample Flow		3.7	slpm	Sample Flow Speed	55	cm/s
E_{Ion}	**Sheath Flow**	Zero Air	12.6	slpm	Reynolds Number in Ionization Chamber	>4000 Turbulent flows	
		HNO_3	10	sccm			
		C_3F_6 (99.9%)	2	sccm	Sheath Flow [C_3F_6]	159	ppm
	Total Flow		16.8	slpm	Sheath Flow Speed	25	cm/s
	Sheath Voltages		-80	V	Voltages Difference for ionization	48	V
	Sample Voltages		-32	V			
E_{Trans}	**Buffer Gas**	N_2	440	sccm	Voltages Difference for transmission	80	V
	Buffer Voltages		-70	V			
	Pinhole Voltages		-40	V			
Cal	**Calibration Flow**		10	slpm	Calibration Factors ($N^{18}O_3^-$) OH	$1.09*10^{-8}$	cm^3
	Flow Speed		65	cm/s	H_2SO_4	$1.07*10^{-8}$	
	Product It Value		$8.8*10^{10}$	photon/cm^2	HO_2	$6.01*10^{-9}$	
Overall Uncertainties (2σ)		OH		46%	**Detection Limit in Field Study ($\times 10^6$ cm^{-3}) (3σ)**	OH	3
		H_2SO_4		40%		H_2SO_4	1
		HO_2		44%		HO_2	20

5.3 Box Modeling for Hok Tsui 2020 Campaign

The Framework for 0-D Atmospheric Modelling (F0AM) using the Master Chemical Mechanism (MCM) v3.3.1 (Wolfe et al., 2016) was used to simulate OH concentrations. MCM v3.3.1 (http://mcm.leeds.ac.uk/MCM) is a near-explicit chemical mechanism that includes over 17,000 elementary reactions of 6700 primary, secondary, and radical species (Jenkin et al., 2015). The isoprene degradation mechanisms, and in particular the mechanisms OH regenerated by HO_x recycling in low NO_x condition, were improved in MCM v3.3.1. The MCM mechanism has been used in previous studies to investigate OH chemistry in different environments, including forests (Stone et al., 2011), urban areas (Slater et al., 2020), suburban areas (Tan et al., 2018), and coastal regions (Sommariva et al., 2004). In our study, observational data (shown in Table 1) were used to constrain the model. These data included VOCs, OVOCs, SO_2, NO_x, CO, O_3, HONO, photolysis frequency of NO_2 (J_{NO2}), and meteorological parameters (temperature, relative humidity, and pressure). The photolysis frequencies for other species were calculated by the "HYBRID" method in F0AM which is based on Tropospheric Ultraviolet and Visible (TUV v5.2) Radiation Model from National Center for Atmospheric Research. The Ozone column we used for TUV calculation was 240 DU (the Dobson unit) which is the average number from October to November 2020 for the Hok Tsui area according to the worldview website (EOSDIS Worldview (nasa.gov)). The simulated photolysis frequencies were then scaled by the correction factor obtained from the comparison between observed and modelled J_{NO2}. The first-order physical loss process, with a 24-hour lifetime for all species, was included in the model to represent physical processes (Wolfe et al., 2016; Chen et al., 2022b). The physical loss process has a negligible influence on OH simulation because the OH concentrations are controlled by fast *in situ* chemistry.

The heterogeneous uptake of HO_2 by aerosols was included in the model by assuming a pseudo-first-order loss of HO_2 (E5.1–E5.2; Jacob, 2000):

E 5.1 $$\frac{d[HO_2]}{dt} = -k_{HO_2}[HO_2]$$

E 5.2 $$k_{HO_2} = \frac{V_{HO_2} \times S_a \times \gamma_{HO_2}}{4}$$

E 5.3 $$V_{HO_2} = \sqrt{\frac{8RT}{\pi \times MW_{HO_2}}}$$

where k_{HO_2} is the first-order loss rate coefficient of HO_2 by aerosol uptake, γ_{HO2} is the effective HO_2 uptake coefficient (0.1 for the base model run; Guo et al., 2019), v_{HO_2} is the mean molecular velocity of HO_2, S_a is the aerosol surface area concentration measured by a scanning mobility particle sizing (SMPS), and M_{HO_2} (= 17 g/mol) is the molecular mass of HO_2. We assumed in the model that the products of heterogeneous HO_2 loss would not participate in further reactions (Guo et al., 2019). On the other hand, as mentioned in the introduction, the uptake of the OH radical is negligible and does not change the troposphere OH concentration as shown in the previous study (Ivanov et al., 1996; Park et al., 2008).

The observation data were averaged every 10 mins for the model input. Any missing values were calculated assuming linear interpolation. The measured concentrations of NO and NO_2 were used to constrain the model. Due to the clean condition of the coastal air, some of the reactive alkenes and long-chain alkanes were below detection limits. For the simulation of those compounds, we used concentrations that were half of the detection limits. The measured VOCs were further divided into those of anthropogenic origin (AVOCs) and biogenic origin (BVOCs). The AVOCs included alkanes (C_2–C_8), alkenes (C_2–C_6) benzene, and TEXs (toluene, ethylbenzene, and xylenes), which covered the dominant species originating from petroleum gas and industrial solvent evaporation (Tang et al., 2008), while the BVOCs included isoprene, terpene, pinene, and limonene. The majority (> 95%) of the measured OVOCs in this study were C_1–C_3 aldehydes, ketones, and acids. For each run, a three-day spin-up was performed with constant photolysis and deposition to create a stable model environment and to avoid the uncertainty of unconstrained species (Carslaw et al., 1999).

6. Results of Field Measurement

6.1 PolyU OH Measurement (2019)

After the sensitivity tests and optimization of the instrument in the laboratory, the CIMS was tested in the sky garden for ambient measurement. In this section, we show one of the first successful measurement results of the CIMS.

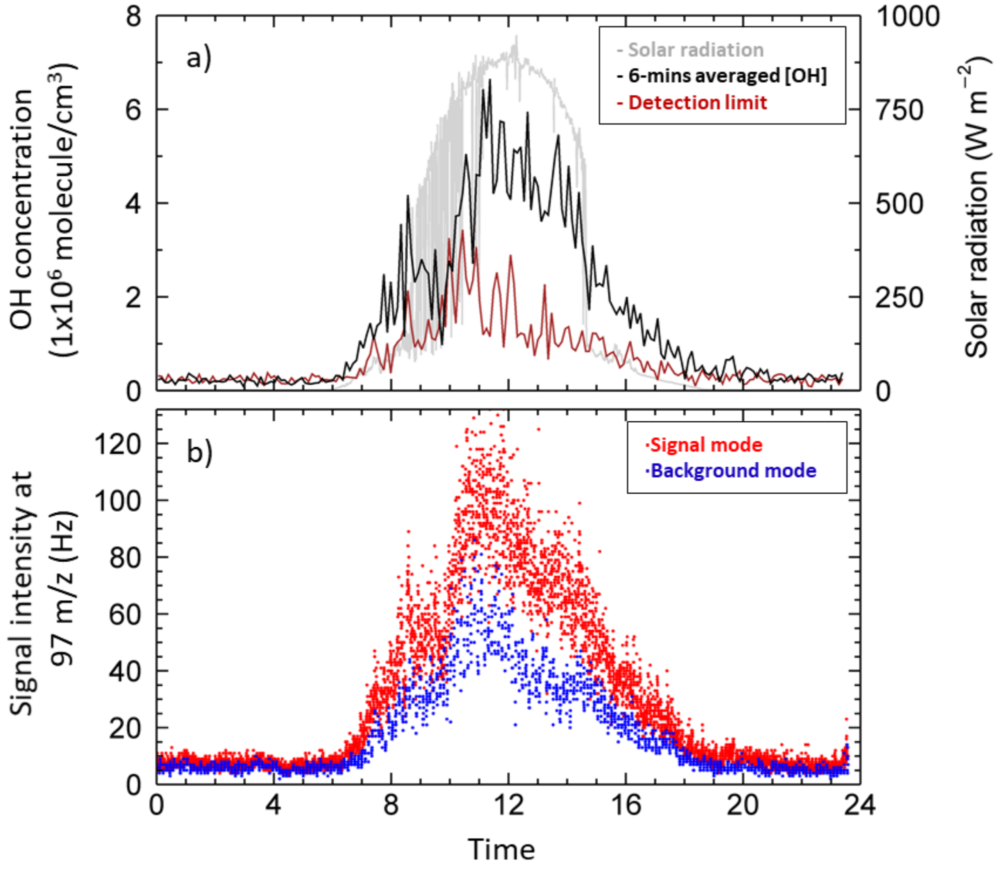

Figure 6.1.1 a) Diurnal variation of OH concentration and solar radiation on the 11th floor of a teaching building on the campus of the Hong Kong Polytechnic University on April 25, 2019. b) The signal intensity at 97 m/z for two different measurement modes: Signal mode also known as S_{97SO2} and Background mode known as $S_{97ScaSO2}$.

Measurements were made with a time resolution of 10 seconds. A typical measurement sequence consisted of 3 minutes in the background mode ($S_{97ScaSO2}$) and 3 minutes in the signal mode (S_{97SO2}). The other details in the settings of the CIMS are shown in Table 5.2.

Figure 6.1.1a shows the diurnal profile of OH concentrations (3-minute average) observed on April 25, 2019, and the solar radiation measured using UTA-LI200 at a time resolution of 1 minute. Figure 6.1.1b shows the measured signal intensities at 97 m/z at the signal mode and the background mode. The OH concentrations exhibited a clear diurnal profile with the highest value of 6×10^6 cm^{-3} at midday and the lowest level of 0.25×10^6 cm^{-3} at night. The OH concentrations were highly correlated to solar radiation, which was similar to previous studies (Rohrer and Berresheim, 2006; Tan et al., 2017). The 3-minute average OH concentrations were above the detection limits ($0.5\text{-}2 \times 10^6$ cm^{-3}) most of the daytime, except during a cloudy period (08:00 to 10:00) (Figure 6.1.1a). This preliminary result demonstrated the capability of our CIMS for measuring ambient OH on a clear day in an urban environment.

6.2 Hok Tsui OH Measurement (2020)

After the testing of CIMS in the sky garden of PolyU, the CIMS participated in a 2-month field study in the supersite held by EPD in Hok Tsui to study the atmospheric oxidation capacity on the south China coast. The specification of CIMS for this campaign is shown in Table 5.2.

6.2.1 Observation Result

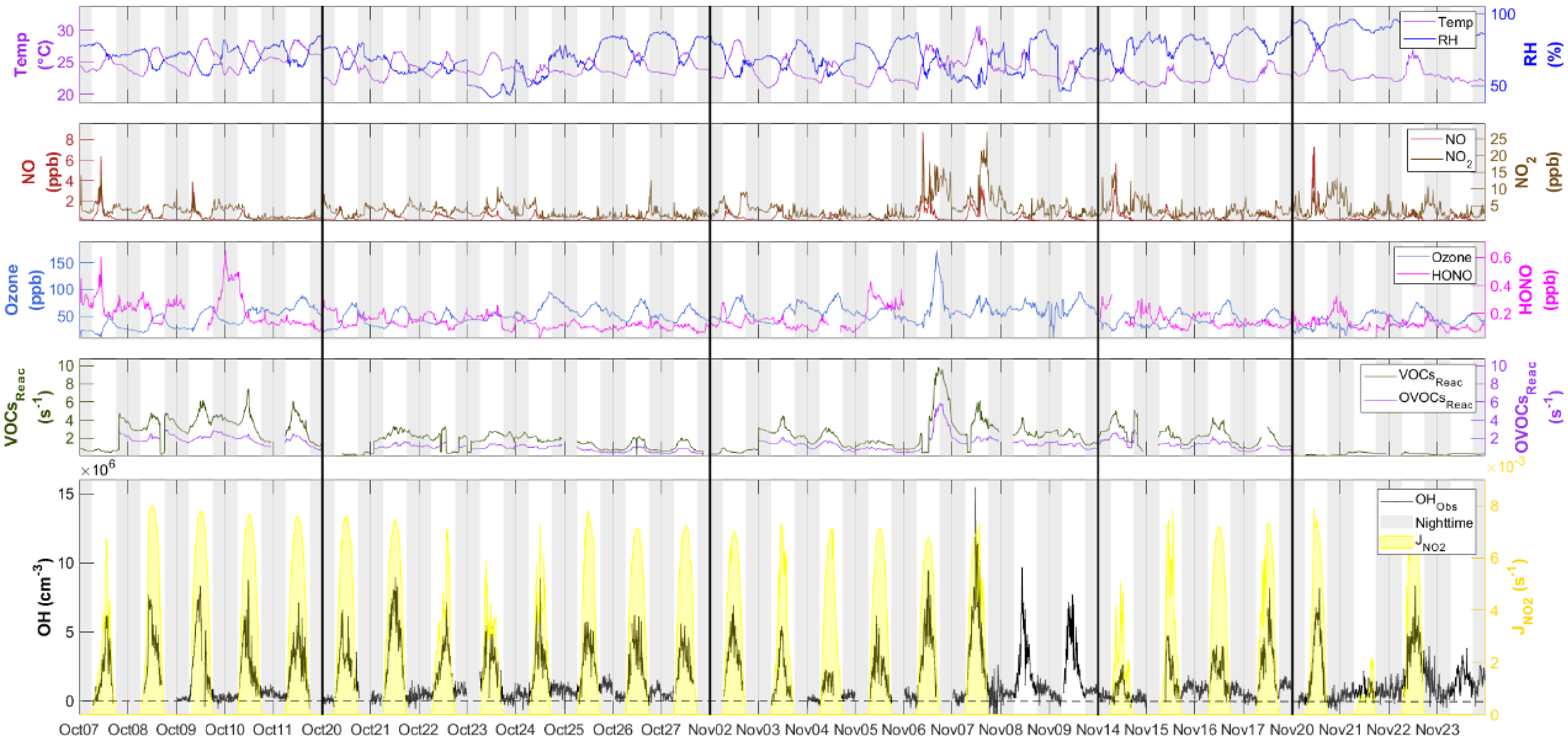

Figure 6.2.1 Time series of OH between 7 October and 23 November with measured weather conditions (temperature and RH), OH primary sources (ozone and HONO), NO_x (NO and NO_2), the reactivity of measured VOCs and OVOCs ($VOCs_{Reac}$, and $OVOCs_{Reac}$), and photolysis frequency (J_{NO2}). All measurement data shown are 10 min averages. The gaps in the data were due to the calibration or instrument maintenance. The black lines separate the non-continuous days during measurement and the black horizontal dotted line denotes [OH]=0. The grey shaded area denotes night-time. The time zone was the local time (+8 UTC) for the x-axis.

Figure 6.2.1 shows the time series of observed OH concentrations, along with the concentrations of other trace gases and the meteorological parameters, during the study period. The weather conditions featured relatively high temperatures, high relative humidity (RH), and strong solar radiation, similar to previous autumn observations at the same site (Li et al., 2018; Peng et al., 2022). The air temperature ranged from 20°C to 30°C and RH ranged from 40% to 96%. The photolysis frequency of NO_2 (J_{NO2}) peaked at 8×10^{-3} s^{-1} around noon on sunny days and decreased to 2×10^{-3} s^{-1} on cloudy days. The observed OH concentrations were mostly above the detection limit during the daytime but closer to the detection limit at night. The OH concentrations showed a distinct diurnal pattern and a positive correlation with J_{NO2} ($R^2 = 0.68$) and calculated J_{O1D} ($R^2=0.46$)(Figure 6.2.2), similar to the findings in previous studies (Berresheim et al., 2003; Rohrer and Berresheim, 2006; Ma et al., 2019). The daily maximum OH concentration varied from 2.1×10^6 cm^{-3} on 21 November, accompanying the lowest level of solar radiation, to 15.4×10^6 cm^{-3} on 7 November during a pollution episode. The pollution episode began on the evening of 6 November and featured a maximum concentration of 174.0 ppb O_3, 8.7 ppb NO, 22.7 ppb NO_2, 9.8 s^{-1} total reactivity of measured VOCs, and 5.8 s^{-1} total reactivity of measured OVOCs. The OH concentration peaked the next day (7 Nov). This suggests abundant OH sources and fast radical propagation under high-NO_x and high-VOC conditions.

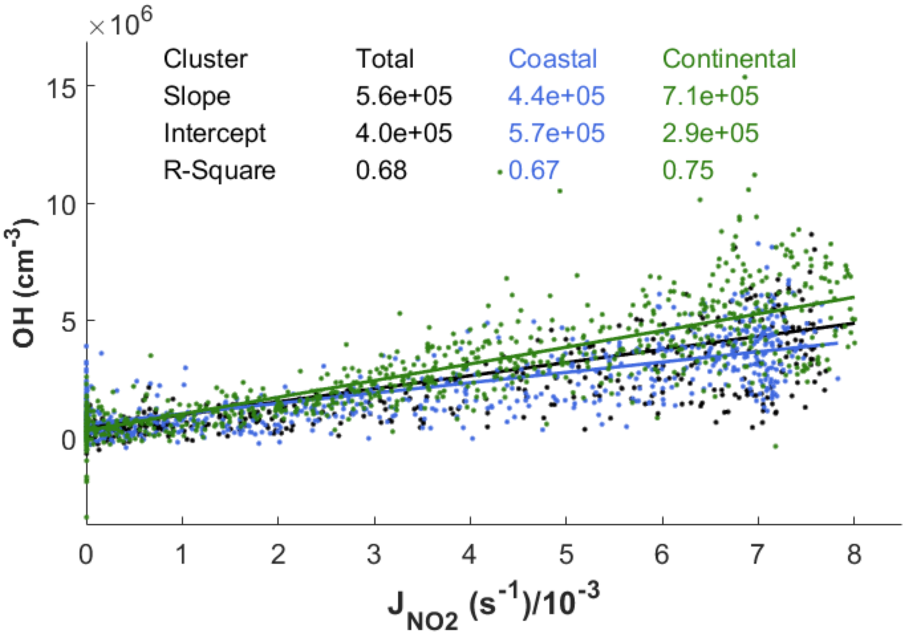

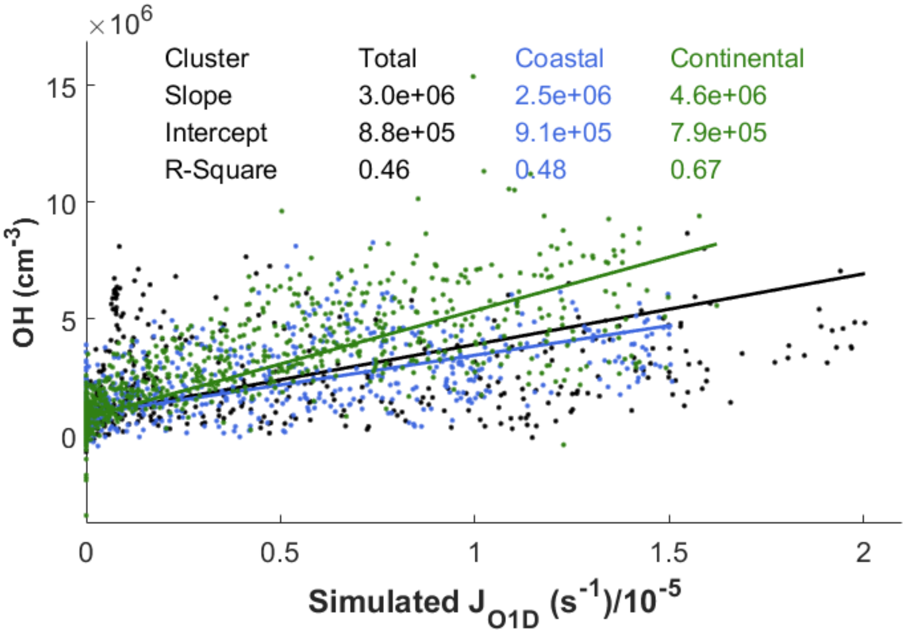

Figure 6.2.2 Correlation between observed OH concentration and a) photolysis frequency of NO_2 (J_{NO2}), and b) model simulated photolysis frequency O_3 (Simulated J_{O1D}). The linear regressions with respect to total, coastal, and continental cases are labeled in black, blue, and green. Note that the coastal and continental cases are reported as correlations for all cases in different clusters, not only the selected cases in the Figures 6 and 8 comparisons.

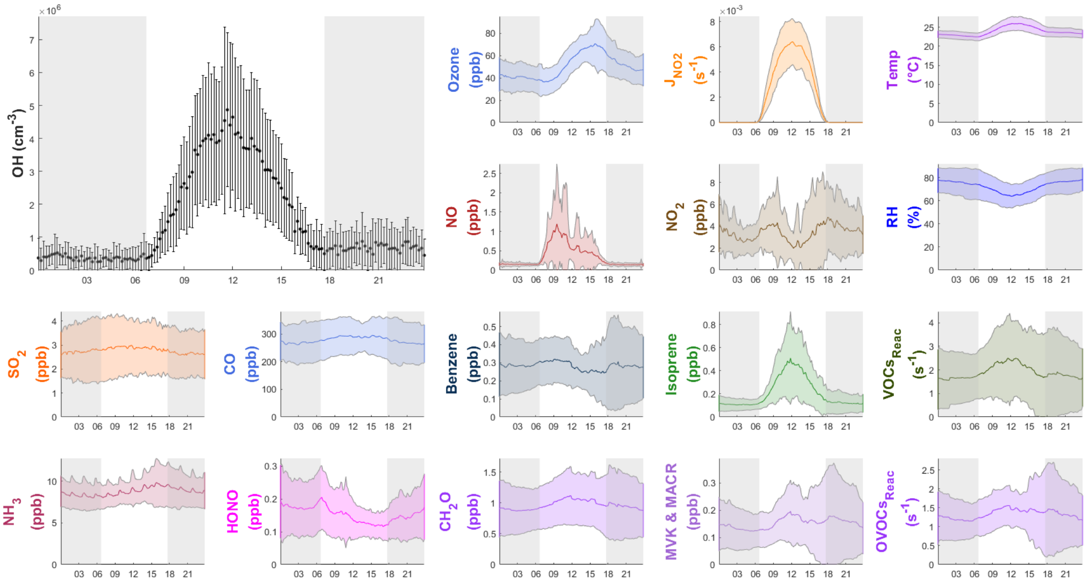

Figure 6.2.3 Diurnal profiles of the average (±1σ) concentrations of OH, other chemical species, the measured VOCs reactivity and OVOCs reactivity ($VOCs_{Reac}$ and $OVOCs_{Reac}$), and meteorological parameters (T, RH, J_{NO2}) during the field campaign. The grey shaded area denotes night-time. The error bars and shaded error bars are the standard deviations of the averaged data.

Figure 6.2.3 shows the average diurnal profiles of OH and other representative species. On average, the maximum OH concentration was $4.9 \pm 2.1 \times 10^6$ (1σ) cm^{-3}. As shown in Table 2.2, the OH concentrations at our site were comparable to those reported in previous field studies conducted at tropical coastal sites. For example, the reported OH maximum concentration was 4.5×10^6 cm^{-3} in the low-altitude remote tropical troposphere (Brune et al., 2020). In a study conducted in autumn at a suburban site in Shenzhen, approximately 50 km away from our site, an OH diurnal maximum concentration of 5.3×10^6 cm^{-3} was observed (Wang et al., 2021b). The average night-time OH concentrations in this study were $5.1 \pm 1.8 \times 10^5$ (1σ) cm^{-3} which was comparable to the previous night-time results (below 10×10^5 cm^{-3}) measured at the PRD region (in Heshan, Tan et al., 2019, and in PKUSZ site, Yang et al., 2022). The OH concentration was slightly higher in the evening ($6.8 \pm 1.1 \times 10^5$ cm^{-3}) than in the morning ($3.7 \pm 0.7 \times 10^5$ cm^{-3}), which might be due to the higher ozone concentration in the evening leading to a higher OH production from alkene ozonolysis.

Figure 6.2.3 also shows the average diurnal patterns of the other trace gases measured. As a primary source of OH, HONO peaked in the morning at 0.21 ± 0.09 ppb around 7:00 local time (LT), and O_3 peaked in the afternoon at 70 ± 20 ppb at around 16:00 LT. The average NO and NO_2 concentrations reached a maximum of 1.2 ± 1.6 ppb at around 10:00 LT and 4.9 ± 3.2 ppb at around 18:00 LT, respectively. Isoprene showed a diurnal pattern similar to that of J_{NO2} and OH, peaking at 0.5 ± 0.4 ppb at noon. Non-negligible levels of NO (~ 0.1 ppb) and isoprene (~ 0.1 ppb) were observed at night, which could be caused by nearby ship emissions and plant emissions, respectively. The average concentrations of all the measured species during the campaign are shown in Table 6.1.

Table 6.1 The average concentration of MCM box model input with respect to different cases.

Species Abb.	Species Name	Total	Coastal	Continental	Oct10M	Oct10A	Episode
OH 10^{6} (cm^{-3})	Hydroxyl radical	2.4±1.9	2.5±1.4	3.1±1.7	3.7±2.1	1.8±1.5	4.2±2.8
OH_DL 10^{6} (cm^{-3})	The detection limit of hydroxyl radical	1.0±0.5	0.8±0.3	0.9±0.3	1.2±0.5	1.5±0.7	1.0±0.5
OH_Err 10^{6} (cm^{-3})	OH Measurement Uncertainty	1.5±1.0	1.8±0.5	1.7±0.6	0.9±0.8	1.0±0.9	2.5±1.7
PM_Num 10^{3} (#/cm^{3})	Number of particulate matters	3.8±1.9	4.1±1.7	4.9±1.4	NaN	NaN	5.6±2.0
*PM_Sur 10^{7} (nm^{2}/cm^{3})	The surface of particulate matters	19.7±9.0	15.0±2.3	26.8±4.3	NaN	NaN	31.5±14.2
PM_Vol 10^{9} (nm^{3}/cm^{3})	The volume of particulate matters	7.6±3.8	4.9±0.7	10.5±1.5	NaN	NaN	12.0±5.9
*RH (%)	Relative humidity	70.1±10.1	69.9±4.5	64.2±2.8	69.3±4.6	63.7±3.7	61.6±9.6
*CO2 (ppm)	Carbon dioxide	426.7±14.8	412.8±1.2	426.3±2.4	424.1±2.8	425.2±2.5	428.0±10.8
WindDi (°)	Wind direction	45.9±35.7	49.3±0.9	53.3±24.0	30.7±5.5	48.5±3.3	125.7±90.1
WindSp (m/s)	Wind speed	4.3±1.6	5.2±0.9	3.9±0.6	4.0±0.5	3.0±0.5	2.4±1.5
*Temp (°C)	Temperature	23.3±3.5	24.7±0.9	25.5±1.4	25.3±1.6	27.4±0.9	26.7±2.1
†SO2	Sulfur dioxide	2.6±1.2	3.2±0.2	3.4±0.1	3.5±0.2	3.2±0.1	4.4±0.8
†CO	Carbon monoxide	304.9±72	217.4±10.9	318.0±8.5	291.3±16.3	258.4±14.1	329.0±74.6
NH3	Ammonia	8.8±1.8	8.9±0.4	9.5±0.6	9.7±0.2	9.2±0.6	10.6±3.0
†NO	Nitrogen Monoxide	0.9±1.4	0.3±0.1	0.7±0.4	0.6±0.3	0.3±0.1	1.4±1.3
†NO2	Nitrogen Dioxide	3.9±3.5	1.6±0.7	4.5±1.1	3.4±1.4	1.1±0.5	10.1±5.6
†NOx	Nitrogen Oxides	4.8±4.4	1.9±0.7	5.2±1.2	4.0±1.6	1.4±0.5	11.4±6.2
†O3	Ozone	49.9±20.6	59.5±10.1	54.7±14.5	44.2±9.9	61.2±3.8	70.4±33.5
†JNO2 10^{-3} (s^{-1})	The photolysis rate constant of NO2	3.6±2.5	4.7±2.4	4.0±2.0	4.8±2.5	5.0±2.6	4.3±2.2
†HONO	Nitrous acid	0.15±0.069	0.15±0.019	0.16±0.035	0.29±0.101	0.14±0.015	NaN
*C2H4	Ethene	1.4±1.3	0.5±0.1	0.7±0.1	0.6±0.1	0.3±0.1	0.9±0.2
*C2H6	Ethane	1.9±0.9	1.4±0.1	2.1±0.1	2.0±0.1	1.7±0.1	2.3±0.5
*C3H8	Propane	1.7±0.9	1.1±0.2	1.5±0.2	1.3±0.1	0.8±0.1	2.1±1.7
*C3H6	Propene	0.10±0.05	0.07±0.01	0.11±0.02	0.18±0.06	0.06±0.01	0.12±0.04
*C2H2	Ethyne	1.63±0.65	0.97±0.03	1.42±0.23	1.07±0.08	NaN	1.39±0.48
*IC4H10	i-Butane	0.55±0.44	0.22±0.04	0.61±0.14	0.44±0.09	0.23±0.07	1.02±1.04
*NC4H10	n-Butane	0.76±0.60	0.27±0.06	0.88±0.19	0.67±0.13	0.32±0.08	1.53±1.62
*TBUT2ENE	But-2-ene	0.06±0.01	0.05±0.00	0.06±0.00	0.05±0.00	NaN	0.06±0.01
*BUT1ENE	But-1-ene	0.08±0.03	NaN	0.10±0.01	0.08±0.01	NaN	NaN
*IC5H12	i-Pentane	0.40±0.22	0.18±0.04	0.42±0.05	0.46±0.03	0.28±0.11	0.60±0.36
*NC5H12	n-Pentane	0.24±0.12	0.13±0.02	0.24±0.02	0.33±0.05	0.17±0.04	0.29±0.21

*C4H6	Buta-1,3-diene	0.06±0.01	NaN	0.06±0.00	NaN	NaN	0.06±0.00
*M2PE	2-Methyl pentane	0.31±0.14	NaN	0.28±0.05	0.30±0.04	0.20±0.00	0.36±0.27
*NC6H14	n-Hexane	0.15±0.11	0.08±0.01	0.15±0.04	0.10±0.03	0.05±0.00	0.28±0.28
*IC8H18	i-Octane	0.02±0.02	NaN	0.02±0.01	NaN	NaN	0.05±0.06
*NC7H16	n-Heptane	0.03±0.01	NaN	0.07±0.00	NaN	NaN	0.07±0.00
*NC8H18	n-Octane	0.03±0.00	NaN	0.03±0.00	NaN	NaN	0.03±0.00
*EBENZ	Ethyl Benzene	0.05±0.04	0.02±0.01	0.05±0.01	0.05±0.02	0.01±0.00	0.08±0.09
*MXYL	m-Xylene	0.03±0.03	0.01±0.00	0.03±0.01	0.03±0.01	0.01±0.00	0.02±0.02
*OXYL	o-Xylene	0.04±0.03	0.01±0.00	0.03±0.01	0.03±0.01	0.01±0.00	0.03±0.03
**CH2O2	Formic acid	1.02±0.44	0.58±0.08	1.03±0.19	1.16±0.20	1.55±0.11	1.54±0.47
**C2H4O2	Acetic acid	2.76±1.46	1.59±0.34	3.03±0.68	4.54±0.35	3.19±0.61	4.38±3.25
**C2H8O2	Ethylene dihydrate	0.06±0.02	0.06±0.00	0.06±0.01	0.05±0.00	0.04±0.00	0.09±0.06
**C5H8	Isoprene	0.31±0.24	0.16±0.06	0.36±0.14	0.69±0.46	0.56±0.33	0.54±0.25
**C4H6O	Methyl Vinyl Ketone+ Methacrolein	0.16±0.10	0.06±0.01	0.22±0.06	0.26±0.05	0.15±0.06	0.32±0.19
**C3H4O2	Acrylic acid	0.12±0.05	0.06±0.01	0.13±0.03	0.16±0.02	0.13±0.02	0.19±0.10
**C3H6O2	Propanoic acid/ Hydroxy acetone	0.90±0.43	0.57±0.15	0.97±0.23	1.26±0.03	1.01±0.11	1.45±0.93
**C6H6	Benzene	0.28±0.13	0.12±0.03	0.33±0.03	0.43±0.04	0.25±0.05	0.38±0.21
**C6H12	Cyclohexane	0.02±0.01	0.01±0.00	0.03±0.00	0.03±0.01	0.02±0.01	0.04±0.03
**C3H4O3	Pyruvic acid	0.05±0.02	0.03±0.00	0.05±0.01	0.07±0.01	0.07±0.00	0.06±0.03
**C7H8	Toluene	0.38±0.27	0.20±0.10	0.46±0.11	0.50±0.08	0.24±0.04	0.69±0.67
**C8H10	Xylene	0.25±0.22	0.09±0.08	0.35±0.07	0.49±0.17	0.07±0.05	0.41±0.34
**C10H16	Monoterpene	0.05±0.03	0.03±0.00	0.06±0.01	0.10±0.06	0.09±0.04	0.07±0.03
**CH2O	Formaldehyde	1.03±0.41	0.62±0.05	1.17±0.11	1.72±0.10	1.59±0.17	1.17±0.42
**C2H4O	Acetaldehyde	1.88±0.90	0.98±0.13	2.10±0.41	2.74±0.16	1.96±0.36	3.17±1.98
**C3H6O	Acetone	3.88±1.60	2.18±0.31	4.43±0.74	5.64±0.49	5.91±0.47	5.92±2.85
**C3H4O	Acrolein	0.25±0.11	0.14±0.02	0.29±0.05	0.39±0.04	0.33±0.05	0.39±0.19
**C4H8O	MEK + Butanals	0.45±0.30	0.24±0.04	0.53±0.16	0.59±0.05	0.44±0.05	0.87±0.86
**C8H8O	Methyl benzaldehyde	0.04±0.03	0.02±0.00	0.05±0.01	0.06±0.00	0.04±0.01	0.08±0.06
[&]BVOC	Biogenic VOCs	0.3±0.4	0.2±0.1	0.4±0.1	1.1±0.6	0.8±0.4	0.7±0.5
[&]AVOC	Anthropogenic VOCs	7.1±3.6	4.0±0.7	7.6±0.9	7.7±0.9	4.4±0.7	11.1±8.7
[&]OVOC	Oxygenated VOCs	7.2±7.4	7.0±1.0	9.2±1.5	18.6±1.3	16.4±1.9	14.9±12.8
[&]Arom	Aromatic compounds	0.6±0.6	0.4±0.2	0.8±0.1	1.5±0.3	0.6±0.1	1.2±1.3
[&]Alkane	Alkane	6.5±3.4	3.6±0.5	6.8±0.8	6.3±0.6	3.8±0.6	9.9±7.5
[&]Alkene	Alkene	2.5±1.9	0.5±0.1	2.2±0.2	2.6±0.2	1.0±0.5	2.5±1.0
[&]Aldehyde	Aldehyde	4.4±4.5	4.2±0.5	5.7±0.8	11.4±0.8	10.4±1.1	9.1±7.6
[&]Acid	Acid	2.8±2.9	2.8±0.5	3.4±0.6	7.2±0.5	5.9±0.8	5.8±5.2

Notes:

The concentration was averaged from the daytime (6:00 to 18:00) results.

The concentration unit is presented in the bracket in the ‘Species Abb.’.

The unit for other species is in ppb.

* Species measured by GC-MS and constrained by the model

** Species measured by PTR-MS and constrained by the model.

[†] Species measured by instrument specified in Table 1.

[&] Different VOCs functional groups.

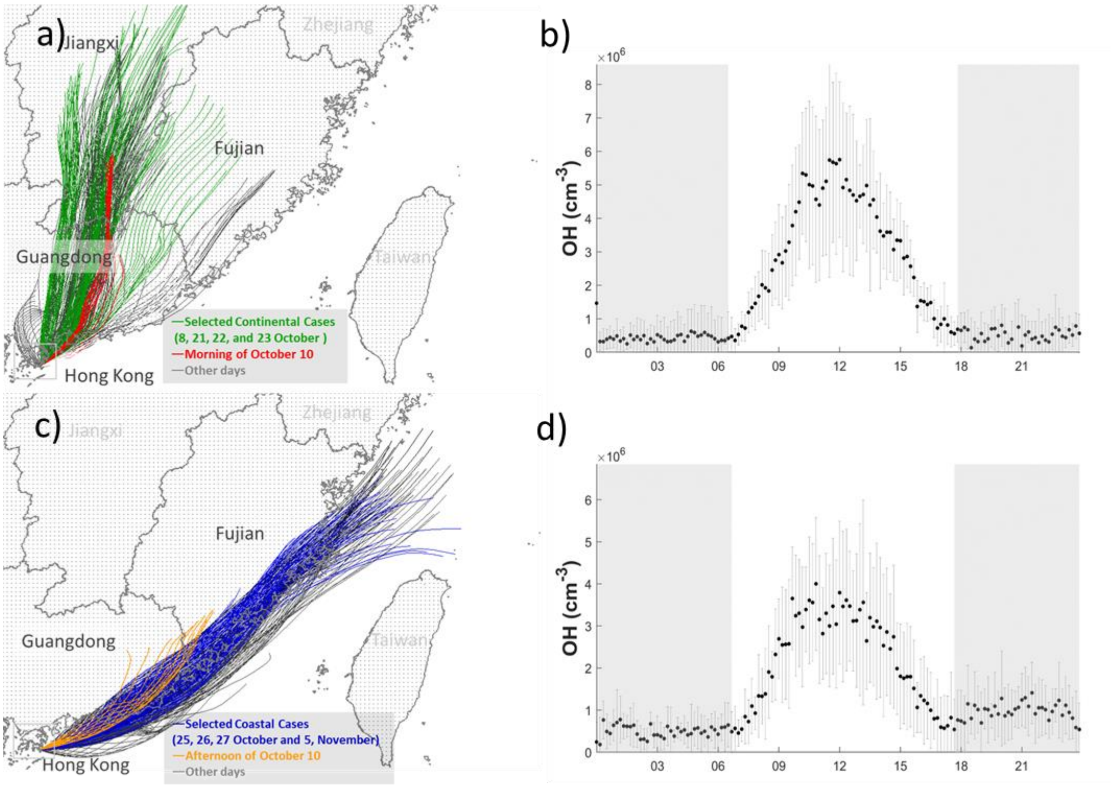

Figure 6.2.4 24 h back trajectories of the continental (a) and coastal (c) cases over the whole measurement period. The selected days for coastal, continental, and mixed cases are labeled in different colors. (b) and (d) show the average concentration of OH with standard deviation in continental and coastal air masses, respectively. The error bars and shaded error bars are the standard deviations of the averaged data.

Figure 6.2.4 shows the hourly backward trajectories over the whole campaign. Consistent with previous studies conducted at HT in the same season (Li et al., 2018; Peng et al., 2022), the air masses were dominated by continental air masses containing high concentrations of pollutants (Figure 6.2.4a) and less polluted coastal air masses (Figure 6.2.4c). In this study, we did not encounter oceanic air masses from the south. The average noontime OH concentration was $5.0 \pm 2.2 \times 10^6$ cm^{-3} in the continental air (Figure 6.2.4b) and $3.3 \pm 1.6 \times 10^6$ cm^{-3} in the coastal air (Figure 6.2.4d).

6.2.2 Model-observation Comparison

To investigate the performance of the MCM box model in simulating OH chemistry at our site, we selected 4 days featuring the continental air mass (8, 21, 22, and 23 Oct) and 4 days featuring the coastal air mass (25–27 Oct, 5 November) (Figure 6.2.5). We also selected 10 October as a specific case due to the shifting continental and coastal air masses within the same day during the daytime. These days were selected for model analysis because they comprised relatively complete chemical data that could be used to constrain the model. The below discussions focus on the comparison of the daytime results since the simulated night-time OH concentration was mostly within the measurement uncertainties and the night-time observations for Oct 08, 23, 27 and Nov. 5 were incomplete as shown in Figure 6.2.5.

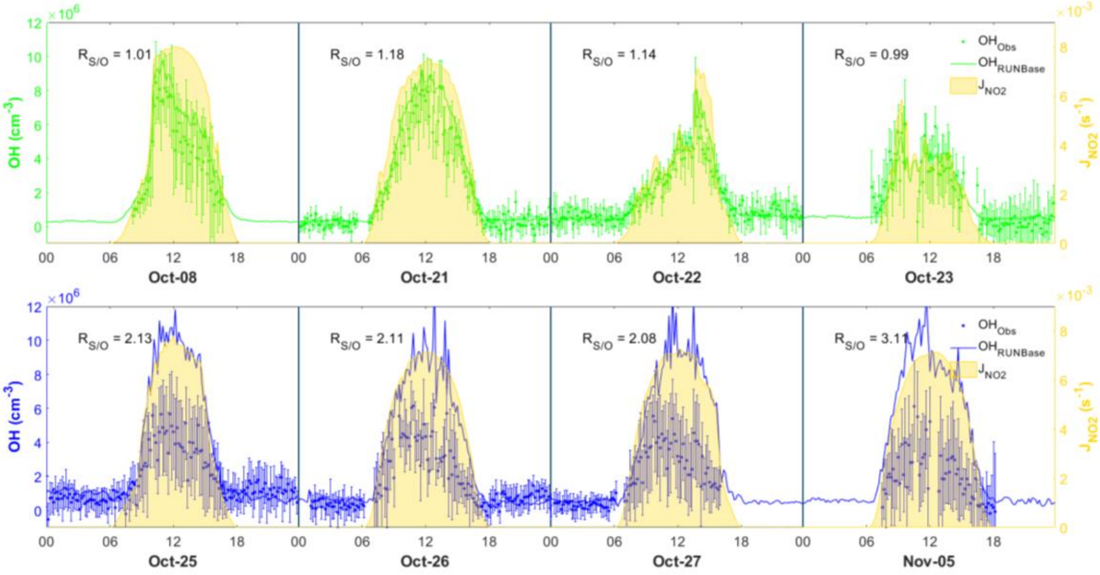

Figure 6.2.5 Comparison between observed (dots) and simulated (lines) OH in the four continental cases (top panel) and the four coastal cases (lower panel), also shows measurement uncertainty (error bars) and J_{NO2} measurement (yellow shades). The time zone was the local time (+8 UTC) for the x-axis.

6.2.2.1 Selected Continental Air Mass Cases

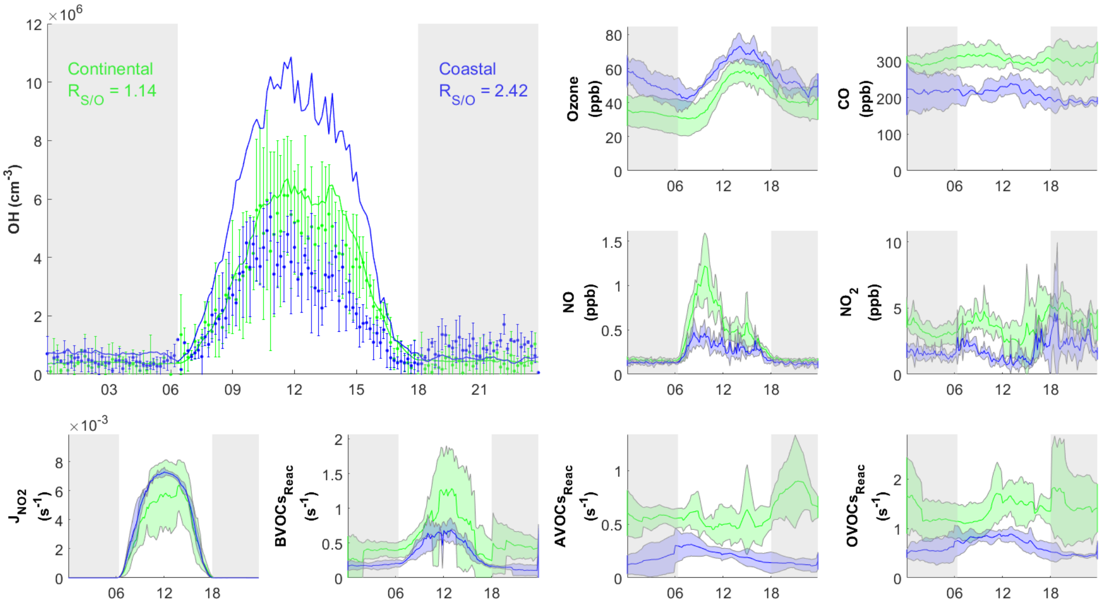

Figure 6.2.6 Diurnal profiles of average concentrations of measured (dots) with standard deviation and simulated (RUNBase, line) OH concentration, important trace gases, and the measured BVOCs, AVOCs, OVOCs reactivity ($BVOCs_{Reac}$, $AVOCs_{Reac}$, and $OVOCs_{Reac}$) for selected cases in continental (green) and coastal (blue) air masses. The grey shaded area denotes night-time. The error bars and shaded error bars are the standard deviations of the averaged data.

Figure 6.2.5 shows the comparison between the simulated and observed OH concentrations for the selected cases in the continental and coastal air masses (4 days each). The simulated OH concentrations of the four continental cases (8 October and 21–23 October) were mostly within the OH measurement uncertainty (2σ), with a daytime average $R_{S/O}$ of 1.14 (Figure 6.2.6), ranging from 0.99 to 1.18 (Figure 6.2.5). High NO_x (~ 5 ppb) and VOCs (~17 ppb) concentrations were measured for these days (Figure 6.2.6, Table 6.1). Therefore, in the continental polluted air mass, the existing MCM mechanism reproduced the observed OH concentrations well. On these days, the reaction between HO_2 and NO was the dominant OH formation pathway (78%), followed by O_3 photolysis (8%), HONO photolysis (6%), the reaction between ozone and HO_2 (2%), and alkene ozonolysis (< 2%; Table 6.2 and Figure 6.2.8). These results are similar to the findings of previous studies in the PRD conducted during autumn under polluted conditions (Tan et al., 2019). The removal of OH occurs mainly through its reaction with non-methane hydrocarbons (NMHCs; ~63%), CO (20%), NO_2 (9%), and CH_4 (4%; Table 6.2).

The simulated OH reactivity was 8.1 ± 1.0 s^{-1} on average for continental air masses (Figure 6.2.9), which is comparable to the OH reactivity measured at suburban sites which ranged from 5 to 30 s^{-1} but lower than that measured at the urban sites which ranged from 10 to 100 s^{-1} (Yang et al., 2016).

The simulated daytime average and peak HO_2 concentration were $2.1 \pm 1.2 \times 10^8$ cm^{-3} and 4.5×10^8 cm^{-3}, respectively, for continental air masses (RUNBase, Figure 6.2.10). The peak HO_2 value at our is lower than the result at a clean midlatitude forest area (10×10^8 cm^{-3}, Lew et al., 2020), and the average daytime value is higher than that measured at polluted urban sites in Beijing (0.3 to 0.4×10^8 cm^{-3}, Ma et al., 2019). The ratio of simulated HO_2 to observed OH (HO_{2SIM}/OH_{OBS}) was 147 averaged during on daytime (06:00-18:00) in continental cases.

6.2.2.2 Selected Coastal Air Mass Cases

In contrast to the continental air mass cases, the diurnal OH patterns in the coastal air mass category (25–27 October and 5 November) were not well reproduced by the model (Figure 6.2.5). The simulated results overestimated the observed OH concentration, with the daytime average $R_{S/O}$ of 2.42 (Figure 6.2.6) for these 4 case days (ranging from 2.08 to 3.11) (Figure 6.2.5). The coastal air masses showed statistically significant (i.e., p-value < 0.05) lower NO_x (−63%), AVOCs (−47%), BVOCs (−50%), OVOCs (−23%), and CO (−31%) concentrations compared with the continental cases (Figure 6.2.6, Table 6.1). The HO_2 and NO reaction was still the dominant source (69%) of OH in the coastal air masses, like in the continental air mass cases, but in a lower proportion than on continental days due to the lower NO concentration (Figure 6.2.8 and Table 6.2). The other major OH sources were O_3 photolysis (13.8%), HONO photolysis (7%), and the reaction between ozone and HO_2 (4%).

The simulated OH reactivity is $4.7 \pm 0.58\ s^{-1}$ on average for the coastal case (Figure 6.2.9), which is lower than the continental polluted air mass ($8.1 \pm 1.0\ s^{-1}$). As discussed below, low OH reactivity could have been the cause of the model's overestimation of OH concentrations in the coastal cases. The model's overestimation of OH in coastal air masses indicates gaps in our knowledge about the OH budget in relatively clean conditions with low NO_x and VOCs.

The simulated daytime average HO_2 concentration was $3.4 \pm 1.7 \times 10^8\ cm^{-3}$ for the coastal cases (RUNBase, Figure 6.2.10), which was ~ $1.2 \times 10^8\ cm^{-3}$ higher than the value in the continental polluted air mass. The simulated HO_2 level is comparable to the measured value at a rural site in Heshan ($3 \times 10^8\ cm^{-3}$, Tan et al., 2019). The HO_{2_SIM}/OH_{OBS} was 218 in coastal cases, higher than the ratio in continental cases. This could be explained by the lower NO concentration in the coastal cases that slows the recycling reaction of HO_2 back to OH (Sommariva et al., 2004; Shirley et al., 2006; Chen et al., 2010).

6.2.2.3 The October 10 Case Day

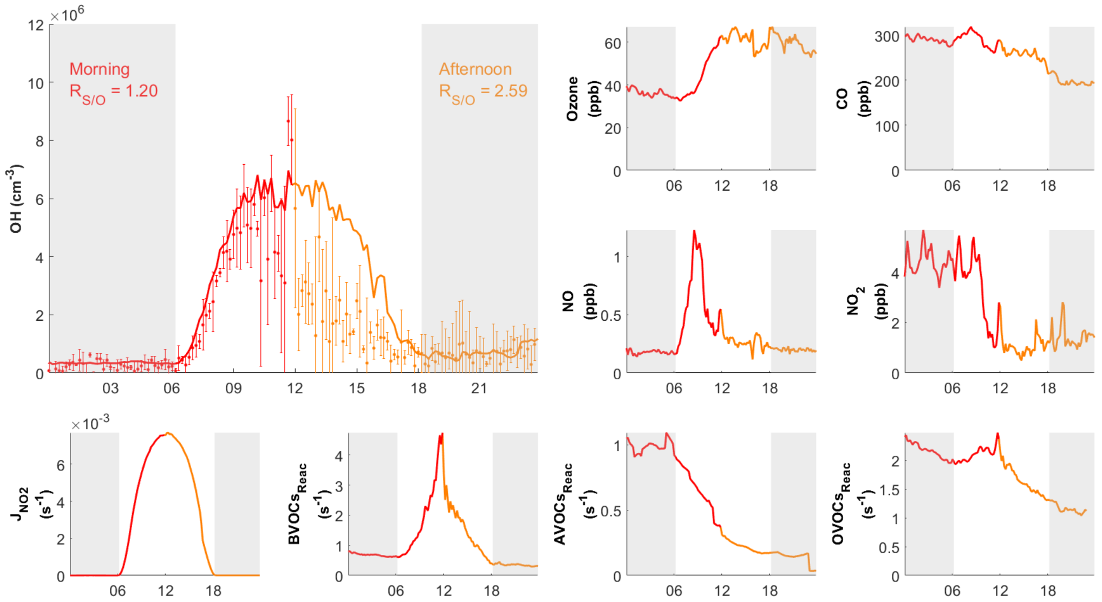

Figure 6.2.7 Diurnal profiles of measured (dots) with measurement uncertainty (error bars) and simulated (RUNBase, line) OH on 10 October 2020, with other chemical species and the measured BVOCs, AVOCs, OVOCs reactivity ($\text{BVOCs}_{\text{Reac}}$, $\text{AVOCs}_{\text{Reac}}$ and $\text{OVOCs}_{\text{Reac}}$). The air mass drifted from continental (red) in the morning to coastal (orange) in the afternoon. The grey shaded area denotes night-time. The time zone was the local time (+8 UTC) for the x-axis.

During the day on 10 October, our site received continental air masses between sunrise and noon and coastal air masses between noon and sunset. This served as another case that could be used to check the model’s performance on continental versus coastal air masses within the same day. On 10 October, the $R_{S/O}$ changed from 1.20 in the morning to 2.59 in the afternoon, driven by the air mass drift during continuous measurement without interruption (Figure 6.2.7). As with the continental and coastal results shown above, the afternoon of 10 October showed significantly ($p < 0.05$) lower concentrations of NO (−50%), NO_2 (−68%), and the reactivity of AVOCs (−42%), BVOCs (−27%), and OVOCs (−12%) compared with the morning (Table 4). With lower NO, the fraction of OH produced from HO_2 and NO reaction was also lower in the afternoon (65%) than in the morning (73%) (Figure 6.2.8 and Table 6.2). Similarly, the simulated total OH reactivity was lower in the afternoon (7.6 ± 2.3 s^{-1} on average) than in the morning (10.3 ± 1.6 s^{-1} on average; Figure 6.2.9). The simulated HO_2 was $3.6 \pm 2.4 \times 10^8$ cm^{-3} in the morning when continental air mass dominated and was $5.6 \pm 1.9 \times 10^8$ cm^{-3} in the afternoon when coastal air mass dominated (RUNBase, Figure 6.2.10). The HO_{2SIM}/OH_{OBS} was 142 in the morning and up to 476 in the afternoon. Again, higher HO_2 concentration and HO_{2SIM}/OH_{OBS} ratio were shown with low NO concentration.

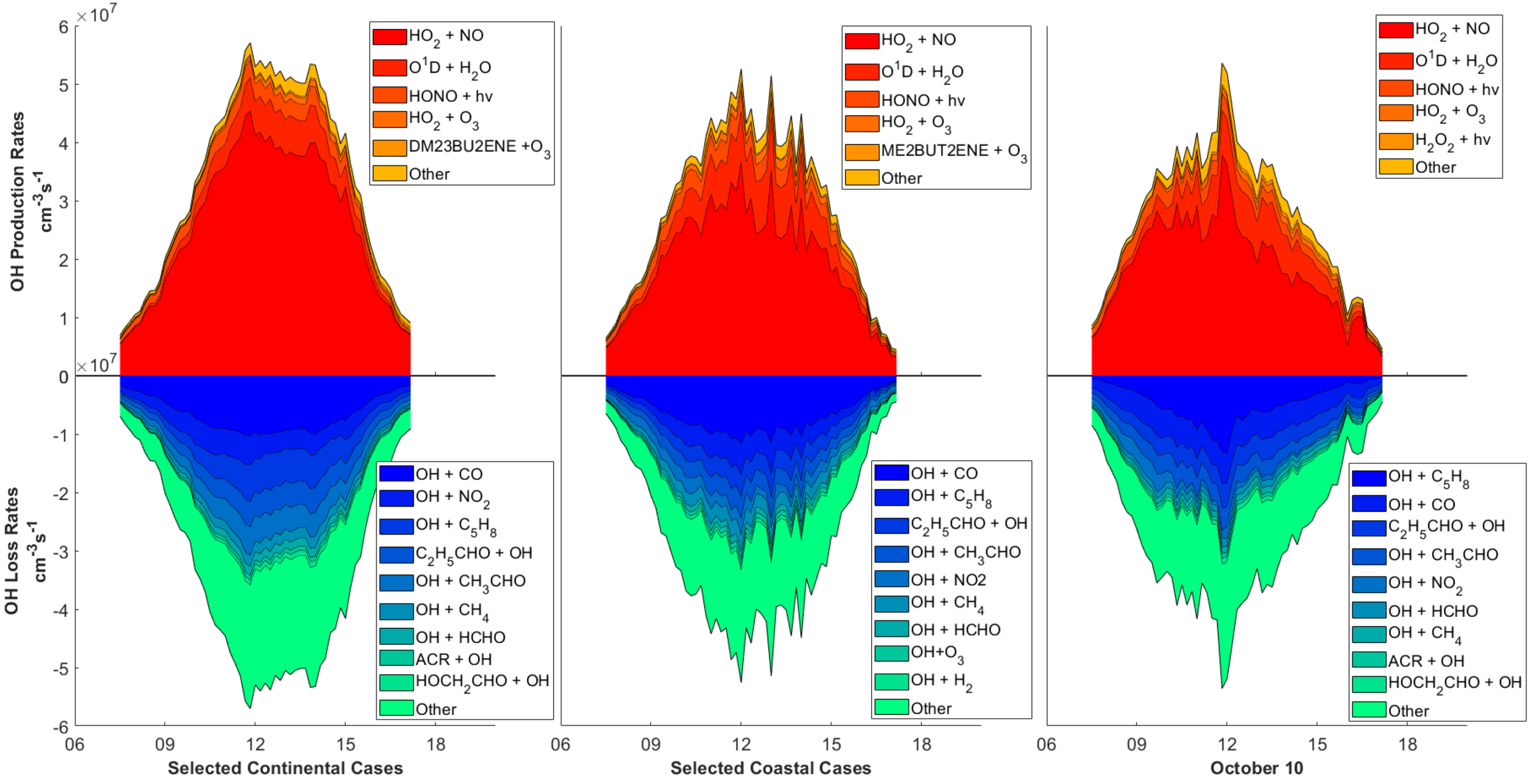

Figure 6.2.8 OH radical budgets for the continental cases, coastal cases, and 10 October. Where DM23BU2ENE and ME2BUT2ENE represent 2,3-Dimethyl-2-butene and 2-Methyl-2-butene respectively.

Table 6.2 OH budgets for the selected continental and coastal cases, the morning and afternoon of 10 October.

Continental Case		Coastal Case		Oct 10 Morning		Oct 10 Afternoon	
Production							
HO_2 + NO	77.66%	HO_2 + NO	69.02%	HO_2 + NO	73.17%	HO_2 + NO	65.11%
O^1D + H_2O	7.98%	O^1D + H_2O	13.80%	O^1D + H_2O	10.73%	O^1D + H_2O	15.04%
HONO + hv	5.78%	HONO + hv	7.32%	HONO + hv	8.65%	HONO + hv	7.16%
HO_2 + O_3	1.97%	HO_2 + O_3	3.60%	HO_2 + O_3	1.70%	HO_2 + O_3	3.80%
DM23BU2ENE + O_3	1.59%	ME2BUT2ENE + O_3	1.40%	H_2O_2 + hv	0.52%	H_2O_2 + hv	1.63%
Other	5.02%	Other	4.85%	Other	5.23%	Other	7.25%
Loss							
CO	19.91%	CO	23.39%	C_5H_8	15.96%	C_5H_8	15.38%
NO_2	9.38%	C_5H_8	8.17%	CO	14.68%	CO	13.72%
C_5H_8	9.09%	C_2H_5CHO	7.44%	CH_3CHO	8.76%	C_2H_5CHO	10.64%
C_2H_5CHO	7.96%	CH_3CHO	6.97%	C_2H_5CHO	8.31%	CH_3CHO	7.52%
CH_3CHO	7.94%	NO_2	6.27%	NO_2	5.70%	HCHO	3.44%
CH_4	3.68%	CH_4	5.91%	CH_4	3.04%	NO_2	3.33%
HCHO	2.79%	HCHO	2.50%	HCHO	3.03%	CH_4	3.06%
ACR	1.41%	O_3	2.04%	ACR	1.65%	ACR	1.71%
HOCH2CHO	1.36%	H_2	1.71%	$HOCH_2CHO$	1.61%	$HOCH_2CHO$	1.71%
Other	36.48%	Other	35.61%	Other	37.27%	Other	39.50%

Notes: The H_2 concentration was constrained as 550 ppb in the model simulation.

The H_2O_2 was simulated by the model with the average concentration of 0.95 ppb.

ACR- acrolein	HCHO: Formaldehyde
C_5H_8: Isoprene	$HOCH_2CHO$: Glycolaldehyde
C_2H_5CHO: Propanol	CH_3CHO: Acetaldehyde
ME2BUT2ENE: 2-Methyl-2-butene	DM23BU2ENE: 2,3-Dimethyl-2-butene

Other represents the group of the species that contribute less than 2% to the total OH reactivities. Most of them were the intermediate species produced by the reaction of OH with VOCs.

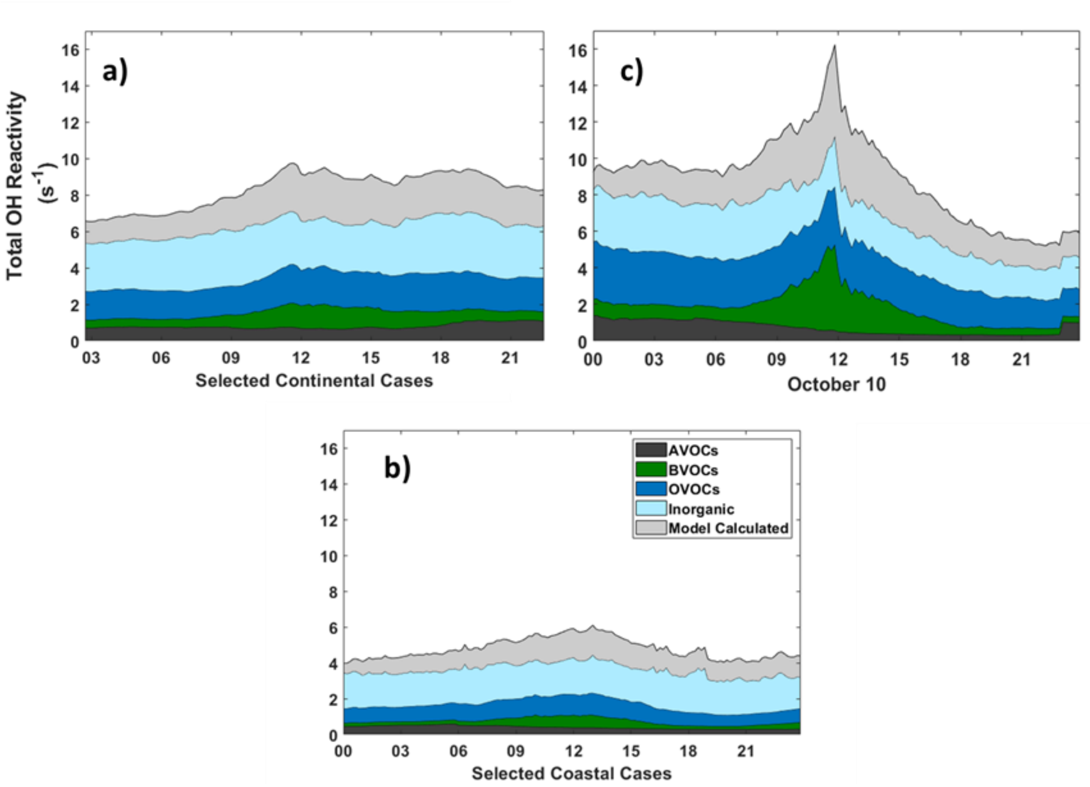

Figure 6.2.9 Simulated reactivity for continental cases (a), coastal cases (b), and 10 October (c). The AVOCs, BVOCs, OVOCs, and Inorganic demonstrate the reactivity calculated from the measured species and the Model Calculated represents the reactivity calculated by the derived species simulated by the model.

6.2.3 Discussion on the Model-observation Discrepancy

As discussed in the introduction, the model overestimation of OH could be caused by multiple reasons including the uncertainties of OH measurements (McKeen et al., 1997; Carslaw et al., 1999; Mauldin III et al., 2001a, 2010), the overestimate of OH sources (HO_2 and HONO) (Kanaya et al., 2007a; Zhang et al., 2006), and the underestimate of OH sinks (Berresheim et al., 2002; Creasey et al., 2003; Mauldin III et al., 2010; Griffith et al., 2016). The possible reasons for the OH overestimation in the coastal air mass is discussed below.

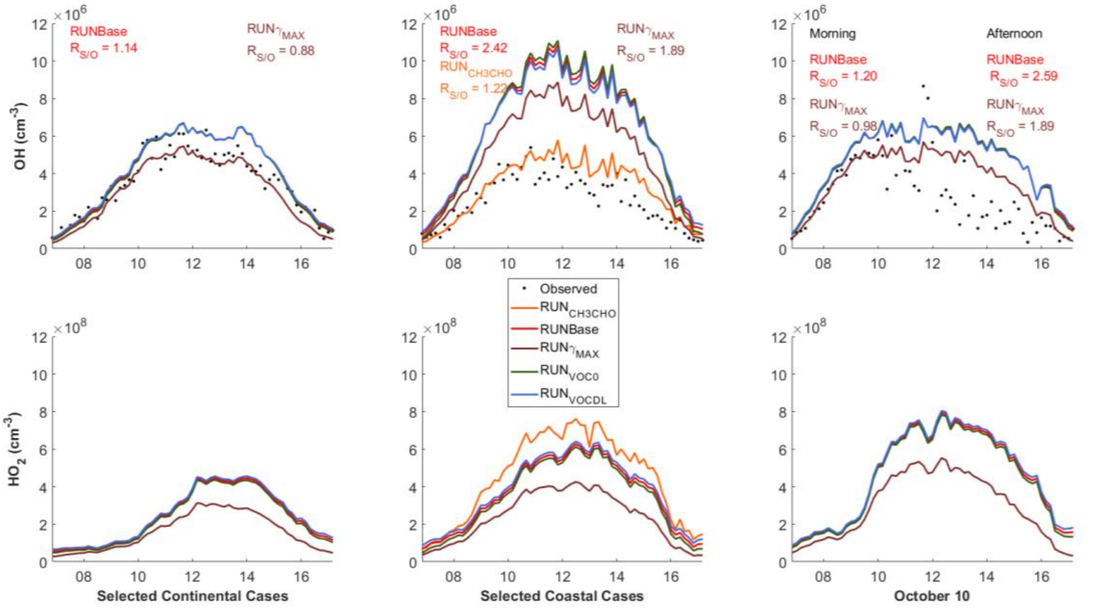

Figure 6.2.10 Sensitivity tests for the simulated OH and HO_2 in continental and coastal cases on 10 October. RUN_{CH3CHO} shows the simulated results of the selected coastal cases when additional CH_3CHO is added as OH sinks. $RUN\gamma_{MAX}$ shows the simulated results for the maximum heterogeneous uptake effect of HO_2 ($\gamma = 1$). The RUN_{VOC0} and RUN_{VOCDL} show the simulated results that constraint "0" and the detection limit value as the concentration of VOCs when their concentration was below detection limits.

The OH measurement uncertainties have been calculated as described in Section 4.6 and are shown as the error bars in Figure 6.2.5. The model's overestimation of OH in coastal air masses exceeded the measurement uncertainties (Figure 6.2.5 and Figure 6.2.6), and thus, the measurement uncertainty is unlikely to be the main reason for the discrepancy.

Model uncertainties in our study include the uncertainties in photolysis frequencies correction, uncertainties in the constrained VOCs concentrations when they were below detection limits, and uncertainties from not considering halogen chemistry.

On the first possibility, we acknowledge that the correction factor for photolysis frequencies due to cloud presence may be different for different species (Walker et al., 2022), thus, using a single correction factor (based on J_{NO2}) may introduce uncertainty in the model simulations. We think such uncertainty should not be significant because the weather was mostly sunny in the coastal cases. Regarding the uncertainty from the VOCs input, we conducted a sensitivity test to show that the treatment of VOCs that were below the detection limits should have a negligible effect on OH simulation (RUN_{VOC0} and RUN_{VOCDL} in Figure 6.2.10). We did not include halogen chemistry in our study as we wanted to compare our results with previous modelling work most of which did not consider halogen chemistry. Our other studies at the same site that did consider the halogen chemistry show a 4% increase in OH concentration from Cl chemistry (Peng et al., 2022) and 2.8% from Br chemistry (Xia et al., 2022), which would even increase the model-measurement in the coastal air mass discrepancy.

Our calculated OH budgets show that the main sources of OH in the coastal air masses were the HO_2 + NO reaction (69%), O_3 photolysis (14%), HONO photolysis (7%), and the reaction between ozone and HO_2 (4%). In the simulation, NO, HONO, and O_3 were constrained by observations. Could HO_2 be overestimated which would cause overprediction of OH? The main HO_2 sources are the VOCs oxidation by OH and the photolysis of OVOCs. In our study, VOCs and OVOCs were more likely under-measured than over-measured, which would underpredict HO_2 rather than overpredict it. In addition, not including the halogen chemistry would under-simulate HO_2 at this site (Peng et al., 2022; Xia et al., 2022).

We next examine the possibility of the underestimation of HO_2 sinks as the cause of the overprediction of OH. The major sinks of HO_2 include the reaction of NO to recycle OH, self-reaction to form H_2O_2 and heterogeneous loss by aerosol uptake. The first and second pathways have been considered in the MCM. The heterogeneous uptake of HO_2 onto aerosol was also included in our simulations with an uptake coefficient of 0.1. We conducted a sensitivity run by increasing the aerosol uptake of

HO_2 ($RUN\gamma_{MAX}$, Figure 6.2.10). Even when we set the uptake coefficient to unity (which is unlikely large), the simulated HO_2 concentration would decrease by 34% and the simulated OH $R_{S/O}$ would decrease to 1.73 from 2.42 in the base case. This indicates that the heterogeneous uptake of HO_2 is not the cause of the overestimation of OH in the coastal case. In summary, the discrepancy in modelled and observed OH in coastal cases is unlikely to be due to the overestimated HO_2.

The sensitivity tests for the change of sinks and sources were also performed as shown in Figure 6.2.11 and the $R_{S/O}$ for different cases is summarized in Table 6.3. These sensitivity test results show that in low NO conditions (<0.5 ppb), the OH concentration is more sensitive to the change of reactivity. The doubling inputs of organic compounds (RUNSink200%) in the selected continental case ($\Delta OCs = 17.2$ ppb) is larger than the selected coastal case ($\Delta OCs = 11.2$ ppb); however, the change of OH between RUNBase and RUNSinks 200% in selected continental ($\Delta OH_{daytime}=5.6\times10^5$ cm^{-3}) is smaller than that in selected coastal case ($\Delta OH_{daytime}=12.4\times10^5$ cm^{-3}). The October 10 case simulated OH also more sensitive to the change of sinks in the afternoon with low NO ($\Delta OH_{morning}=10.5\times10^5$ cm^{-3}, $\Delta OCs_{morning} = 27.4$ ppb, $\Delta OH_{afternoon}=11.4\times10^5$ cm^{-3}, and $\Delta OCs_{afternoon} = 21.6$ ppb). This can be explained by the HO_x cycle behaving differently in different NO conditions (Griffith et al., 2016). In high NO conditions like the urban site, the OH recycled from the HO_2 and RO_2 might buffer the OH concentration. On the other hand, in low NO conditions, the missing sinks caused by high OH loss cannot be compensated by the OH recycled from HO_2 and RO_2 (Griffith et al., 2016; Whalley et al., 2021). Therefore, in the low NO condition, the OH concentration is more affected by the missing sinks. This might explain the fact that the missing OH reactivity is found almost in all conditions (Yang et al., 2016); however, the overestimation due to missing reactivity mostly presents in relatively low NO conditions like coastal (NO <0.1 ppb) Carslaw et al., 1999; Berresheim et al., 2002), remote marine boundary layer (NO <0.1 ppb, Brune et al., 2020), clean condition of rural site (NO_x<3 ppb, Konrad, 2003) or the weekend of the urban site (NO <2 ppb, Griffith et al., 2016).

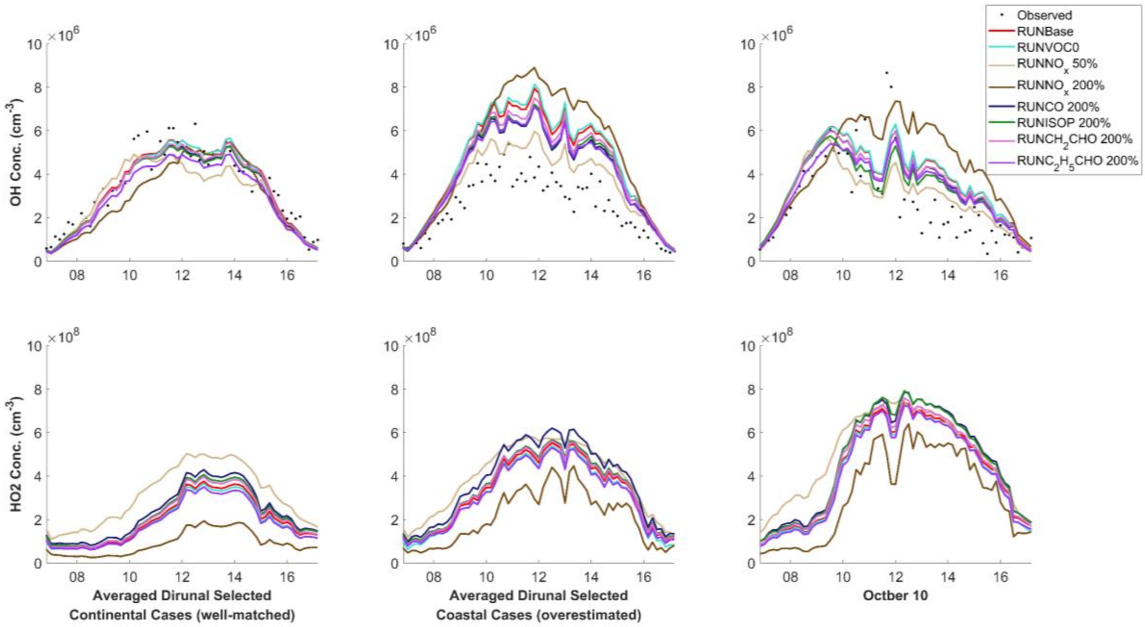

Figure 6.2.11 The sensitivity test results. VOC0 represents the result of constraining below detection limits species to zero as a minimum VOCs sink (RUNVOC0). RUNCO200% is the result of constraining double CO concentration. Similarly, RUNNO$_x$200%, RUNISOP200%, RUNCH$_3$CHO200%, and RUNC$_2$H$_5$CHO200% are the result of doubling the input of NO$_x$, isoprene, acetaldehyde, and propionaldehyde, respectively. The RUNNO$_x$50% is the halving NO$_x$ input result.

Table 6.3 The Averaged $R_{S/O}$ ratio for different sensitivity tests in Figure 6.2.11

Sensitivity Test Labels	Selected Continental Diurnal	Selected Coastal Diurnal	10 October (morning)	10 October (afternoon)
RUNBase	**1.14**	**2.42**	**1.20**	**2.59**
RUNγ1	0.77	1.40	0.93	1.49
RUNVOC0	0.96	1.75	1.08	1.84
RUNSinks 200%	0.82	1.28	0.82	1.23
RUNNO$_x$ 50%	0.87	1.35	0.91	1.34
RUNNO$_x$ 200%	0.83	1.90	1.09	2.46
RUNCO 200%	0.92	1.56	1.04	1.69
RUNISOP 200%	0.93	1.60	0.97	1.59
RUNCH$_2$CHO 200%	0.94	1.64	1.03	1.71
RUNC$_2$H$_5$CHO 200%	0.85	1.54	0.96	1.61

Based on the above discussions, we propose that the model's overestimation of OH could have been caused by unmeasured species that were not included in the model as OH sinks. We attempt to estimate the magnitude of possible OH sinks and investigate which factors could be important to these sinks. We added an artificial loss reaction into the model with the reactivity of k_{miss} (s^{-1}) and assumed that the reaction product would not participate in further reactions. Assuming a pseudo-steady state of OH during the daytime (P = k[OH]), k_{miss} was calculated as follows:

E 6.1

$$k_{miss} = \frac{P_{constrain}}{[OH_{obs}]} - \frac{P_{constrain}}{[OH_{sim}]}$$

where $P_{constrain}$ is the model's calculated OH production rates, with OH constrained by observations; $[OH_{obs}]$ is the observed OH concentration; and $[OH_{sim}]$ is the OH concentration simulated in RUNBase. After introducing the OH sink with k_{miss} into the model, the model better reproduced the observed OH concentrations on the coastal case days, with daytime $R_{S/O}$ close to unity (RUNKmiss, Figure 6.2.12) The average daytime

k_{miss} for the coastal cases was 5.0 ± 2.6 s^{-1}, which is larger than the total calculated reactivity in coastal cases (4.7 ± 0.6 s^{-1}). The calculated k_{miss} should be a lower limit of the possible missing sinks as the products from the reactions of OH with unknown species are most likely to further react with the missing source to produce RO_2 and HO_2 and recycle back to OH. We conducted a sensitivity test in which we assume the missing sink is resulting from under-measured CH_3CHO. Results show that CH_3CHO concentrations would increase by 20 times (RUN_{CH3CHO}) to make up the missing OH sinks and the missing reactivity with the cycling of the CH_3CHO oxidation products would increase to 7.2 s^{-1} (Figure 6.2.10).

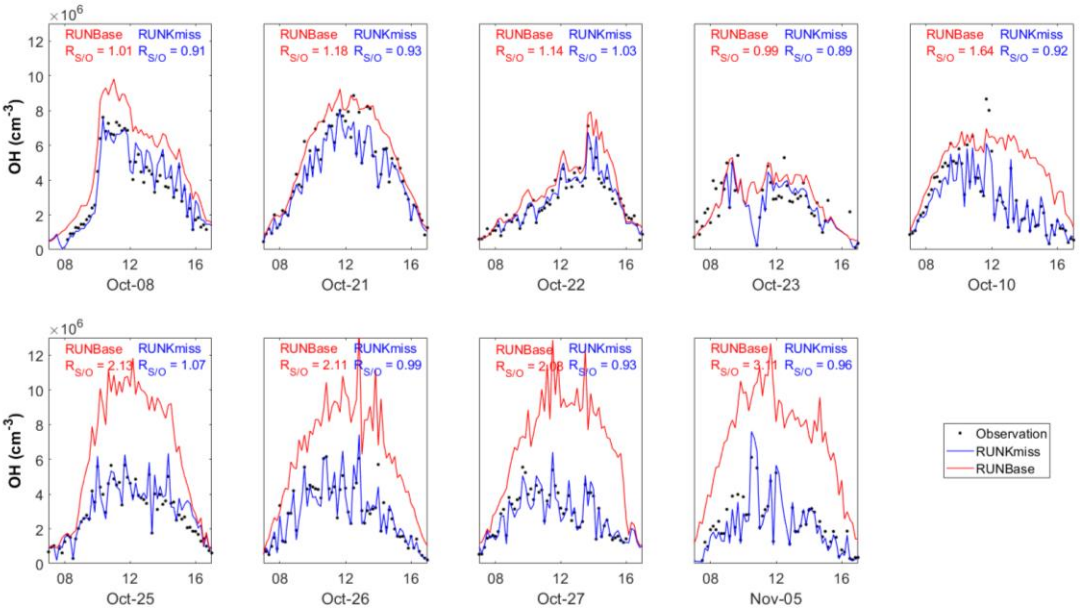

Figure 6.2.12 Nine-day comparison between observed OH and simulated OH with (RUNBase) and without (RUNKmiss) addition reactivity.

Here we next explored the dependence of k_{miss} on different trace gases. Figure 6.2.13a shows the correlation between k_{miss} and NO concentration for the nine days (including 10 October) during 09:00-15:00. At NO > 0.5 ppb, k_{miss} is close to zero. At NO < 0.5 ppb, k_{miss} tends to increase with decreasing NO. Similarly, k_{miss} trends to be zero at high NO_2 (> 2.5 ppb), TEXs (> 0.25 ppb), and AVOCs (> 5 ppb, Figure 6.2.13), and it increases with decreasing concentrations of NO_2, TEXs, and AVOCs. High k_{miss}

mainly occurs at the low toluene/benzene ratio and low C_2H_2/CO ratio, which are indicators of the aged air mass (Figure 6.2.13) (Xiao et al., 2007; Kuyper et al., 2020).

Therefore, while we cannot completely rule out other possibilities, we argue that the aged coastal air masses could have contained unmeasured species such as oxygenated organic molecules (OOMs; Nie et al., 2022) and ocean-emitted gases (Thames et al., 2020) that contributed to the missing OH reactivity, causing the model to overestimate OH concentrations on the coastal case days.

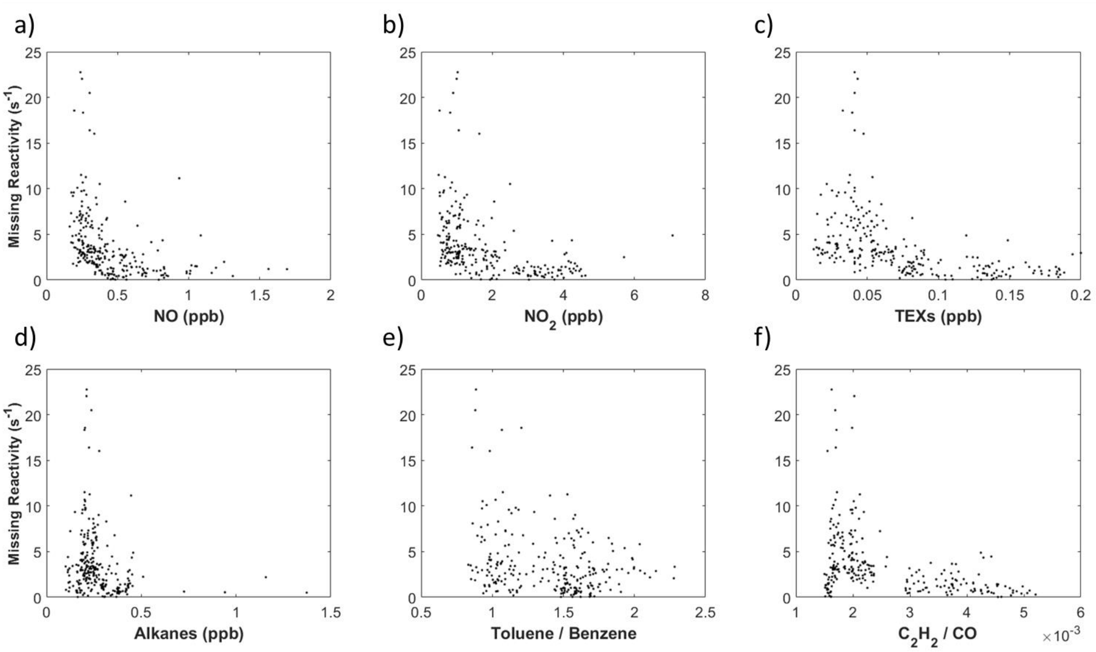

Figure 6.2.13 The dependence of calculated missing reactivity on a) NO, b) NO_2, c) TEXs (toluene, ethylbenzene, and xylenes), d) alkanes (C_2 to C_8), e) the ratio of toluene to benzene, and f) the ratio of C_2H_2 to CO.

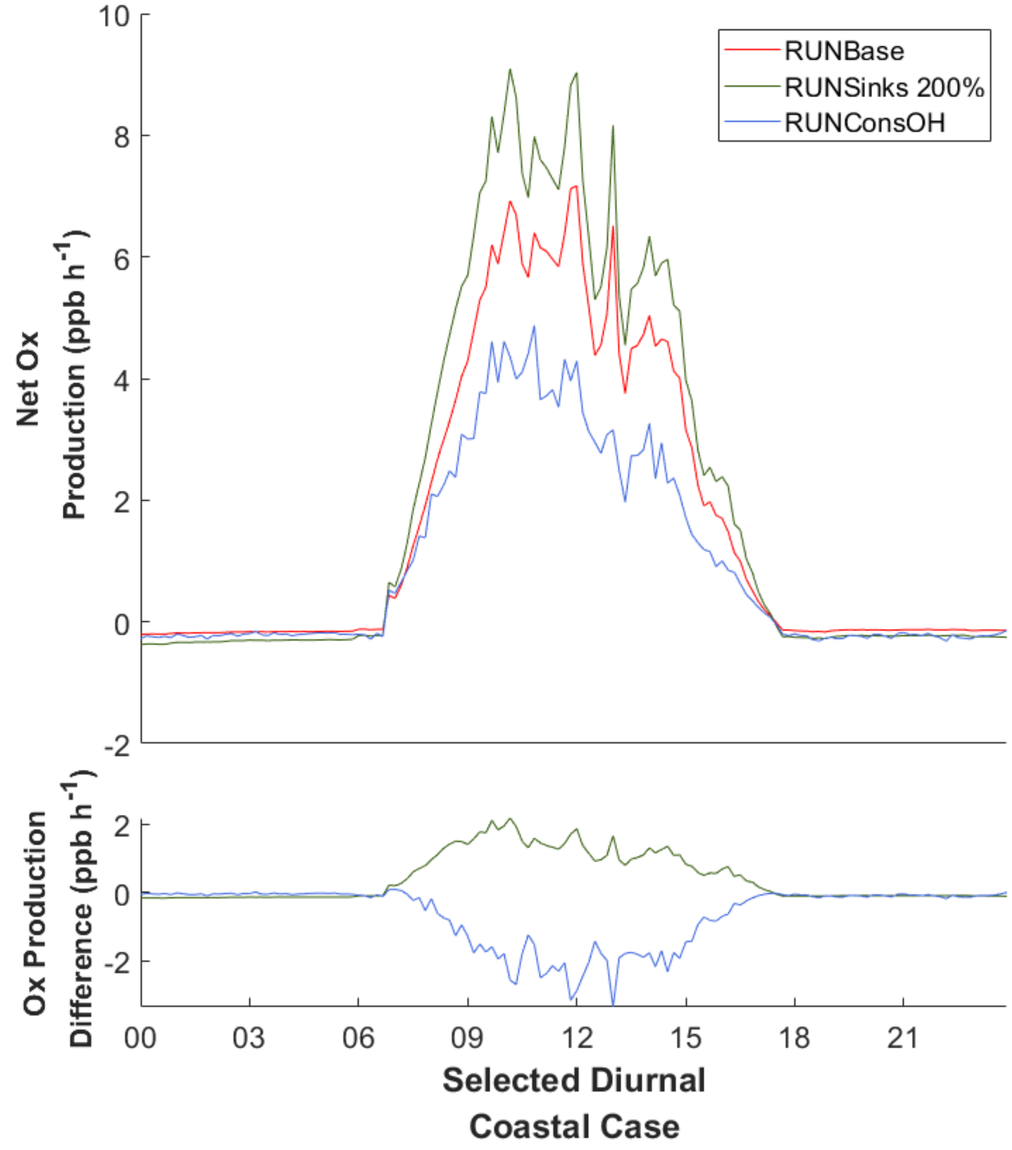

Figure 6.2.14 Net O_x (Ozone+NO_2) production estimation for coastal air mass by MCM v.3.3.1 with (RUNConsOH) and without OH constraint (RUNBase). RUNSinks 200% represents the O_x production calculated by doubling organic compounds inputs.

To investigate the effect of overestimation on pollutants production, Figure 6.2.14 shows the O_x production with different inputs as an example. With the observed OH implemented into the model, the O_x (O_3+NO_2) production rate decreases by -3 ppb h^{-1} (Figure 6.2.14, RUNConsOH). However, with the extra sinks which can further participate in the OH-HO_2 recycling (Figure 6.2.14, RUNSinks 200%), the O_x

production rate will increase by 2 ppb h^{-1} compared to the RUNBase which is similar to the previous study (Kohno et al., 2022). Whatever the cause; the O_x production affected by the overestimation of OH radicals state the impact of discrepancy of OH in low NO_x conditions. Other species' fate and lifetime like methane (Stevenson et al., 2020), and VOCs (Travis et al., 2020) are directly related to the OH concentration. Thus, further study of the OH discrepancy and missing reactivity in low NO conditions are necessary for the global estimation of the atmospheric oxidation process.

6.3 Hok Tsui HO_x and H_2SO_4 Measurement (2021-22)

The overestimation of OH found in 2020 needs the HO_2 measurement for further investigation. Thus, in the third campaign in Hok Tsui, we tested the upgraded CIMS for not only OH but also HO_2 and H_2SO_4 measurements.

By applying the analysis method discussed in section 4.7, the NO residual problem can be monitored during OH measurement. Figure 6.3.1 shows the CIMS measurement results for the whole campaign. From 25, December 2021, to 13, January 2022, ten days of results were collected by CIMS. The OH measurement is not available for 12 and 13 January 2022, after a one-week operation without cleaning the inlet and injectors. However, the H_2SO_4 and HO_2 measurements of the last two days were not affected by the residual problem and were available for the whole period.

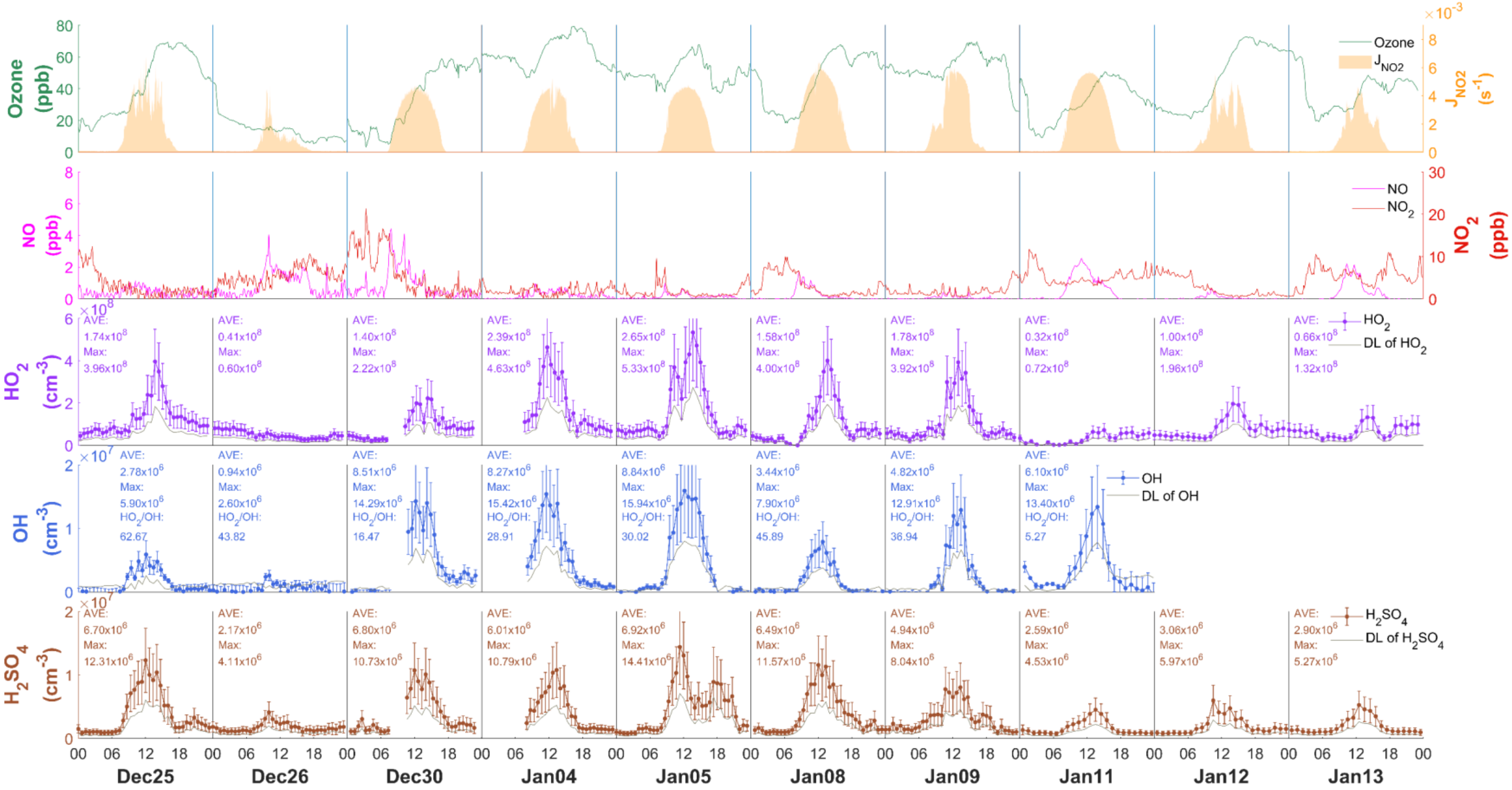

Figure 6.3.1 Time series of 10 mins trace gases (Ozone, J_{NO2}, NO, and NO_2) and CIMS measurement results (HO_2, OH, and H_2SO_4) from 25 December 2021 to 13 January 2022. The CIMS results are shown with the daytime averaged concentration (AVE), maximum concentration (Max), measurement uncertainty (error bar), HO_2 to OH ratio (HO_2/OH), and detection limits (DL), respectively.

Figure 6.3.1 shows the time series of observed HO_2, OH, and H_2SO_4 concentrations with the concentrations of other trace gases during the campaign. Compare to the HT 2020 campaign, the solar radiation (J_{NO2}) was relatively low due to the Winter season, and most of the cases peaked below 6 × 10^{-3} s^{-1}. Ozone ranged from 20 to 80 ppb in the daytime which was similar to the HT 2020 conditions. The NO concentration was mostly above 0.5 ppb in the daytime and above 2 ppb on the daytime of 26, 30 December, and 13 January. NO_2 show typical diurnal patterns that peaked at around 10 ppb in the morning.

All CIMS measured species are mostly above detection limits (grey line) and peak on 5 January 2021 (HO_2: 5.33 × 10^8 cm^{-3}, OH: 15.94 × 10^6 cm^{-3}, and H_2SO_4: 14.41 × 10^6 cm^{-3}), and have the lowest daytime peak concentration on 26 December 2022 (HO_2: 0.6 × 10^8 cm^{-3}, OH: 2.6×10^6 cm^{-3}, and H_2SO_4: 4.11 × 10^6 cm^{-3}) with the lowest J_{NO2} value (< 4 × 10^{-3} s^{-1}) and Ozone concentration (< 20 ppb). The campaign averaged peak concentrations for HO_2, OH and H_2SO_4 were 2.86 × 10^8 cm^{-3}, 8.43 × 10^6 $cm^{-3,}$ and 7.69 × 10^6 cm^{-3}, respectively.

The HO_2 averaged peak concentration close to the continental cases simulated result (3.75 × 10^8 cm^{-3}) in HT 2020 and lower than the coastal result (5.51 × 10^8 cm^{-3}) (Figure 6.2.10). This concentration is also relatively low when compared to the other HO_2 measurements in forest results as shown in Table 2.2 (e.g. 10.5 × 10^8, > 20 × 10^8, and 7 × 10^8, from Lelieveld et al., 2008; Griffith et al., 2013; and Wolfe et al., 2014, respectively) and the nearest suburban sites in Peking University Shenzhen Graduate School (PKUSZ shown in Figure 2.2.1) which peaked at around 4.2 × 10^8 cm^{-3} in the measurement period from October to November. However, when compared to the other HO_2 results in the winter season (2× 10^8 cm^{-3}, Sommariva et al., 2004), the coastal site (1.45 × 10^8 cm^{-3}, Kanaya et al., 2007a) and some urban sites (e.g. peak range: 0.5 to 6 × 10^8 cm^{-3}, Ren, 2003a) measurements the concentration is in a reasonable range (See other results in Table 2.2).

The H_2SO_4 concentrations are also consistent with the previously observed concentration in the coastal site. Previous studies measured H_2SO_4 at the coastal (Berresheim et al., 2003) and mountain (Berresheim et al., 2000; Birmili et al., 2000) sites by CIMS show maximum concentration up to 10 × 10^6 cm^{-3}. These comparisons imply that the H_2SO_4 concentrations observed in this campaign are in the reasonable range.

The OH concentrations, on the other hand, are higher than most of the previous measurement results in HT 2020. Especially the concentrations measured before and after the new year that have a maximum concentration higher than 10 × 10^6 cm^{-3}. Such high concentrations are comparable to the episode in HT 2020 and the result was dominated by polluted air mass presented previously (e.g., Berresheim et al., 2002; Dusanter et al., 2009a; Lu et al., 2013a; see Table 2.2 for the exact concentrations in these studies and more examples). Due to the previously observed winter pollution event in the PRD region (Fu et al., 2019) and the high OH observed in winter haze events with relatively weak solar radiation (Slater et al., 2020), this elevated OH concentration might be related to the pollution events in the wintertime. However, the ozone and NO_x concentration didn't show higher concentrations these days. Thus, further analysis of the other trace gases is necessary.

The HO_2 to OH ratio (HO_2/OH) is used as an indicator for the HO_2 to OH recycling process (Chen et al., 2010). The measured daytime averaged HO_2/OH variate from 16.47 (December 30) to 62.67 (December 25). It is noted that when the NO concentration was above 2 ppb on 30 December and 11 January, the HO_2/OH ratio was less than 20 which implies the faster recycling process from HO_2 to OH during relatively high NO concentrations. The HO_2/OH ratio in previous studies variated in different conditions and didn't show any tendency. The ratios in this campaign consisted of previous results in polar (Mauldin III et al., 2010), urban (Griffith et al., 2016), and forest (Feiner et al., 2016) sites with different NO conditions. The HO_2/OH ratio and comparison imply that recycling is not only affected by NO but also other mechanisms in different conditions.

Another breakthrough for the CIMS development besides HO_2 measurement in this campaign is the measurement of H_2SO_4. The successful measurement of H_2SO_4 represents the potential of CIMS to simultaneously measure other species during HO_x measurement. The measurement of H_2SO_4 was achieved without any injection through the front injectors. The rear injector flows including the N_2, HNO_3, and scavenger gases. Therefore, the CIMS in such mode is capable to measure the species that are available for traditional nitrate CIMS and will not react with the scavenger gases. For example, methane sulfonic acid (MSA; Berresheim et al., 2002) and nitrophenol (Nie et al., 2022) can be possible targets for further measurement.

This development for simultaneous measurement was done previously in CIMS with the addition of isotopic $^{34}SO_2$ (Mauldin III et al., 2004). However, the method in this study achieved the same purpose at a lower cost. Besides, this method is available for measuring other species besides HO_x. If the CIMS uses isotopic $^{34}SO_2$ and applies the front valve to switch off the front injectors at the same time, the CIMS can achieve low detection limits and low uncertainty for both HO_x and other species measurements.

It is noted that this thesis only shows the preliminary results and simple analysis of this campaign. Further analysis and discussion of the OH, HO_2, and H_2SO_4 results with the other trace gases and meteorological data will be shown in the coming article.

7. Summary and Future Research

7.1 Key Findings

This thesis reports the detailed development process for the measurement of OH, HO_2, and H_2SO_4 by chemical ionization mass spectrometer. Compared to the existing CIMS in the other research groups, The CIMS in PolyU not only measured HO_x family but also H_2SO_4 at the same time without the expensive isotopic $^{34}SO_2$ addition. Compared to the previous measurement methods (LIF and DOAS), CIMS has a better cost-performance ratio due to its low price and the potential for multiple species (e.g., MSA and nitrophenol) measurement.

Secondly, this thesis reports the details of the calibration system, the measurement principles, and the working theory of the CIMS for HO_x and H_2SO_4 measurement. A series of comparisons of different components of CIMS (ion sources, scavenger gases, and primary ions detection) have been conducted to optimize the performance of the CIMS for measurement. ^{210}Po has lower artificial OH interference compared to a corona ionizer, and it is adopted as the ion source. C_3F_6 is a better HO_x scavenger than C_3H_8 due to the capability of removing the HO_2 radicals. A set of procedures has been developed to optimize the flow rates of sample gas, sheath gas, and N_2 buffer gas, voltages on the sample inlet system, and the concentration of NO and SO_2, the conversion gas with the aim to increase the instrument's sensitivity and reduce noise. The CIMS instrument achieved a detection limit of 1.5×10^5 cm^{-3} and an uncertainty of 38% (S/N = 2) under laboratory conditions. Even though the optimal values of instrument parameters may differ in different CIMS systems due to the different designs and/or configurations, the procedures, and results of the tests from this thesis provide a useful reference to other researchers who wish to apply the CIMS technique to measure atmospheric HO_x radicals and H_2SO_4. Additionally, the development experiment for this CIMS might inspire the further development of other instruments that aim to tackle highly reactive species like Cl and Br.

Three field campaigns were performed in Hong Kong. The first campaign aims to test the capability of OH after development and sensitivity test. In the field, a clear diurnal profile with a maximum of 6×10^6 cm^{-3} was observed. The detection limit increased to about 8×10^5 cm^{-3} on clear days, with an overall accuracy of about 51%. The results have demonstrated the capacity of this instrument in measuring ambient OH in an urban site on clear days. This is the first result of OH measurement in Hong Kong.

In the second field campaign, we measured OH concentrations using CIMS at a coastal site in Hong Kong in the autumn of 2020 to gain insights into the atmospheric oxidative capacity and to evaluate the performance of a box model in the coastal atmosphere. The daily maximum OH concentration ranged from 2.1 to 15.4×10^6 cm^{-3} over the whole campaign, with an average of $4.9 \pm 2.1 \times 10^6$ cm^{-3}. The air masses were categorized into two groups based on their backward air trajectories: (1) continental air masses, which contained high concentrations of NO_x and VOCs, and (2) coastal air masses, which contained low concentrations of NO_x and VOCs. The observed OH concentration in the continental air parcels was on average 52% higher than in the coastal air parcels. The F0AM box model with comprehensive observational constraints generally reproduced the observed OH in the continental cases during the daytime, with a simulated/observed OH ratio ($R_{S/O}$) of 1.14 on average. However, the model significantly overestimated OH concentrations in the coastal cases, with an $R_{S/O}$ of 2.42 on average during the daytime. While we cannot completely rule out other possibilities, we incline to attribute this overestimation to a missing OH reactivity in the aged coastal air parcels that were not accounted for in the model. The lower limit of the missing OH reactivity was estimated at 5.0 ± 2.6 s^{-1} on average between 09:00 and 15:00 and was especially larger under low NO_x, low AVOCs, and aged air conditions. We hypothesize that unknown products from AVOCs oxidation or unknown OH-reacting gases emitted from oceans could contribute to the missing OH reactivity in aged coastal air masses. The overestimation of OH in the model could cause an overestimation of the formation of secondary aerosols, such as sulfate and nitrate, while the impacts would be even more complicated if it is due to missing chemical species which participated in ozone formation. Further studies are necessary to pin down the exact cause(s) of the OH overestimation by concurrently measuring HO_2 and OH reactivities, VOCs oxidation products, and ocean-emitted trace gases.

The last campaign tests the CIMS for HO_2 and H_2SO_4 measurement simultaneously during OH measurement at the same coastal sites in Hong Kong from winter 2021 to 2022. The newly developed data analysis method identified the unusual OH results due to the residual problem of NO after switching measurement targets from HO_2 to OH. By applying such a method and removing the abnormal results, CIMS is capable of HO_2, OH, and H_2SO_4 measurement. The measured daily maximum HO_2 variated from 0.60 to 4.63 × 10^8 cm^{-3}, OH variated from 2.6 to 15.42 × 10^6 cm^{-3}, and H_2SO_4 ranged from 4.11 to 10.79 × 10^6 cm^{-3}. After this development, the PolyU CIMS become the first instrument around the world that can measure OH, HO_2, and H_2SO_4 simultaneously without isotopic $^{34}SO_2$ for conversion.

7.2 Suggestions for Future Research

7.2.1 Further Development of CIMS

Although the residual problem of NO is monitored by the analysis method and mitigated by cleaning processes, the convenience and measurement frequency of the CIMS are decreased compared to the settings for OH measurement only. It is worthwhile to not only monitor but also figure out the solution for the residual NO. For example, the injection of a high concentration of Ozone for NO elimination might reduce the time for residential NO removal and increase the measurement effectiveness.

To enhance the quality and performance of data, additional laboratory and box modeling research should be conducted for the NO residual issue, as well as for the interference of HO_2 recycling during OH measurement. Moreover, it is necessary to investigate the potential wall loss in the stainless steel and other potential sources of interference for the CIMS instrument.

The OH reactivity can be measured by adding another pair of injectors in front of the existing front injectors. The conversion between OH and H_2SO_4 can be switched between the additional injectors and the existing injectors. Since the residual time for OH in the inlet will be changed when the conversion starts (R 1.24 to R 1.26) in a different position, by comparing the OH concentration measured during different injection positions of SO_2, the reactivity of OH can be determined. Besides that, by coupling with the flow tube, the indirect comparative reactivity method can also be conducted for OH reactivity measurement.

At last, the most impressive possibility of development is the additional measurement of other species. When the CIMS measured the H_2SO_4, only the scavenger gases and the N_2 from the pulsed flow were added. Therefore, theoretically, the CIMS is capable to observe the species that can be observed by the unmodified nitrate CIMS and will not react with scavenger gases. For example, the MSA (Mauldin

III et al., 2001b) and even the hydrotrioxide were found recently (Berndt et al., 2022). To achieve this purpose, further research on the reaction of target species with the reagent (nitrate), possible interference, and the calibration method needs to be studied.

7.2.2 Investigation of Discrepancy Problem in Low NO_x condition

As mentioned by the previous studies and supplied by the second campaign results, the reason for the discrepancy in the low NO_x area remains unknown. This discrepancy represents the knowledge gaps in our understanding of the atmosphere in the low NO_x condition. Therefore, it is still worthwhile to conduct more field campaigns for HO_x measurement, especially in low NO_x regions. Revisiting the coastal site in the same season with HO_2 and OH measurements might help further understand the overprediction in the coastal site as mentioned in section 6.2.3. On the other hand, the underprediction of OH found in the forest sites is also worth revisiting. An alternative measurement method might provide some hints for underprediction.

Besides that, the H_2SO_4 and OH radicals are closely related to the new particle formation. Therefore, the field campaign in the polluted area is also worthy to conduct for the new particle formation study. Additionally, the further development of CIMS will play an important role in the studies of atmospheric oxidation (by measuring HO_x radicals), new particle formation (by measuring OH, H_2SO_4), and marine atmosphere (by measuring OH, H_2SO_4, MSA).

Reference

Berndt, T., Chen, J., Kjærgaard, E. R., Møller, K. H., Tilgner, A., Hoffmann, E. H., Herrmann, H., Crounse, J. D., Wennberg, P. O., and Kjaergaard, H. G.: Hydrotrioxide (ROOOH) formation in the atmosphere, Science, 376, 979–982, https://doi.org/10.1126/science.abn6012, 2022.

Berresheim, H., Elste, T., Plass-Dülmer, C., Eiseleb, F. L., and Tannerb, D. J.: Chemical ionization mass spectrometer for long-term measurements of atmospheric OH and H_2SO_4, International Journal of Mass Spectrometry, 202, 91–109, https://doi.org/10.1016/S1387-3806(00)00233-5, 2000.

Berresheim, H., Elste, T., Tremmel, H. G., Allen, A. G., Hansson, H.-C., Rosman, K., Dal Maso, M., Mäkelä, J. M., Kulmala, M., and O'Dowd, C. D.: Gas-aerosol relationships of H_2SO_4, MSA, and OH: Observations in the coastal marine boundary layer at Mace Head, Ireland, Journal of Geophysical Research: Atmospheres, 107, PAR 5-1-PAR 5-12, https://doi.org/10.1029/2000JD000229, 2002.

Berresheim, H., Plass-Dülmer, C., Elste, T., Mihalopoulos, N., and Rohrer, F.: OH in the coastal boundary layer of Crete during MINOS: Measurements and relationship with ozone photolysis, Atmospheric Chemistry and Physics, 3, 639–649, https://doi.org/10.5194/acp-3-639-2003, 2003.

Berresheim, H., McGrath, J., Adam, M., Mauldin, R. L., Bohn, B., and Rohrer, F.: Seasonal measurements of OH, NO_x, and $J(O^1D)$ at Mace Head, Ireland, Geophys. Res. Lett., 40, 1659–1663, https://doi.org/10.1002/grl.50345, 2013.

Berresheim, H., Adam, M., Monahan, C., O'Dowd, C., Plane, J. M. C., Bohn, B., and Rohrer, F.: Missing SO_2 oxidant in the coastal atmosphere? – observations from high-resolution measurements of OH and atmospheric sulfur compounds, Atmospheric Chemistry and Physics, 14, 12209–12223, https://doi.org/10.5194/acp-14-12209-2014, 2014.

Birmili, W., Wiedensohler, A., Plass-Dülmer, C., and Berresheim, H.: Evolution of newly formed aerosol particles in the continental boundary layer: A case study including OH and H_2SO_4 measurements, Geophys. Res. Lett., 27, 2205–2208, https://doi.org/10.1029/1999GL011334, 2000.

Blocquet, M., Schoemaecker, C., Amedro, D., Herbinet, O., Battin-Leclerc, F., and Fittschen, C.: Quantification of OH and HO_2 radicals during the low-temperature oxidation of hydrocarbons by Fluorescence Assay by Gas Expansion technique, Proc. Natl. Acad. Sci. U.S.A., 110, 20014–20017, https://doi.org/10.1073/pnas.1314968110, 2013.

Bloss, W. J., Lee, J. D., Heard, D. E., Salmon, R. A., Bauguitte, S. J.-B., Roscoe, H. K., and Jones, A. E.: Observations of OH and HO_2 radicals in coastal Antarctica, Atmospheric Chemistry and Physics, 7, 4171–4185, https://doi.org/10.5194/acp-7-4171-2007, 2007.

Brauers, T., Hausmann, M., Bister, A., Kraus, A., and Dorn, H.-P.: OH radicals in the boundary layer of the Atlantic Ocean: 1. Measurements by long-path laser absorption spectroscopy, J. Geophys. Res., 106, 7399–7414, https://doi.org/10.1029/2000JD900679, 2001.

Brune, W. H., Miller, D. O., Thames, A. B., Allen, H. M., Apel, E. C., Blake, D. R., Bui, T. P., Commane, R., Crounse, J. D., Daube, B. C., Diskin, G. S., DiGangi, J. P., Elkins, J. W., Hall, S. R., Hanisco, T. F., Hannun, R. A., Hintsa, E. J., Hornbrook, R. S., Kim, M. J., McKain, K., Moore, F. L., Neuman, J. A., Nicely, J. M., Peischl, J., Ryerson, T. B., St. Clair, J. M., Sweeney, C., Teng, A. P., Thompson, C., Ullmann, K., Veres, P. R., Wennberg, P. O., and Wolfe, G. M.: Exploring Oxidation in the Remote Free Troposphere: Insights From Atmospheric Tomography (ATom), JGR Atmospheres, 125, https://doi.org/10.1029/2019JD031685, 2020.

Calvert, J. G., Lazrus, A., Kok, G. L., Heikes, B. G., Walega, J. G., Lind, J., and Cantrell, C. A.: Chemical mechanisms of acid generation in the troposphere, Nature, 317, 27–35, https://doi.org/10.1038/317027a0, 1985.

Cantrell, C. A., Zimmer, A., and Tyndall, G. S.: Absorption cross sections for water vapor from 183 to 193 nm, Geophys. Res. Lett., 24, 2195–2198, https://doi.org/10.1029/97GL02100, 1997.

Carslaw, N., Creasey, D. J., Heard, D. E., Lewis, A. C., McQuaid, J. B., Pilling, M. J., Monks, P. S., Bandy, B. J., and Penkett, S. A.: Modeling OH, HO_2, and RO_2 radicals in the marine boundary layer: 1. Model construction and comparison with field measurements, J. Geophys. Res., 104, 30241–30255, https://doi.org/10.1029/1999JD900783, 1999.

Chan, C. Y., Hard, T. M., Mehrabzadeh, A. A., George, L. A., and O’Brien, R. J.: Third-generation FAGE instrument for tropospheric hydroxyl radical measurement, J. Geophys. Res., 95, 18569, https://doi.org/10.1029/JD095iD11p18569, 1990.

Chen, L., Huang, Y., Xue, Y., Jia, Z., and Wang, W.: OH-initiated atmospheric degradation of hydroxyalkyl hydroperoxides: mechanism, kinetics, and structure–activity relationship, Atmospheric Chemistry and Physics, 22, 3693–3711, https://doi.org/10.5194/acp-22-3693-2022, 2022a.

Chen, Q., Xia, M., Peng, X., Yu, C., Sun, P., Li, Y., Liu, Y., Xu, Z., Xu, Z., Wu, R., Nie, W., Ding, A., Zhao, Y., and Wang, T.: Large Daytime Molecular Chlorine Missing Source at a Suburban Site in East China, JGR Atmospheres, 127, https://doi.org/10.1029/2021JD035796, 2022b.

Chen, S., Ren, X., Mao, J., Chen, Z., Brune, W. H., Lefer, B., Rappenglück, B., Flynn, J., Olson, J., and Crawford, J. H.: A comparison of chemical mechanisms based on TRAMP-2006 field data, Atmospheric Environment, 44, 4116–4125, https://doi.org/10.1016/j.atmosenv.2009.05.027, 2010.

Creasey, D. J., Evans, G. E., and Heard, D. E.: Measurements of OH and HO_2 concentrations in the Southern Ocean marine boundary layer, J. Geophys. Res., 108, 4475, https://doi.org/10.1029/2002JD003206, 2003.

Dubey, M. K., Hanisco, T. F., Wennberg, P. O., and Anderson, J. G.: Monitoring potential photochemical interference in laser-induced fluorescence Measurements of atmospheric OH, Geophys. Res. Lett., 23, 3215–3218, https://doi.org/10.1029/96GL03008, 1996.

Dusanter, S., Vimal, D., Stevens, P. S., Volkamer, R., and Molina, L. T.: Measurements of OH and HO_2 concentrations during the MCMA-2006 field campaign – Part 1: Deployment of the Indiana University laser-induced fluorescence instrument, Atmospheric Chemistry and Physics, 9, 1665–1685, https://doi.org/10.5194/acp-9-1665-2009, 2009a.

Dusanter, S., Vimal, D., Stevens, P. S., Volkamer, R., Molina, L. T., Baker, A., Meinardi, S., Blake, D., Sheehy, P., Merten, A., Zhang, R., Zheng, J., Fortner, E. C., Junkermann, W., Dubey, M., Rahn, T., Eichinger, B., Lewandowski, P., Prueger, J., and Holder, H.: Measurements of OH and HO_2 concentrations during the MCMA-2006 field campaign – Part 2: Model comparison and radical budget, Atmospheric Chemistry and Physics, 9, 6655–6675, https://doi.org/10.5194/acp-9-6655-2009, 2009b.

Edwards, G. D., Cantrell, C. A., Stephens, S., Hill, B., Goyea, O., Shetter, R. E., Mauldin, R. L., Kosciuch, E., Tanner, D. J., and Eisele, F. L.: Chemical Ionization Mass Spectrometer Instrument for the Measurement of Tropospheric HO_2 and RO_2, Anal. Chem., 75, 5317–5327, https://doi.org/10.1021/ac034402b, 2003.

Eisele, F. L. and Tanner, D. J.: Ion-assisted tropospheric OH measurements, J. Geophys. Res., 96, 9295, https://doi.org/10.1029/91JD00198, 1991.

Eisele, F. L. and Tanner, D. J.: Measurement of the gas phase concentration of H_2SO_4 and methane sulfonic acid and estimates of H_2SO_4 production and loss in the atmosphere, Journal of Geophysical Research: Atmospheres, 98, 9001–9010, https://doi.org/10.1029/93JD00031, 1993.

Emmerson, K. M., Carslaw, N., Carslaw, D. C., Lee, J. D., McFiggans, G., Bloss, W. J., Gravestock, T., Heard, D. E., Hopkins, J., Ingham, T., Pilling, M. J., Smith, S. C., Jacob, M., and Monks, P. S.: Free radical modelling studies during the UK TORCH

Campaign in Summer 2003, Atmospheric Chemistry and Physics, 7, 167–181, https://doi.org/10.5194/acp-7-167-2007, 2007.

Faloona, I. C., Tan, D., Lesher, R. L., Hazen, N. L., Frame, C. L., Simpas, J. B., Harder, H., Martinez, M., Di Carlo, P., Ren, X., and Brune, W. H.: A Laser-induced Fluorescence Instrument for Detecting Tropospheric OH and HO_2 : Characteristics and Calibration, Journal of Atmospheric Chemistry, 47, 139–167, https://doi.org/10.1023/B:JOCH.0000021036.53185.0e, 2004.

Fehsenfeld, F. C., Howard, C. J., and Schmeltekopf, A. L.: Gas phase ion chemistry of HNO_3, J. Chem. Phys., 63, 2835–2841, https://doi.org/10.1063/1.431722, 1975.

Feiner, P. A., Brune, W. H., Miller, D. O., Zhang, L., Cohen, R. C., Romer, P. S., Goldstein, A. H., Keutsch, F. N., Skog, K. M., Wennberg, P. O., Nguyen, T. B., Teng, A. P., DeGouw, J., Koss, A., Wild, R. J., Brown, S. S., Guenther, A., Edgerton, E., Baumann, K., and Fry, J. L.: Testing Atmospheric Oxidation in an Alabama Forest, Journal of the Atmospheric Sciences, 73, 4699–4710, https://doi.org/10.1175/JAS-D-16-0044.1, 2016.

Fittschen, C., Al Ajami, M., Batut, S., Ferracci, V., Archer-Nicholls, S., Archibald, A. T., and Schoemaecker, C.: ROOOH: a missing piece of the puzzle for OH measurements in low-NO environments?, Atmos. Chem. Phys., 19, 349–362, https://doi.org/10.5194/acp-19-349-2019, 2019.

Fu, X., Wang, T., Zhang, L., Li, Q., Wang, Z., Xia, M., Yun, H., Wang, W., Yu, C., Yue, D., Zhou, Y., Zheng, J., and Han, R.: The significant contribution of HONO to secondary pollutants during a severe winter pollution event in southern China, Atmos. Chem. Phys., 19, 1–14, https://doi.org/10.5194/acp-19-1-2019, 2019.

Fuchs, H., Brauers, T., Dorn, H.-P., Harder, H., Häseler, R., Hofzumahaus, A., Holland, F., Kanaya, Y., Kajii, Y., Kubistin, D., Lou, S., Martinez, M., Miyamoto, K., Nishida, S., Rudolf, M., Schlosser, E., Wahner, A., Yoshino, A., and Schurath, U.: Technical Note: Formal blind intercomparison of HO_2 measurements in the atmosphere simulation chamber SAPHIR during the HOxComp campaign, Atmospheric Chemistry and Physics, 10, 12233–12250, https://doi.org/10.5194/acp-10-12233-2010, 2010.

Fuchs, H., Bohn, B., Hofzumahaus, A., Holland, F., Lu, K. D., Nehr, S., Rohrer, F., and Wahner, A.: Detection of HO_2 by laser-induced fluorescence: calibration and interferences from RO_2 radicals, Atmospheric Measurement Techniques, 4, 1209–1225, https://doi.org/10.5194/amt-4-1209-2011, 2011.

Fuchs, H., Dorn, H.-P., Bachner, M., Bohn, B., Brauers, T., Gomm, S., Hofzumahaus, A., Holland, F., Nehr, S., Rohrer, F., Tillmann, R., and Wahner, A.: Comparison of OH concentration measurements by DOAS and LIF during SAPHIR chamber experiments at high OH reactivity and low NO concentration, Atmos. Meas. Tech., 5, 1611–1626, https://doi.org/10.5194/amt-5-1611-2012, 2012.

Fuchs, H., Hofzumahaus, A., Rohrer, F., Bohn, B., Brauers, T., Dorn, H.-P., Häseler, R., Holland, F., Kaminski, M., Li, X., Lu, K., Nehr, S., Tillmann, R., Wegener, R., and Wahner, A.: Experimental evidence for efficient hydroxyl radical regeneration in isoprene oxidation, Nature Geosci, 6, 1023–1026, https://doi.org/10.1038/ngeo1964, 2013.

Fuchs, H., Acir, I.-H., Bohn, B., Brauers, T., Dorn, H.-P., Häseler, R., Hofzumahaus, A., Holland, F., Kaminski, M., Li, X., Lu, K., Lutz, A., Nehr, S., Rohrer, F., Tillmann, R., Wegener, R., and Wahner, A.: OH regeneration from methacrolein oxidation investigated in the atmosphere simulation chamber SAPHIR, Atmos. Chem. Phys., 14, 7895–7908, https://doi.org/10.5194/acp-14-7895-2014, 2014.

Fuchs, H., Tan, Z., Hofzumahaus, A., Broch, S., Dorn, H.-P., Holland, F., Künstler, C., Gomm, S., Rohrer, F., Schrade, S., Tillmann, R., and Wahner, A.: Investigation of potential interferences in the detection of atmospheric RO_x radicals by laser-induced fluorescence under dark conditions, Atmospheric Measurement Techniques, 9, 1431–1447, https://doi.org/10.5194/amt-9-1431-2016, 2016.

Fuchs, H., Albrecht, S., Acir, I., Bohn, B., Breitenlechner, M., Dorn, H.-P., Gkatzelis, G. I., Hofzumahaus, A., Holland, F., Kaminski, M., Keutsch, F. N., Novelli, A., Reimer, D., Rohrer, F., Tillmann, R., Vereecken, L., Wegener, R., Zaytsev, A., Kiendler-Scharr, A., and Wahner, A.: Investigation of the oxidation of methyl vinyl ketone (MVK) by OH radicals in the atmospheric simulation chamber SAPHIR, Atmos. Chem. Phys., 18, 8001–8016, https://doi.org/10.5194/acp-18-8001-2018, 2018.

Griffith, S. M., Hansen, R. F., Dusanter, S., Stevens, P. S., Alaghmand, M., Bertman, S. B., Carroll, M. A., Erickson, M., Galloway, M., Grossberg, N., Hottle, J., Hou, J., Jobson, B. T., Kammrath, A., Keutsch, F. N., Lefer, B. L., Mielke, L. H., O'Brien, A., Shepson, P. B., Thurlow, M., Wallace, W., Zhang, N., and Zhou, X. L.: OH and HO_2 radical chemistry during PROPHET 2008 and CABINEX 2009 - Part 1: Measurements and model comparison, Atmospheric Chemistry and Physics, 13, 5403–5423, https://doi.org/10.5194/acp-13-5403-2013, 2013.

Griffith, S. M., Hansen, R. F., Dusanter, S., Michoud, V., Gilman, J. B., Kuster, W. C., Veres, P. R., Graus, M., Gouw, J. A., Roberts, J., Young, C., Washenfelder, R., Brown, S. S., Thalman, R., Waxman, E., Volkamer, R., Tsai, C., Stutz, J., Flynn, J. H., Grossberg, N., Lefer, B., Alvarez, S. L., Rappenglueck, B., Mielke, L. H., Osthoff, H. D., and Stevens, P. S.: Measurements of hydroxyl and hydroperoxy radicals during CalNex-LA: Model comparisons and radical budgets, J. Geophys. Res. Atmos., 121, 4211–4232, https://doi.org/10.1002/2015JD024358, 2016.

Guo, J., Wang, Z., Tao Wang, and Zhang, X.: Theoretical evaluation of different factors affecting the HO_2 uptake coefficient driven by aqueous-phase first-order loss reaction, Science of The Total Environment, 683, 146–153, https://doi.org/10.1016/j.scitotenv.2019.05.237, 2019.

Guo, Y., Yan, C., Li, C., Ma, W., Feng, Z., Zhou, Y., Lin, Z., Dada, L., Stolzenburg, D., Yin, R., Kontkanen, J., Daellenbach, K. R., Kangasluoma, J., Yao, L., Chu, B., Wang, Y., Cai, R., Bianchi, F., Liu, Y., and Kulmala, M.: Formation of nighttime sulfuric acid from the ozonolysis of alkenes in Beijing, Atmos. Chem. Phys., 21, 5499–5511, https://doi.org/10.5194/acp-21-5499-2021, 2021.

Handisides, G. M.: Hohenpeissenberg Photochemical Experiment (HOPE 2000): Measurements and photostationary state calculations of OH and peroxy radicals, Atmos. Chem. Phys., 24, 2003.

Hanke, M., Uecker, J., Reiner, T., and Arnold, F.: Atmospheric peroxy radicals: ROXMAS, a new mass-spectrometric methodology for speciated measurements of HO_2 and $\sum RO_2$ and first results, International Journal of Mass Spectrometry, 213, 91–99, https://doi.org/10.1016/S1387-3806(01)00548-6, 2002.

Hansen, R. F., Griffith, S. M., Dusanter, S., Rickly, P. S., Stevens, P. S., Bertman, S. B., Carroll, M. A., Erickson, M. H., Flynn, J. H., Grossberg, N., Jobson, B. T., Lefer, B. L., and Wallace, H. W.: Measurements of total hydroxyl radical reactivity during CABINEX 2009 – Part 1: field measurements, Atmos. Chem. Phys., 14, 2923–2937, https://doi.org/10.5194/acp-14-2923-2014, 2014.

Hard, T. M., O'Brien, R. J., Cook, T. B., and Tsongas, G. A.: Interference suppression in HO fluorescence detection, Appl. Opt., 18, 3216, https://doi.org/10.1364/AO.18.003216, 1979.

Hard, T. M., O'Brien, R. J., Chan, C. Y., and Mehrabzadeh, A. A.: Tropospheric free radical determination by fluorescence assay with gas expansion, Environ. Sci. Technol., 18, 768–777, https://doi.org/10.1021/es00128a009, 1984.

Heard, D. E. and Pilling, M. J.: Measurement of OH and HO_2 in the Troposphere, Chem. Rev., 103, 5163–5198, https://doi.org/10.1021/cr020522s, 2003.

Hens, K., Novelli, A., Martinez, M., Auld, J., Axinte, R., Bohn, B., Fischer, H., Keronen, P., Kubistin, D., Nölscher, A. C., Oswald, R., Paasonen, P., Petäjä, T., Regelin, E., Sander, R., Sinha, V., Sipilä, M., Taraborrelli, D., Tatum Ernest, C., Williams, J., Lelieveld, J., and Harder, H.: Observation and modelling of HO_x radicals in a boreal forest, Atmospheric Chemistry and Physics, 14, 8723–8747, https://doi.org/10.5194/acp-14-8723-2014, 2014.

Hofzumahaus, A. and Holland, F.: Laser-induced fluorescence based detection system for measurement of tropospheric OH using 308 nm excitation at low pressure, 163–173, https://doi.org/10.1117/12.140228, 1993.

Hofzumahaus, A., Rohrer, F., Lu, K., Bohn, B., Brauers, T., Chang, C.-C., Fuchs, H., Holland, F., Kita, K., Kondo, Y., Li, X., Lou, S., Shao, M., Zeng, L., Wahner, A., and Zhang, Y.: Amplified Trace Gas Removal in the Troposphere, Science, 324, 1702–1704, https://doi.org/10.1126/science.1164566, 2009.

Holland, F., Hofzumahaus, A., Schäfer, J., and Kraus, A.: Measurements of OH and HO_2 radical concentrations and photolysis frequencies during BERLIOZ, J. Geophys. Res., 108, 8246, https://doi.org/10.1029/2001JD001393, 2003.

Hübler, G., Perner, D., Platt, U., Tönnissen, A., and Ehhalt, D. H.: Groundlevel OH radical concentration: New measurements by optical absorption, J. Geophys. Res., 89, 1309, https://doi.org/10.1029/JD089iD01p01309, 1984.

Ivanov, A. V., Gershenzon, Y. M., Gratpanche, F., Devolder, P., and Sawerysyn, J.-P.: Heterogeneous loss of OH on NaCl and NH_4NO_3 at tropospheric temperatures, Annales Geophysicae, 14, 659–664, https://doi.org/10.1007/s00585-996-0659-5, 1996.

Jacob, D.: Heterogeneous chemistry and tropospheric ozone, Atmospheric Environment, 34, 2131–2159, https://doi.org/10.1016/S1352-2310(99)00462-8, 2000.

Jenkin, M. E., Young, J. C., and Rickard, A. R.: The MCM v3.3.1 degradation scheme for isoprene, Atmos. Chem. Phys., 15, 11433–11459, https://doi.org/10.5194/acp-15-11433-2015, 2015.

Jeong, D., Seco, R., Emmons, L., Schwantes, R., Liu, Y., McKinney, K. A., Martin, S. T., Keutsch, F. N., Gu, D., Guenther, A. B., Vega, O., Tota, J., Souza, R. A. F., Springston, S. R., Watson, T. B., and Kim, S.: Reconciling Observed and Predicted Tropical Rainforest OH Concentrations, JGR Atmospheres, 127, https://doi.org/10.1029/2020JD032901, 2022.

Kaiser, J., Skog, K. M., Baumann, K., Bertman, S. B., Brown, S. B., Brune, W. H., Crounse, J. D., de Gouw, J. A., Edgerton, E. S., Feiner, P. A., Goldstein, A. H., Koss, A., Misztal, P. K., Nguyen, T. B., Olson, K. F., St. Clair, J. M., Teng, A. P., Toma, S., Wennberg, P. O., Wild, R. J., Zhang, L., and Keutsch, F. N.: Speciation of OH reactivity above the canopy of an isoprene-dominated forest, Atmos. Chem. Phys., 16, 9349–9359, https://doi.org/10.5194/acp-16-9349-2016, 2016.

Kaminski, M., Fuchs, H., Acir, I.-H., Bohn, B., Brauers, T., Dorn, H.-P., Häseler, R., Hofzumahaus, A., Li, X., Lutz, A., Nehr, S., Rohrer, F., Tillmann, R., Vereecken, L., Wegener, R., and Wahner, A.: Investigation of the β-pinene photooxidation by OH in the atmosphere simulation chamber SAPHIR, Atmospheric Chemistry and Physics, 17, 6631–6650, https://doi.org/10.5194/acp-17-6631-2017, 2017.

Kanaya, Y., Cao, R., Kato, S., Miyakawa, Y., Kajii, Y., Tanimoto, H., Yokouchi, Y., Mochida, M., Kawamura, K., and Akimoto, H.: Chemistry of OH and HO_2 radicals observed at Rishiri Island, Japan, in September 2003: Missing daytime sink of HO_2 and positive nighttime correlations with monoterpenes, J. Geophys. Res., 112, D11308, https://doi.org/10.1029/2006JD007987, 2007a.

Kanaya, Y., Cao, R., Akimoto, H., Fukuda, M., Komazaki, Y., Yokouchi, Y., Koike, M., Tanimoto, H., Takegawa, N., and Kondo, Y.: Urban photochemistry in central Tokyo: 1. Observed and modeled OH and HO_2 radical concentrations during the winter and summer of 2004, J. Geophys. Res., 112, D21312, https://doi.org/10.1029/2007JD008670, 2007b.

Kanaya, Y., Hofzumahaus, A., Dorn, H.-P., Brauers, T., Fuchs, H., Holland, F., Rohrer, F., Bohn, B., Tillmann, R., Wegener, R., Wahner, A., Kajii, Y., Miyamoto, K., Nishida, S., Watanabe, K., Yoshino, A., Kubistin, D., Martinez, M., Rudolf, M., Harder, H., Berresheim, H., Elste, T., Plass-Dülmer, C., Stange, G., Kleffmann, J., Elshorbany, Y., and Schurath, U.: Comparisons of observed and modeled OH and HO_2 concentrations during the ambient measurement period of the HO_xComp field campaign, Atmospheric Chemistry and Physics, 12, 2567–2585, https://doi.org/10.5194/acp-12-2567-2012, 2012.

Kim, S., Wolfe, G. M., Mauldin, L., Cantrell, C., Guenther, A., Karl, T., Turnipseed, A., Greenberg, J., Hall, S. R., Ullmann, K., Apel, E., Hornbrook, R., Kajii, Y., Nakashima, Y., Keutsch, F. N., DiGangi, J. P., Henry, S. B., Kaser, L., Schnitzhofer, R., Graus, M., Hansel, A., Zheng, W., and Flocke, F. F.: Evaluation of HO_x sources and cycling using measurement-constrained model calculations in a 2-methyl-3-butene-2-ol (MBO) and monoterpene (MT) dominated ecosystem, Atmospheric Chemistry and Physics, 13, 2031–2044, https://doi.org/10.5194/acp-13-2031-2013, 2013.

Kohno, N., Zhou, J., Li, J., Takemura, M., Ono, N., Sadanaga, Y., Nakashima, Y., Sato, K., Kato, S., Sakamoto, Y., and Kajii, Y.: Impacts of missing OH reactivity and aerosol uptake of HO_2 radicals on tropospheric O_3 production during the AQUAS-Kyoto summer campaign in 2018, Atmospheric Environment, 281, 119130, https://doi.org/10.1016/j.atmosenv.2022.119130, 2022.

Konrad, S.: Hydrocarbon measurements at Pabstthum during the BERLIOZ campaign and modeling of free radicals, J. Geophys. Res., 108, 8251, https://doi.org/10.1029/2001JD000866, 2003.

Kukui, A., Ancellet, G., and Le Bras, G.: Chemical ionisation mass spectrometer for measurements of OH and Peroxy radical concentrations in moderately polluted atmospheres, J Atmos Chem, 61, 133–154, https://doi.org/10.1007/s10874-009-9130-9, 2008.

Kukui, A., Legrand, M., Ancellet, G., Gros, V., Bekki, S., Sarda-Estève, R., Loisil, R., and Preunkert, S.: Measurements of OH and RO_2 radicals at the coastal Antarctic site of Dumont d'Urville (East Antarctica) in summer 2010–2011, Journal of Geophysical Research: Atmospheres, 117, https://doi.org/10.1029/2012JD017614, 2012.

Kukui, A., Legrand, M., Preunkert, S., Frey, M. M., Loisil, R., Gil Roca, J., Jourdain, B., King, M. D., France, J. L., and Ancellet, G.: Measurements of OH and RO_2 radicals at Dome C, East Antarctica, Atmospheric Chemistry and Physics, 14, 12373–12392, https://doi.org/10.5194/acp-14-12373-2014, 2014.

Kulmala, M., Vehkamäki, H., Petäjä, T., Dal Maso, M., Lauri, A., Kerminen, V.-M., Birmili, W., and McMurry, P. H.: Formation and growth rates of ultrafine atmospheric particles: a review of observations, Journal of Aerosol Science, 35, 143–176, https://doi.org/10.1016/j.jaerosci.2003.10.003, 2004.

Kürten, A., Rondo, L., Ehrhart, S., and Curtius, J.: Calibration of a Chemical Ionization Mass Spectrometer for the Measurement of Gaseous Sulfuric Acid, J. Phys. Chem. A, 116, 6375–6386, https://doi.org/10.1021/jp212123n, 2012.

Kuyper, B., Wingrove, H., Lesch, T., Labuschagne, C., Say, D., Martin, D., Young, D., Khan, M. A. H., O'Doherty, S., Davies-Coleman, M. T., and Shallcross, D. E.: Atmospheric Toluene and Benzene Mole Fractions at Cape Town and Cape Point and an Estimation of the Hydroxyl Radical Concentrations in the Air above the Cape Peninsula, South Africa, ACS Earth Space Chem., 4, 24–34, https://doi.org/10.1021/acsearthspacechem.9b00207, 2020.

Lelieveld, J., Butler, T. M., Crowley, J. N., Dillon, T. J., Fischer, H., Ganzeveld, L., Harder, H., Lawrence, M. G., Martinez, M., Taraborrelli, D., and Williams, J.: Atmospheric oxidation capacity sustained by a tropical forest, Nature, 452, 737–740, https://doi.org/10.1038/nature06870, 2008.

Levy, H.: Normal Atmosphere: Large Radical and Formaldehyde Concentrations Predicted, Science, 173, 141–143, https://doi.org/10.1126/science.173.3992.141, 1971.

Lew, M. M., Rickly, P. S., Bottorff, B. P., Reidy, E., Sklaveniti, S., Léonardis, T., Locoge, N., Dusanter, S., Kundu, S., Wood, E., and Stevens, P. S.: OH and HO_2 radical chemistry in a midlatitude forest: measurements and model comparisons, Atmospheric Chemistry and Physics, 20, 9209–9230, https://doi.org/10.5194/acp-20-9209-2020, 2020.

Li, J., Sakamoto, Y., Kohno, N., Fujii, T., Matsuoka, K., Takemura, M., Zhou, J., Nakagawa, M., Murano, K., Sadanaga, Y., Nakashima, Y., Sato, K., Takami, A., Yoshino, A., Nakayama, T., Kato, S., and Kajii, Y.: Total hydroxyl radical reactivity measurements in a suburban area during AQUAS–Tsukuba campaign in summer 2017, Science of The Total Environment, 740, 139897, https://doi.org/10.1016/j.scitotenv.2020.139897, 2020.

Li, J., Kohno, N., Sakamoto, Y., Fukusaki, Y., Kousa, Y., Sadanaga, Y., Nakashima, Y., Sato, K., Ramasamy, S., Takami, A., Yoshino, A., Nakayama, T., Kato, S., Ono, N., Zhou, J., Bai, Y., and Kajii, Y.: A quantitative understanding of total OH reactivity and ozone production in a coastal industrial area during the Yokohama air quality study (AQUAS) campaign of summer 2019, Atmospheric Environment, 267, 118754, https://doi.org/10.1016/j.atmosenv.2021.118754, 2021.

Li, Z., Xue, L., Yang, X., Zha, Q., Tham, Y. J., Yan, C., Louie, P. K. K., Luk, C. W. Y., Wang, T., and Wang, W.: Oxidizing capacity of the rural atmosphere in Hong Kong, Southern China, Science of The Total Environment, 612, 1114–1122, https://doi.org/10.1016/j.scitotenv.2017.08.310, 2018.

Liao, J., Huey, L. G., Tanner, D. J., Brough, N., Brooks, S., Dibb, J. E., Stutz, J., Thomas, J. L., Lefer, B., Haman, C., and Gorham, K.: Observations of hydroxyl and peroxy radicals and the impact of BrO at Summit, Greenland in 2007 and 2008, Atmos. Chem. Phys., 11, 8577–8591, https://doi.org/10.5194/acp-11-8577-2011, 2011.

Lu, K., Guo, S., Tan, Z., Wang, H., Shang, D., Liu, Y., Li, X., Wu, Z., Hu, M., and Zhang, Y.: Exploring atmospheric free-radical chemistry in China: the self-cleansing capacity and the formation of secondary air pollution, National Science Review, 6, 579–594, https://doi.org/10.1093/nsr/nwy073, 2019.

Lu, K. D., Rohrer, F., Holland, F., Fuchs, H., Bohn, B., Brauers, T., Chang, C. C., Häseler, R., Hu, M., Kita, K., Kondo, Y., Li, X., Lou, S. R., Nehr, S., Shao, M., Zeng, L. M., Wahner, A., Zhang, Y. H., and Hofzumahaus, A.: Observation and modelling of OH and HO_2 concentrations in the Pearl River Delta 2006: a missing OH source in a VOC rich atmosphere, Atmospheric Chemistry and Physics, 12, 1541–1569, https://doi.org/10.5194/acp-12-1541-2012, 2012.

Lu, K. D., Hofzumahaus, A., Holland, F., Bohn, B., Brauers, T., Fuchs, H., Hu, M., Häseler, R., Kita, K., Kondo, Y., Li, X., Lou, S. R., Oebel, A., Shao, M., Zeng, L. M., Wahner, A., Zhu, T., Zhang, Y. H., and Rohrer, F.: Missing OH source in a suburban environment near Beijing: observed and modelled OH and HO_2 concentrations in summer 2006, Atmospheric Chemistry and Physics, 13, 1057–1080, https://doi.org/10.5194/acp-13-1057-2013, 2013a.

Lu, Q., Zheng, J., Ye, S., Shen, X., Yuan, Z., and Yin, S.: Emission trends and source characteristics of SO_2, NO_x, PM_{10} and VOCs in the Pearl River Delta region from 2000 to 2009, Atmospheric Environment, 76, 11–20, https://doi.org/10.1016/j.atmosenv.2012.10.062, 2013b.

Ma, X., Tan, Z., Lu, K., Yang, X., Liu, Y., Li, S., Li, X., Chen, S., Novelli, A., Cho, C., Zeng, L., Wahner, A., and Zhang, Y.: Winter photochemistry in Beijing: Observation and model simulation of OH and HO2 radicals at an urban site, Science of The Total Environment, 685, 85–95, https://doi.org/10.1016/j.scitotenv.2019.05.329, 2019.

Ma, X., Tan, Z., Lu, K., Yang, X., Chen, X., Wang, H., Chen, S., Fang, X., Li, S., Li, X., Liu, J., Liu, Y., Lou, S., Qiu, W., Wang, H., Zeng, L., and Zhang, Y.: OH and HO_2 radical chemistry at a suburban site during the EXPLORE-YRD campaign in 2018, Atmospheric Chemistry and Physics, 22, 7005–7028, https://doi.org/10.5194/acp-22-7005-2022, 2022.

Mao, J., Ren, X., Chen, S., Brune, W. H., Chen, Z., Martinez, M., Harder, H., Lefer, B., Rappenglück, B., Flynn, J., and Leuchner, M.: Atmospheric oxidation capacity in the summer of Houston 2006: Comparison with summer measurements in other metropolitan studies, Atmospheric Environment, 44, 4107–4115, https://doi.org/10.1016/j.atmosenv.2009.01.013, 2010.

Mao, J., Ren, X., Zhang, L., Van Duin, D. M., Cohen, R. C., Park, J.-H., Goldstein, A. H., Paulot, F., Beaver, M. R., Crounse, J. D., Wennberg, P. O., DiGangi, J. P., Henry, S. B., Keutsch, F. N., Park, C., Schade, G. W., Wolfe, G. M., Thornton, J. A., and Brune, W. H.: Insights into hydroxyl measurements and atmospheric oxidation in a California forest, Atmos. Chem. Phys., 12, 8009–8020, https://doi.org/10.5194/acp-12-8009-2012, 2012.

Marno, D., Ernest, C., Hens, K., Javed, U., Klimach, T., Martinez, M., Rudolf, M., Lelieveld, J., and Harder, H.: Calibration of an airborne HO_x instrument using the All Pressure Altitude-based Calibrator for HO_x Experimentation (APACHE), Atmospheric Measurement Techniques, 13, 2711–2731, https://doi.org/10.5194/amt-13-2711-2020, 2020.

Mauldin III, R., Kosciuch, E., Eisele, F., Huey, G., Tanner, D., Sjostedt, S., Blake, D., Chen, G., Crawford, J., and Davis, D.: South Pole Antarctica observations and modeling results: New insights on HO_x radical and sulfur chemistry, Atmospheric Environment, 44, 572–581, https://doi.org/10.1016/j.atmosenv.2009.07.058, 2010.

Mauldin III, R. L., Eisele, F. L., Cantrell, C. A., Kosciuch, E., Ridley, B. A., Lefer, B., Tanner, D. J., Nowak, J. B., Chen, G., Wang, L., and Davis, D.: Measurements of OH aboard the NASA P-3 during PEM-Tropics B, J. Geophys. Res., 106, 32657–32666, https://doi.org/10.1029/2000JD900832, 2001a.

Mauldin III, R. L., Eisele, F. L., Tanner, D. J., Kosciuch, E., Shetter, R., Lefer, B., Hall, S. R., Nowak, J. B., Buhr, M., Chen, G., Wang, P., and Davis, D.: Measurements of OH, H_2SO_4, and MSA at the South Pole during ISCAT, Geophysical Research Letters, 28, 3629–3632, https://doi.org/10.1029/2000GL012711, 2001b.

Mauldin III, R. L., Kosciuch, E., Henry, B., Eisele, F. L., Shetter, R., Lefer, B., Chen, G., Davis, D., Huey, G., and Tanner, D.: Measurements of OH, HO_2+RO_2, H_2SO_4, and MSA at the South Pole during ISCAT 2000, Atmospheric Environment, 38, 5423–5437, https://doi.org/10.1016/j.atmosenv.2004.06.031, 2004.

Mauldin III, R. L., Berndt, T., Sipilä, M., Paasonen, P., Petäjä, T., Kim, S., Kurtén, T., Stratmann, F., Kerminen, V.-M., and Kulmala, M.: A new atmospherically relevant oxidant of sulphur dioxide, Nature, 488, 193–196, https://doi.org/10.1038/nature11278, 2012.

Mauldin, R. L., Frost, G. J., Chen, G., Tanner, D. J., Prevot, A. S. H., Davis, D. D., and Eisele, F. L.: OH measurements during the First Aerosol Characterization Experiment (ACE 1): Observations and model comparisons, J. Geophys. Res., 103, 16713–16729, https://doi.org/10.1029/98JD00882, 1998.

McKeen, S. A., Mount, G., Eisele, F., Williams, E., Harder, J., Goldan, P., Kuster, W., Liu, S. C., Baumann, K., Tanner, D., Fried, A., Sewell, S., Cantrell, C., and Shetter, R.: Photochemical modeling of hydroxyl and its relationship to other species during the Tropospheric OH Photochemistry Experiment, J. Geophys. Res., 102, 6467–6493, https://doi.org/10.1029/96JD03322, 1997.

Nie, W., Yan, C., Huang, D. D., Wang, Z., Liu, Y., Qiao, X., Guo, Y., Tian, L., Zheng, P., Xu, Z., Li, Y., Xu, Z., Qi, X., Sun, P., Wang, J., Zheng, F., Li, X., Yin, R., Dallenbach, K. R., Bianchi, F., Petäjä, T., Zhang, Y., Wang, M., Schervish, M., Wang, S., Qiao, L., Wang, Q., Zhou, M., Wang, H., Yu, C., Yao, D., Guo, H., Ye, P., Lee, S., Li, Y. J., Liu, Y., Chi, X., Kerminen, V.-M., Ehn, M., Donahue, N. M., Wang, T., Huang, C., Kulmala, M., Worsnop, D., Jiang, J., and Ding, A.: Secondary organic aerosol formed by condensing anthropogenic vapours over China's megacities, Nat. Geosci., 15, 255–261, https://doi.org/10.1038/s41561-022-00922-5, 2022.

Novelli, A., Hens, K., Tatum Ernest, C., Kubistin, D., Regelin, E., Elste, T., Plass-Dülmer, C., Martinez, M., Lelieveld, J., and Harder, H.: Characterisation of an inlet pre-injector laser-induced fluorescence instrument for the measurement of atmospheric hydroxyl radicals, Atmos. Meas. Tech., 7, 3413–3430, https://doi.org/10.5194/amt-7-3413-2014, 2014.

Novelli, A., Vereecken, L., Bohn, B., Dorn, H.-P., Gkatzelis, G. I., Hofzumahaus, A., Holland, F., Reimer, D., Rohrer, F., Rosanka, S., Taraborrelli, D., Tillmann, R., Wegener, R., Yu, Z., Kiendler-Scharr, A., Wahner, A., and Fuchs, H.: Importance of isomerization reactions for OH radical regeneration from the photo-oxidation of isoprene investigated in the atmospheric simulation chamber SAPHIR, Atmos. Chem. Phys., 20, 3333–3355, https://doi.org/10.5194/acp-20-3333-2020, 2020.

Nussbaumer, C. M., Crowley, J. N., Schuladen, J., Williams, J., Hafermann, S., Reiffs, A., Axinte, R., Harder, H., Ernest, C., Novelli, A., Sala, K., Martinez, M., Mallik, C., Tomsche, L., Plass-Dülmer, C., Bohn, B., Lelieveld, J., and Fischer, H.: Measurement report: Photochemical production and loss rates of formaldehyde and ozone across Europe, Atmospheric Chemistry and Physics, 21, 18413–18432, https://doi.org/10.5194/acp-21-18413-2021, 2021.

Pang, J. Y. S., Novelli, A., Kaminski, M., Acir, I.-H., Bohn, B., Carlsson, P. T. M., Cho, C., Dorn, H.-P., Hofzumahaus, A., Li, X., Lutz, A., Nehr, S., Reimer, D., Rohrer, F., Tillmann, R., Wegener, R., Kiendler-Scharr, A., Wahner, A., and Fuchs, H.: Investigation of the limonene photooxidation by OH at different NO concentrations in the atmospheric simulation chamber SAPHIR (Simulation of Atmospheric PHotochemistry In a large Reaction Chamber), Atmos. Chem. Phys., 22, 8497–8527, https://doi.org/10.5194/acp-22-8497-2022, 2022.

Park, J.-H., Ivanov, A., and Molina, M.: Effect of Relative Humidity on OH Uptake by Surfaces of Atmospheric Importance, The journal of physical chemistry. A, 112, 6968–77, https://doi.org/10.1021/jp8012317, 2008.

Peeters, J. and Müller, J.-F.: HO_x radical regeneration in isoprene oxidation via peroxy radical isomerisations. II: experimental evidence and global impact, Phys. Chem. Chem. Phys., 12, 14227, https://doi.org/10.1039/c0cp00811g, 2010.

Peeters, J., Nguyen, T. L., and Vereecken, L.: HOx radical regeneration in the oxidation of isoprene, Phys. Chem. Chem. Phys., 11, 5935, https://doi.org/10.1039/b908511d, 2009.

Peeters, J., Müller, J.-F., Stavrakou, T., and Nguyen, V. S.: Hydroxyl Radical Recycling in Isoprene Oxidation Driven by Hydrogen Bonding and Hydrogen Tunneling: The Upgraded LIM1 Mechanism, J. Phys. Chem. A, 118, 8625–8643, https://doi.org/10.1021/jp5033146, 2014.

Peng, X., Wang, T., Wang, W., Ravishankara, A. R., George, C., Xia, M., Cai, M., Li, Q., Salvador, C. M., Lau, C., Lyu, X., Poon, C. N., Mellouki, A., Mu, Y., Hallquist, M., Saiz-Lopez, A., Guo, H., Herrmann, H., Yu, C., Dai, J., Wang, Y., Wang, X., Yu, A., Leung, K., Lee, S., and Chen, J.: Photodissociation of particulate nitrate as a source of daytime tropospheric Cl_2, Nat Commun, 13, 939, https://doi.org/10.1038/s41467-022-28383-9, 2022.

Perner, D., Ehhalt, D. H., Pätz, H. W., Platt, U., Röth, E. P., and Volz, A.: OH - Radicals in the lower troposphere, Geophys. Res. Lett., 3, 466–468, https://doi.org/10.1029/GL003i008p00466, 1976.

Petäjä, T., Mauldin, I. I. I., Kosciuch, E., McGrath, J., Nieminen, T., Paasonen, P., Boy, M., Adamov, A., Kotiaho, T., and Kulmala, M.: Sulfuric acid and OH concentrations in a boreal forest site, Atmospheric Chemistry and Physics, 9, 7435–7448, https://doi.org/10.5194/acp-9-7435-2009, 2009.

Platt, U., Rateike, M., Junkermann, W., Rudolph, J., and Ehhalt, D. H.: New tropospheric OH measurements, J. Geophys. Res., 93, 5159, https://doi.org/10.1029/JD093iD05p05159, 1988.

Pugh, T. A. M., MacKenzie, A. R., Hewitt, C. N., Langford, B., Edwards, P. M., Furneaux, K. L., Heard, D. E., Hopkins, J. R., Jones, C. E., Karunaharan, A., Lee, J., Mills, G., Misztal, P., Moller, S., Monks, P. S., and Whalley, L. K.: Simulating atmospheric composition over a South-East Asian tropical rainforest: performance of a chemistry box model, Atmos. Chem. Phys., 20, 2010.

Ramasamy, S., Ida, A., Jones, C., Kato, S., Tsurumaru, H., Kishimoto, I., Kawasaki, S., Sadanaga, Y., Nakashima, Y., Nakayama, T., Matsumi, Y., Mochida, M., Kagami, S., Deng, Y., Ogawa, S., Kawana, K., and Kajii, Y.: Total OH reactivity measurement in a BVOC dominated temperate forest during a summer campaign, 2014, Atmospheric Environment, 131, 41–54, https://doi.org/10.1016/j.atmosenv.2016.01.039, 2016.

Ren, X.: HO_x concentrations and OH reactivity observations in New York City during PMTACS-NY2001, Atmospheric Environment, 37, 3627–3637, https://doi.org/10.1016/S1352-2310(03)00460-6, 2003a.

Ren, X.: OH and HO_2 Chemistry in the urban atmosphere of New York City, Atmospheric Environment, 37, 3639–3651, https://doi.org/10.1016/S1352-2310(03)00459-X, 2003b.

Ren, X., Brune, W. H., Oliger, A., Metcalf, A. R., Simpas, J. B., Shirley, T., Schwab, J. J., Bai, C., Roychowdhury, U., Li, Y., Cai, C., Demerjian, K. L., He, Y., Zhou, X., Gao, H., and Hou, J.: OH, HO_2 , and OH reactivity during the PMTACS-NY Whiteface Mountain 2002 campaign: Observations and model comparison: HO_x DURING PMTACS-NY WHITEFACE 2002, J. Geophys. Res., 111, n/a-n/a, https://doi.org/10.1029/2005JD006126, 2006.

Ren, X., van Duin, D., Cazorla, M., Chen, S., Mao, J., Zhang, L., Brune, W. H., Flynn, J. H., Grossberg, N., Lefer, B. L., Rappenglück, B., Wong, K. W., Tsai, C., Stutz, J., Dibb, J. E., Thomas Jobson, B., Luke, W. T., and Kelley, P.: Atmospheric oxidation chemistry and ozone production: Results from SHARP 2009 in Houston, Texas: ATMOSPHERIC PHOTOCHEMISTRY IN HOUSTON, J. Geophys. Res. Atmos., 118, 5770–5780, https://doi.org/10.1002/jgrd.50342, 2013.

Rohrer, F. and Berresheim, H.: Strong correlation between levels of tropospheric hydroxyl radicals and solar ultraviolet radiation, Nature, 442, 184–187, https://doi.org/10.1038/nature04924, 2006.

Rohrer, F., Lu, K., Hofzumahaus, A., Bohn, B., Brauers, T., Chang, C.-C., Fuchs, H., Häseler, R., Holland, F., Hu, M., Kita, K., Kondo, Y., Li, X., Lou, S., Oebel, A., Shao, M., Zeng, L., Zhu, T., Zhang, Y., and Wahner, A.: Maximum efficiency in the hydroxyl-radical-based self-cleansing of the troposphere, Nature Geosci, 7, 559–563, https://doi.org/10.1038/ngeo2199, 2014.

Rolletter, M., Kaminski, M., Acir, I.-H., Bohn, B., Dorn, H.-P., Li, X., Lutz, A., Nehr, S., Rohrer, F., Tillmann, R., Wegener, R., Hofzumahaus, A., Kiendler-Scharr, A., Wahner, A., and Fuchs, H.: Investigation of the α-pinene photooxidation by OH in the atmospheric simulation chamber SAPHIR, Atmospheric Chemistry and Physics, 19, 11635–11649, https://doi.org/10.5194/acp-19-11635-2019, 2019.

Sanchez, J., Tanner, D. J., Chen, D., Huey, L. G., and Ng, N. L.: A new technique for the direct detection of HO_2 radicals using bromide chemical ionization mass spectrometry (Br-CIMS): initial characterization, Atmospheric Measurement Techniques, 9, 3851–3861, https://doi.org/10.5194/amt-9-3851-2016, 2016.

Schlosser, E., Brauers, T., Kanaya, Y., Kajii, Y., Miyamoto, K., Nishida, S., Watanabe, K., Yoshino, A., Kubistin, D., Martinez, M., Rudolf, M., Harder, H., Berresheim, H., and Elste, T.: Technical Note: Formal blind intercomparison of OH measurements: results from the international campaign HOxComp, Atmos. Chem. Phys., 26, 2009.

Shirley, T. R., Brune, W. H., Ren, X., Mao, J., Lesher, R., Cardenas, B., Volkamer, R., Molina, L. T., Molina, M. J., Lamb, B., Velasco, E., Jobson, T., and Alexander, M.: Atmospheric oxidation in the Mexico City Metropolitan Area (MCMA) during April 2003, Atmos. Chem. Phys., 13, 2006.

da Silva, G., Graham, C., and Wang, Z.-F.: Unimolecular β-Hydroxyperoxy Radical Decomposition with OH Recycling in the Photochemical Oxidation of Isoprene, Environ. Sci. Technol., 44, 250–256, https://doi.org/10.1021/es900924d, 2010.

Singh, H. B. and Hanst, P. L.: Peroxyacetyl nitrate (PAN) in the unpolluted atmosphere: An important reservoir for nitrogen oxides, Geophys. Res. Lett., 8, 941–944, https://doi.org/10.1029/GL008i008p00941, 1981.

Sjostedt, S. J., Huey, L. G., Tanner, D. J., Peischl, J., Chen, G., Dibb, J. E., Lefer, B., Hutterli, M. A., Beyersdorf, A. J., Blake, N. J., Blake, D. R., Sueper, D., Ryerson, T., Burkhart, J., and Stohl, A.: Observations of hydroxyl and the sum of peroxy radicals at Summit, Greenland during summer 2003, Atmospheric Environment, 41, 5122–5137, https://doi.org/10.1016/j.atmosenv.2006.06.065, 2007.

Slater, E. J., Whalley, L. K., Woodward-Massey, R., Ye, C., Lee, J. D., Squires, F., Hopkins, J. R., Dunmore, R. E., Shaw, M., Hamilton, J. F., Lewis, A. C., Crilley, L. R., Kramer, L., Bloss, W., Vu, T., Sun, Y., Xu, W., Yue, S., Ren, L., Acton, W. J. F., Hewitt, C. N., Wang, X., Fu, P., and Heard, D. E.: Elevated levels of OH observed in haze events during wintertime in central Beijing, Atmospheric Chemistry and Physics, 20, 14847–14871, https://doi.org/10.5194/acp-20-14847-2020, 2020.

Smith, G. P. and Crosley, D. R.: A photochemical model of ozone interference effects in laser detection of tropospheric OH, J. Geophys. Res., 95, 16427, https://doi.org/10.1029/JD095iD10p16427, 1990.

Sommariva, R., Lewis, A. C., Pilling, M. J., and Zador, J.: OH and HO_2 chemistry in clean marine air during SOAPEX-2, Atmos. Chem. Phys., 18, 2004.

Song, H., Zou, Q., and Lu, K.: Parameterization and Application of Hydroperoxyl Radicals (HO_2) Heterogeneous Uptake coefficient, 2020.

Stevenson, D. S., Zhao, A., Naik, V., O'Connor, F. M., Tilmes, S., Zeng, G., Murray, L. T., Collins, W. J., Griffiths, P. T., Shim, S., Horowitz, L. W., Sentman, L. T., and Emmons, L.: Trends in global tropospheric hydroxyl radical and methane lifetime since 1850 from AerChemMIP, Atmos. Chem. Phys., 20, 12905–12920, https://doi.org/10.5194/acp-20-12905-2020, 2020.

Stimpfle, R. M. and Anderson, J. G.: In-situ detection of OH in the lower stratosphere with a balloon borne high repetition rate laser system, Geophys. Res. Lett., 15, 1503–1506, https://doi.org/10.1029/GL015i013p01503, 1988.

Stone, D., Evans, M. J., Edwards, P. M., Commane, R., Ingham, T., Rickard, A. R., Brookes, D. M., Hopkins, J., Leigh, R. J., Lewis, A. C., Monks, P. S., Oram, D., Reeves, C. E., Stewart, D., and Heard, D. E.: Isoprene oxidation mechanisms: measurements and modelling of OH and HO_2 over a South-East Asian tropical rainforest during the OP3 field campaign, Atmospheric Chemistry and Physics, 11, 6749–6771, https://doi.org/10.5194/acp-11-6749-2011, 2011.

Stone, D., Whalley, L. K., and Heard, D. E.: Tropospheric OH and HO_2 radicals: field measurements and model comparisons, Chem. Soc. Rev., 41, 6348, https://doi.org/10.1039/c2cs35140d, 2012.

Tan, D., Faloona, I., Brune, W. H., Weinheimer, A., Campos, T., Ridley, B., Vay, S., Collins, J., and Sachse, G.: *in situ* measurements of HO_x in aircraft exhaust plumes and contrails during SUCCESS, Geophys. Res. Lett., 25, 1721–1724, https://doi.org/10.1029/98GL00117, 1998.

Tan, D., Faloona, I., Simpas, J. B., Brune, W., Shepson, P. B., Couch, T. L., Sumner, A. L., Carroll, M. A., Thornberry, T., Apel, E., Riemer, D., and Stockwell, W.: HO_x budgets in a deciduous forest: Results from the PROPHET summer 1998 campaign, J. Geophys. Res., 106, 24407–24427, https://doi.org/10.1029/2001JD900016, 2001a.

Tan, D., Faloona, I., Simpas, J. B., Brune, W., Olson, J., Crawford, J., Avery, M., Sachse, G., Vay, S., Sandholm, S., Guan, H.-W., Vaughn, T., Mastromarino, J., Heikes, B., Snow, J., Podolske, J., and Singh, H.: OH and HO_2 in the tropical Pacific: Results from PEM-Tropics B, J. Geophys. Res., 106, 32667–32681, https://doi.org/10.1029/2001JD900002, 2001b.

Tan, H., Zhang, L., Lu, X., Zhao, Y., Yao, B., Parker, R. J., and Boesch, H.: An integrated analysis of contemporary methane emissions and concentration trends over China using in situ and satellite observations and model simulations, Atmospheric Chemistry and Physics, 22, 1229–1249, https://doi.org/10.5194/acp-22-1229-2022, 2022.

Tan, Z., Fuchs, H., Lu, K., Hofzumahaus, A., Bohn, B., Broch, S., Dong, H., Gomm, S., Häseler, R., He, L., Holland, F., Li, X., Liu, Y., Lu, S., Rohrer, F., Shao, M., Wang, B., Wang, M., Wu, Y., Zeng, L., Zhang, Y., Wahner, A., and Zhang, Y.: Radical chemistry at a rural site (Wangdu) in the North China Plain: observation and model calculations of OH, HO_2 and RO_2 radicals, Atmospheric Chemistry and Physics, 17, 663–690, https://doi.org/10.5194/acp-17-663-2017, 2017.

Tan, Z., Rohrer, F., Lu, K., Ma, X., Bohn, B., Broch, S., Dong, H., Fuchs, H., Gkatzelis, G. I., Hofzumahaus, A., Holland, F., Li, X., Liu, Y., Liu, Y., Novelli, A., Shao, M., Wang, H., Wu, Y., Zeng, L., Hu, M., Kiendler-Scharr, A., Wahner, A., and Zhang, Y.: Wintertime photochemistry in Beijing: observations of RO_x radical concentrations in the North China Plain during the BEST-ONE campaign, Atmospheric Chemistry and Physics, 18, 12391–12411, https://doi.org/10.5194/acp-18-12391-2018, 2018.

Tan, Z., Lu, K., Hofzumahaus, A., Fuchs, H., Bohn, B., Holland, F., Liu, Y., Rohrer, F., Shao, M., Sun, K., Wu, Y., Zeng, L., Zhang, Y., Zou, Q., Kiendler-Scharr, A., Wahner, A., and Zhang, Y.: Experimental budgets of OH, HO_2, and RO_2 radicals and implications for ozone formation in the Pearl River Delta in China 2014, Atmospheric Chemistry and Physics, 19, 7129–7150, https://doi.org/10.5194/acp-19-7129-2019, 2019.

Tan, Z., Hantschke, L., Kaminski, M., Acir, I.-H., Bohn, B., Cho, C., Dorn, H.-P., Li, X., Novelli, A., Nehr, S., Rohrer, F., Tillmann, R., Wegener, R., Hofzumahaus, A., Kiendler-Scharr, A., Wahner, A., and Fuchs, H.: Atmospheric photo-oxidation of myrcene: OH reaction rate constant, gas-phase oxidation products and radical budgets, Atmospheric Chemistry and Physics, 21, 16067–16091, https://doi.org/10.5194/acp-21-16067-2021, 2021.

Tang, J. H., Chan, L. Y., Chan, C. Y., Li, Y. S., Chang, C. C., Wang, X. M., Zou, S. C., Barletta, B., Blake, D. R., and Wu, D.: Implications of changing urban and rural emissions on non-methane hydrocarbons in the Pearl River Delta region of China, Atmospheric Environment, 42, 3780–3794, https://doi.org/10.1016/j.atmosenv.2007.12.069, 2008.

Tanner, D. J. and Eisele, F. L.: Present OH measurement limits and associated uncertainties, J. Geophys. Res., 100, 2883, https://doi.org/10.1029/94JD02609, 1995.

Tanner, D. J., Jefferson, A., and Eisele, F. L.: Selected ion chemical ionization mass spectrometric measurement of OH, J. Geophys. Res., 102, 6415–6425, https://doi.org/10.1029/96JD03919, 1997.

Thames, A. B., Brune, W. H., Miller, D. O., Allen, H. M., Apel, E. C., Blake, D. R., Bui, T. P., Commane, R., Crounse, J. D., Daube, B. C., Diskin, G. S., DiGangi, J. P., Elkins, J. W., Hall, S. R., Hanisco, T. F., Hannun, R. A., Hintsa, E., Hornbrook, R. S., Kim, M. J., McKain, K., Moore, F. L., Nicely, J. M., Peischl, J., Ryerson, T. B., St. Clair, J. M., Sweeney, C., Teng, A., Thompson, C. R., Ullmann, K., Wennberg, P. O., and Wolfe, G. M.: Missing OH reactivity in the global marine boundary layer, Atmospheric Chemistry and Physics, 20, 4013–4029, https://doi.org/10.5194/acp-20-4013-2020, 2020.

Travis, K. R., Heald, C. L., Allen, H. M., Apel, E. C., Arnold, S. R., Blake, D. R., Brune, W. H., Chen, X., Commane, R., Crounse, J. D., Daube, B. C., Diskin, G. S., Elkins, J. W., Evans, M. J., Hall, S. R., Hintsa, E. J., Hornbrook, R. S., Kasibhatla, P. S., Kim, M. J., Luo, G., McKain, K., Millet, D. B., Moore, F. L., Peischl, J., Ryerson, T. B., Sherwen, T., Thames, A. B., Ullmann, K., Wang, X., Wennberg, P. O., Wolfe, G. M., and Yu, F.: Constraining remote oxidation capacity with ATom observations, Atmos. Chem. Phys., 20, 7753–7781, https://doi.org/10.5194/acp-20-7753-2020, 2020.

Volz-Thomas, A., Pätz, H.-W., Houben, N., Konrad, S., and Mihelcic, D.: Inorganic trace gases and peroxy radicals during BERLIOZ at Pabstthum: An investigation of the photostationary state of NO_x and O_3, J. Geophys. Res., 108, 8248, https://doi.org/10.1029/2001JD001255, 2003a.

Volz-Thomas, A., Geiss, H., and Andreas, H.: Introduction to Special Section: Photochemistry Experiment in BERLIOZ, J. Geophys. Res., 108, 8252, https://doi.org/10.1029/2001JD002029, 2003b.

Walker, H. L., Heal, M. R., Braban, C. F., Whalley, L. K., and Twigg, M. M.: Evaluation of local measurement-driven adjustments of modelled cloud-free atmospheric photolysis rate coefficients, Environ. Sci.: Atmos., 2, 1411–1427, https://doi.org/10.1039/D2EA00072E, 2022.

Wang, F., Hu, R., Chen, H., Xie, P., Wang, Y., Li, Z., Jin, H., Liu, J., and Liu, W.: Development of a field system for measurement of tropospheric OH radical using laser-induced fluorescence technique, Opt. Express, 27, A419, https://doi.org/10.1364/OE.27.00A419, 2019a.

Wang, G., Iradukunda, Y., Shi, G., Sanga, P., Niu, X., and Wu, Z.: Hydroxyl, hydroperoxyl free radicals determination methods in atmosphere and troposphere, Journal of Environmental Sciences, 99, 324–335, https://doi.org/10.1016/j.jes.2020.06.038, 2021a.

Wang, T., Xue, L., Brimblecombe, P., Lam, Y. F., Li, L., and Zhang, L.: Ozone pollution in China: A review of concentrations, meteorological influences, chemical precursors, and effects, Science of The Total Environment, 575, 1582–1596, https://doi.org/10.1016/j.scitotenv.2016.10.081, 2017.

Wang, T., Dai, J., Lam, K. S., Nan Poon, C., and Brasseur, G. P.: Twenty-Five Years of Lower Tropospheric Ozone Observations in Tropical East Asia: The Influence of Emissions and Weather Patterns, Geophysical Research Letters, 46, 11463–11470, https://doi.org/10.1029/2019GL084459, 2019b.

Wang, Y., Hu, R., Xie, P., Chen, H., Wang, F., Liu, X., Liu, J., and Liu, W.: Measurement of tropospheric HO_2 radical using fluorescence assay by gas expansion with low interferences, Journal of Environmental Sciences, 99, 40–50, https://doi.org/10.1016/j.jes.2020.06.010, 2021b.

Wang, Y. Q.: MeteoInfo: GIS software for meteorological data visualization and analysis: Meteorological GIS software, Met. Apps, 21, 360–368, https://doi.org/10.1002/met.1345, 2014.

Wang, Y. Q.: An Open Source Software Suite for Multi-Dimensional Meteorological Data Computation and Visualisation, JORS, 7, 21, https://doi.org/10.5334/jors.267, 2019.

Weinstock, B. and Niki, H.: Carbon Monoxide Balance in Nature, Science, 176, 290–292, https://doi.org/10.1126/science.176.4032.290, 1972.

Wennberg, P. O., Stimpfle, R. M., Weinstock, E. M., Dessler, A. E., Lloyd, S. A., Lapson, L. B., Schwab, J. J., and Anderson, J. G.: Simultaneous, in situ measurements of OH, HO_2, O_3, and H_2O: A test of modeled stratospheric HO_x chemistry, Geophys. Res. Lett., 17, 1909–1912, https://doi.org/10.1029/GL017i011p01909, 1990.

Wennberg, P. O., Bates, K. H., Crounse, J. D., Dodson, L. G., McVay, R. C., Mertens, L. A., Nguyen, T. B., Praske, E., Schwantes, R. H., Smarte, M. D., St Clair, J. M., Teng, A. P., Zhang, X., and Seinfeld, J. H.: Gas-Phase Reactions of Isoprene and Its Major Oxidation Products, Chem. Rev., 118, 3337–3390, https://doi.org/10.1021/acs.chemrev.7b00439, 2018.

Whalley, L. K., Edwards, P. M., Furneaux, K. L., Goddard, A., Ingham, T., Evans, M. J., Stone, D., Hopkins, J. R., Jones, C. E., Karunaharan, A., Lee, J. D., Lewis, A. C., Monks, P. S., Moller, S. J., and Heard, D. E.: Quantifying the magnitude of a missing hydroxyl radical source in a tropical rainforest, Atmos. Chem. Phys., 11, 7223–7233, https://doi.org/10.5194/acp-11-7223-2011, 2011.

Whalley, L. K., Stone, D., Dunmore, R., Hamilton, J., Hopkins, J. R., Lee, J. D., Lewis, A. C., Williams, P., Kleffmann, J., Laufs, S., Woodward-Massey, R., and Heard,

D. E.: Understanding in situ ozone production in the summertime through radical observations and modelling studies during the Clean air for London project (ClearfLo), Atmos. Chem. Phys., 18, 2547–2571, https://doi.org/10.5194/acp-18-2547-2018, 2018.

Whalley, L. K., Slater, E. J., Woodward-Massey, R., Ye, C., Lee, J. D., Squires, F., Hopkins, J. R., Dunmore, R. E., Shaw, M., Hamilton, J. F., Lewis, A. C., Mehra, A., Worrall, S. D., Bacak, A., Bannan, T. J., Coe, H., Percival, C. J., Ouyang, B., Jones, R. L., Crilley, L. R., Kramer, L. J., Bloss, W. J., Vu, T., Kotthaus, S., Grimmond, S., Sun, Y., Xu, W., Yue, S., Ren, L., Acton, W. J. F., Hewitt, C. N., Wang, X., Fu, P., and Heard, D. E.: Evaluating the sensitivity of radical chemistry and ozone formation to ambient VOCs and NO_x in Beijing, Atmospheric Chemistry and Physics, 21, 2125–2147, https://doi.org/10.5194/acp-21-2125-2021, 2021.

Wolfe, G. M., Cantrell, C., Kim, S., Mauldin III, R. L., Karl, T., Harley, P., Turnipseed, A., Zheng, W., Flocke, F., Apel, E. C., Hornbrook, R. S., Hall, S. R., Ullmann, K., Henry, S. B., DiGangi, J. P., Boyle, E. S., Kaser, L., Schnitzhofer, R., Hansel, A., Graus, M., Nakashima, Y., Kajii, Y., Guenther, A., and Keutsch, F. N.: Missing peroxy radical sources within a summertime ponderosa pine forest, Atmos. Chem. Phys., 14, 4715–4732, https://doi.org/10.5194/acp-14-4715-2014, 2014.

Wolfe, G. M., Marvin, M. R., Roberts, S. J., Travis, K. R., and Liao, J.: The Framework for 0-D Atmospheric Modeling (F0AM) v3.1, Geosci. Model Dev., 9, 3309–3319, https://doi.org/10.5194/gmd-9-3309-2016, 2016.

Woodward-Massey, R., Slater, E. J., Alen, J., Ingham, T., Cryer, D. R., Stimpson, L. M., Ye, C., Seakins, P. W., Whalley, L. K., and Heard, D. E.: Implementation of a chemical background method for atmospheric OH measurements by laser-induced fluorescence: characterisation and observations from the UK and China, Atmospheric Measurement Techniques, 13, 3119–3146, https://doi.org/10.5194/amt-13-3119-2020, 2020.

Xia, M., Wang, T., Wang, Z., Chen, Y., Peng, X., Huo, Y., Wang, W., Yuan, Q., Jiang, Y., Guo, H., Lau, C., Leung, K., Yu, A., and Lee, S.: Pollution-Derived Br_2 Boosts Oxidation Power of the Coastal Atmosphere, Environ. Sci. Technol., 56, 12055–12065, https://doi.org/10.1021/acs.est.2c02434, 2022.

Xiao, Y., Jacob, D. J., and Turquety, S.: Atmospheric acetylene and its relationship with CO as an indicator of air mass age, J. Geophys. Res., 112, D12305, https://doi.org/10.1029/2006JD008268, 2007.

Yang, X., Lu, K., Ma, X., Gao, Y., Tan, Z., Wang, H., Chen, X., Li, X., Huang, X., He, L., Tang, M., Zhu, B., Chen, S., Dong, H., Zeng, L., and Zhang, Y.: Radical chemistry in the Pearl River Delta: observations and modeling of OH and HO_2 radicals in Shenzhen 2018, Atmospheric Chemistry and Physics Discussions, 1–19, https://doi.org/10.5194/acp-2022-113, 2022.

Yang, Y., Shao, M., Wang, X., Nölscher, A. C., Kessel, S., Guenther, A., and Williams, J.: Towards a quantitative understanding of total OH reactivity: A review, Atmospheric Environment, 134, 147–161, https://doi.org/10.1016/j.atmosenv.2016.03.010, 2016.

Yao, T., Fung, J. C. H., Ma, H., Lau, A. K. H., Chan, P. W., Yu, J. Z., and Xue, J.: Enhancement in secondary particulate matter production due to mountain trapping, Atmospheric Research, 147–148, 227–236, https://doi.org/10.1016/j.atmosres.2014.05.007, 2014.

Zhang, G., Hu, R., Xie, P., Lu, K., Lou, S., Liu, X., Li, X., Wang, F., Wang, Y., Yang, X., Cai, H., Wang, Y., and Liu, W.: Intercomparison of OH radical measurement in a complex atmosphere in Chengdu, China, Science of The Total Environment, 838, 155924, https://doi.org/10.1016/j.scitotenv.2022.155924, 2022a.

Zhang, G., Hu, R., Xie, P., Lou, S., Wang, F., Wang, Y., Qin, M., Li, X., Liu, X., Wang, Y., and Liu, W.: Observation and simulation of HO_x radicals in an urban area in Shanghai, China, Science of The Total Environment, 810, 152275, https://doi.org/10.1016/j.scitotenv.2021.152275, 2022b.

Zhang, M., Akimoto, H., and Uno, I.: A Three-Dimensional Simulation of HO_x Concentrations Over East Asia During TRACE-P, J Atmos Chem, 54, 233–254, https://doi.org/10.1007/s10874-006-9015-0, 2006.

Zhao, D., Pullinen, I., Fuchs, H., Schrade, S., Wu, R., Acir, I.-H., Tillmann, R., Rohrer, F., Wildt, J., Guo, Y., Kiendler-Scharr, A., Wahner, A., Kang, S., Vereecken, L., and Mentel, T. F.: Highly oxygenated organic molecule (HOM) formation in the isoprene oxidation by NO_3 radical, Atmospheric Chemistry and Physics, 21, 9681–9704, https://doi.org/10.5194/acp-21-9681-2021, 2021.

Zhao, Y., Saunois, M., Bousquet, P., Lin, X., Berchet, A., Hegglin, M. I., Canadell, J. G., Jackson, R. B., Dlugokencky, E. J., Langenfelds, R. L., Ramonet, M., Worthy, D., and Zheng, B.: Influences of hydroxyl radicals (OH) on top-down estimates of the global and regional methane budgets, Atmos. Chem. Phys., 20, 9525–9546, https://doi.org/10.5194/acp-20-9525-2020, 2020a.

Zhao, Y., Saunois, M., Bousquet, P., Lin, X., Berchet, A., Hegglin, M. I., Canadell, J. G., Jackson, R. B., Deushi, M., Jöckel, P., Kinnison, D., Kirner, O., Strode, S., Tilmes, S., Dlugokencky, E. J., and Zheng, B.: On the role of trend and variability in the hydroxyl radical (OH) in the global methane budget, Atmos. Chem. Phys., 20, 13011–13022, https://doi.org/10.5194/acp-20-13011-2020, 2020b.

Ziemann, P. J. and Atkinson, R.: Kinetics, products, and mechanisms of secondary organic aerosol formation, Chem. Soc. Rev., 41, 6582, https://doi.org/10.1039/c2cs35122f, 2012.